

**Dissertation**  
**submitted to the**  
**Combined Faculties for the Natural Sciences and for Mathematics**  
**of the Ruperto-Carola University of Heidelberg, Germany**  
**for the degree of**  
**Doctor of Natural Sciences**

**Put forward by**  
**Dipl.-Phys. Kim Melanie Kraus**  
**Born in: Siegen**  
**Oral examination: 15.01.2014**



# **Dose Delivery Study for a Novel Compact Proton Accelerator**

**Referees:**

**Prof. Dr. Uwe Oelfke**

**Prof. Dr. Wolfgang Schlegel**



## **Dosisapplikationsstudie für einen neuen kompakten Protonenbeschleuniger**

Seit mehr als 60 Jahren spielt Protonentherapie eine wichtige Rolle in der Behandlung von Krebs mit ionisierender Strahlung. 3D spot-scanning wurde entwickelt, um eine höchst konformale Dosis im Tumor zu applizieren. Trotzdem ist die Verfügbarkeit von Protonentherapie für die Patienten noch immer limitiert, teilweise aufgrund der hohen Kosten und der Dimensionen von großen Multi-Raum Protonentherapiezentren. Deshalb wurde eine neue kompakte 1-Raum-Anlage für Protonentherapie, namentlich TULIP (TUrning LInac for Proton therapy) entwickelt, basierend auf einem Linearbeschleuniger montiert auf einer Gantry. Dieser Beschleuniger ermöglicht aktive Energievariation auf einer Zeitskala von Millisekunden. Das Ziel dieser Arbeit ist, die Möglichkeiten der Dosisapplikation mit TULIP zu erarbeiten, um die vorteilhaften Eigenschaften bezüglich der Dosisapplikation bestmöglich auszunutzen. Wir haben ein Softwareprogramm entwickelt, welches die Dosisapplikation in einem Tumor simuliert. Mit Hilfe dieses Programms haben wir verschiedene Dosisapplikationsmethoden untersucht und herausgefunden, dass 3D spot scanning in Bezug auf Dosis und Zeit der Rotationstherapie mit Protonen überlegen ist. In einem zweiten Teil haben wir die Untersuchungen auf Dosisabgabe an bewegte Tumore erweitert. Aufgrund schneller Energievariation ist TULIP besonders geeignet für Rescanning, was durch Bestrahlungszeiten von wenigen Minuten belegt werden konnte.

## **Dose Delivery Study for a Novel Compact Proton Accelerator**

Proton therapy has played an important role in the treatment of cancer with radiation therapy for more than 60 years. Active spot scanning to deliver highly conformal dose to the tumor has been developed. However, the availability of proton therapy to the patients is still limited, partly, due to the high costs and sizes of large proton therapy centers. Therefore, a novel compact proton single room facility based on a linear accelerator mounted on a gantry has been proposed, named TULIP (TUrning LInac for Proton therapy). This accelerator allows for active energy variation on a milliseconds time scale. This work aims to assess the possibilities of dose delivery with TULIP to exploit its beneficial features with respect to dose delivery. We developed a software tool, simulating the dose delivery to the tumor. By means of this software tool, we assessed different delivery methods and found 3D spot scanning to be superior to rotational dose delivery with regard to dose and irradiation time. In a second part, we expanded the investigations to dose delivery to moving targets. Due to fast energy variation, we found TULIP to be preferably suitable for rescanning, confirmed by irradiation times of only a few minutes.

# Contents

<b>1</b>	<b>Introduction</b>	<b>1</b>
1.1	Objectives of this work . . . . .	1
<b>2</b>	<b>Proton Therapy</b>	<b>5</b>
2.1	Basic physical properties of protons . . . . .	5
2.2	Proton acceleration . . . . .	8
2.2.1	Cyclotrons . . . . .	9
2.2.2	Synchrotrons . . . . .	11
2.2.3	Fixed Field Alternating Gradient accelerators (FFAGs) . . . . .	13
2.3	Novel accelerator techniques . . . . .	13
2.3.1	Laser induced acceleration of protons . . . . .	13
2.3.2	Dielectric wall accelerator . . . . .	15
2.3.3	Linear particle accelerator . . . . .	15
2.4	Dose delivery and treatment planning with proton beams . . . . .	17
2.4.1	Introduction . . . . .	17
2.4.2	Dose delivery methods for proton beams . . . . .	18
2.4.3	Treatment planning . . . . .	20
2.4.4	Treatment planning for proton beams . . . . .	21
2.5	Treatment of moving organs with protons . . . . .	23
2.5.1	Organ motion in radiation therapy . . . . .	24
2.5.2	Consequences of organ motion for proton beam therapy . . . . .	24
2.5.2.1	Density changes . . . . .	25
2.5.2.2	Interplay effects . . . . .	25
2.5.3	Motion management . . . . .	27
2.5.3.1	Motion monitoring . . . . .	27
2.5.3.2	Motion mitigation and dose delivery strategies . . . . .	29
<b>3</b>	<b>TULIP - TUrning Linac for Proton therapy</b>	<b>35</b>
3.1	Introduction . . . . .	35
3.1.1	Motivation . . . . .	35
3.1.2	TULIP - Design . . . . .	36

3.1.3	TULIP - accelerator and beam line . . . . .	38
<b>4</b>	<b>Static proton dose delivery with TULIP</b>	<b>41</b>
4.1	Dose Delivery Simulation Software . . . . .	41
4.1.0.1	Input Data . . . . .	42
4.1.1	TULip DOse CALculation software -TuDoCa . . . . .	45
4.1.2	Evaluation of the dose calculation software . . . . .	45
4.1.2.1	Methods and Materials . . . . .	47
4.1.2.2	Results . . . . .	50
4.1.2.3	Discussion . . . . .	51
4.1.3	Influence of relative isocenter position on the dose distribution . . . . .	51
4.1.3.1	Materials and Methods . . . . .	57
4.1.3.2	Results . . . . .	57
4.1.3.3	Discussion . . . . .	59
4.2	Dose delivery to static targets . . . . .	60
4.2.1	Dynamic rotational dose delivery . . . . .	61
4.2.1.1	Materials and Methods . . . . .	62
4.2.1.2	Results . . . . .	63
4.2.1.3	Discussion . . . . .	70
4.2.2	3D spot scanning dose delivery with TULIP . . . . .	72
4.2.2.1	Materials and Methods . . . . .	72
4.2.2.2	Results . . . . .	73
4.2.2.3	Discussion . . . . .	79
4.2.3	Influence of breakdown rate on the dose distribution . . . . .	79
4.2.3.1	Materials and Methods . . . . .	80
4.2.3.2	Results . . . . .	80
4.2.3.3	Conclusion . . . . .	81
4.3	Discussion and Conclusion . . . . .	83
<b>5</b>	<b>Dose delivery to moving tumors with TULIP</b>	<b>85</b>
5.1	Introduction . . . . .	85
5.2	Materials and Methods . . . . .	86
5.2.1	4D dose delivery simulation algorithm . . . . .	86
5.2.2	Input data . . . . .	89
5.2.3	Magnitude of motion induced effects . . . . .	93
5.2.4	Rescanning . . . . .	94
5.3	Results . . . . .	95
5.3.1	Magnitude of motion induced effects . . . . .	95
5.3.2	Rescanning . . . . .	96
5.4	Discussion . . . . .	102

<b>6 Summary and outlook</b>	<b>107</b>
<b>Bibliography</b>	<b>113</b>
<b>List of Figures</b>	<b>I</b>
<b>List of Tables</b>	<b>III</b>





# Chapter 1

## Introduction

### 1.1 Objectives of this work

In the treatment of cancer proton therapy has been used for almost 60 years. By the end of march 2013 more than 90000 patients have been treated with protons worldwide since 1955 when the first patient was treated at the Lawrence Berkeley Laboratory in California [PTCOG]. Over the last six years this number has almost doubled. Even though the potential and physical advantages of proton beam therapy have been discovered long ago, the availability of proton therapy is still limited. Based on data from 2010, for each 10 million people 54 photon therapy rooms but only 7 proton therapy treatment rooms are available in developed countries [Amaldi et al., 2010]. A controversial discussion is going on about the rational for proton therapy. The increased costs compared to photon therapy together with the limited availability thereby counteract the potential clinical benefit. The underlying question is:

"If the availability of proton therapy would be increased, would more patients profit from proton therapy?"

We do not intend to answer this question in terms of clinical advantages in comparison to photon therapy. There are many publications dealing with that question and a controversial debate is sparked ([Smith, 2009], [Hoppe et al., 2011], [Alonso-Basanta et al., 2011], [Mohan and Bortfeld, 2011], [DeLaney, 2011], [Hill-Kayser et al., 2011], [Merchant, 2013], [Combs et al., 2013]). However, we intend to answer the question of how the availability of proton therapy could be increased and leave the more general debate on the evidence of the superiority of proton therapy over photon therapy aside.

For some disease sites, patients do not receive and potentially benefit from proton therapy because of the lack of availability, high costs and missing evidence of the superiority compared to photon therapy [Combs et al., 2013]. The increased costs and dimensions of proton therapy devices are regarded as a main obstruction to the spread of this therapy method ([DeLaney, 2011], [Hill-Kayser et al., 2011]).

Also, in the field of dose delivery techniques, efficient 3D spot scanning has been proposed long ago [Lomax, 1999], however, only very few operating facilities worldwide offer this - from a physical point of view - beneficial dose delivery method. Most proton therapy offering sites employ passive beam delivery - meaning that the dose is delivered by a broad proton beam whose energy and shape is modulated by absorbing material within the beam's path [Mohan and Bortfeld, 2011]. For active spot scanning, the field is shaped by multiple pristine proton spots, that can be influenced in their energy, position and weight on an individual basis. Therefore, this technique offers increased flexibility and thus better dose conformation to the target. However, still technical challenges as well as high sensitivity that comes along with the precise dose shaping hamper this sophisticated delivery method on its way into clinical routine.

Researchers worldwide pursue different approaches to overcome these problems. One trend is the development of relatively small and more cost-effective proton therapy accelerators. Part of this development is to reduce the size and costs of common accelerators used for proton therapy, as they are cyclotrons and synchrotrons ([MEVION], [Schippers and Lomax, 2011], [Schillo et al., 2001], [Klein et al., 2005], [IBA], [Picardi et al., 1994], [Protom International]). For synchrotrons, also the improvement of beam acceleration and extraction time scales with respect to dose delivery is studied to make treatment more efficient ([Peggs, S and Barton, D, 2002], [Iwata et al., 2010]).

Beside the improvement of existing technologies, also new acceleration concepts are studied. One interesting approach is based on laser induced charged particle acceleration ([Wilks et al., 2001], [Schippers and Lomax, 2011], [Robinson et al., 2008]). A high power laser induces the formation of a strong electric field capable to accelerate protons. To date, laser acceleration of protons is still subject to research. Many challenges have to be overcome and the costs for the required high-power lasers must be reduced to make this accelerator type usable for therapeutic application.

Another emerging accelerator type is the "Dielectric Wall Accelerator" (DWA) [Sampayan et al., 1998]. An electromagnetic wave travels through a tube surrounded by alternating conducting and insulating wall material. While the electromagnetic wave moves along the tube an electric field is induced, which can accelerate protons. These accelerators offer high gradients and reduction of size. However, still technical challenges with regard to the required energy for therapeutic use has still to be overcome.

All of these new accelerating techniques, that are described in more detail in section 2.2, are fascinating and might be of relevance for clinical proton therapy. However, they are still subject to research and may need a longer time until all obstructions are diminished and the way into clinical practice is cleared.

In this work we try to answer the question how the availability of proton therapy can be increased in a time scale less than ten years. We present a novel compact linear accelerator for protons with a footprint of about two photon linac vaults - named "TULIP" - TUrning LInac for Proton therapy [Amaldi et al., 2008]. It can be installed as a single room proton therapy facility in already existing medical centers. Furthermore, this

unique device offers an improved time scale for radiation treatments with protons with active 3D spot scanning. Due to the beneficial pulse structure and linac design energy and weight modulation are feasible on a pulse-by-pulse basis. With that, this accelerator offers advantageous characteristics for treatment of moving tumors with rescanning and beam tracking. This work, however, is not dedicated to a detailed description of the accelerator design, but rather to the dose delivery achievable with this new device. We have developed a dose delivery and calculation algorithm for TULIP specific dose calculation (TuDoCa). Since software development was one major part of this thesis, one section is dedicated to the evaluation of TuDoCa (4.1). Using this software tool, we have simulated time dependent and static dose delivery with TULIP for static tumors to investigate whether active proton dose delivery with TULIP for common tumor sites is feasible. This is described in section 4.2.

In chapter 5 dose delivery to moving tumors with TULIP is described. To exploit the effects of TULIP beam characteristics for irradiation of moving targets, dose delivery simulation was performed for lung and liver tumors. Rescanning of the moving tumor volume represents one promising motion mitigation technique for active spot scanning dose delivery. However, the time structure achievable with common accelerators is often an obstruction to this method. With TULIP and its fast flexibility of beam modulation we envisage to improve the dose delivery for rescanning in terms of irradiation time. Moreover, for further investigations we can also think of beam tracking of the moving tumor combined with rescanning to average out residual dose disturbances. The effect of TULIP specific characteristics on rescanning dose delivery is also studied in chapter 5.



# Chapter 2

## Proton Therapy

Proton therapy has its origin in the discovery of the Bragg Peak in 1904 [Bragg, 1904]. Wilson then discovered that protons lose the majority of their incidental energy at the end of their range when traveling through matter. Based on these findings protons were first used for patient treatment in 1954 [Tobias et al., 1958]. Until the end of March 2013 93895 patients have been treated with protons since then [PTCOG]. 42 operating treatment sites exist to date all over the world. The physical properties of protons when penetrating matter make proton therapy an appealing way to treat cancer. Emerging state-of-the-art techniques such as spot scanning give rise to further improvement. New concepts of proton acceleration and beam line designs propagate the spreading of proton therapy. In this chapter the fundamentals of proton therapy physics are explained.

### 2.1 Basic physical properties of protons

In contrast to photons, particles such as protons and heavier ions are not absorbed when they travel through matter. They are slowed down and stopped. The unique energy loss at the end of their path in matter is commonly known as the Bragg Peak, visualized in figure 2.1.1. While protons traverse matter they can either interact with atomic electrons or the nuclei. Most relevant for the energy loss of the protons is electromagnetic interaction with electrons while scattering of the protons is mainly due to elastic scattering off the atomic nuclei. Other effects, such as inelastic nuclear reactions or inelastic scattering off the atomic electrons are of minor importance for energies used for proton therapy (70 MeV - 250 MeV).

The predominant energy loss of protons  $\frac{dE}{dx}$  also referred to as *stopping power*

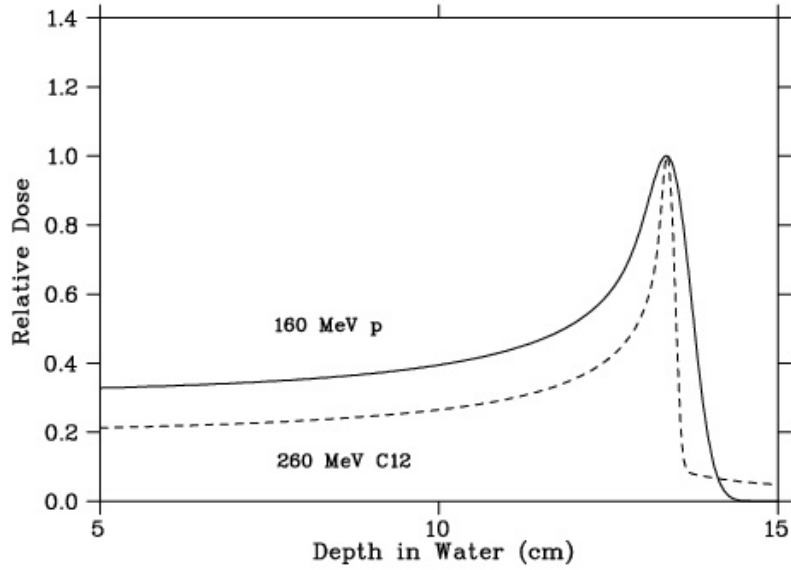


Figure 2.1.1: Schematic drawing of depth dose curves for protons and Carbon ions. The characteristic low entrance dose and a steep dose fall-off at the end of their path for protons and Carbon ions can be seen. (taken from [Multimedia DVD, 2007])

$S(E)$  in a medium can be described by the Bethe-Bloch-formula

$$S(E) = -\frac{dE}{dx} = 4\pi r_e^2 c^2 N_A \frac{Z}{A} \frac{z^2}{\beta^2} \rho_e \left[ \ln \left( \frac{2m_e c^2 \beta^2}{I_{exc}(1 - \beta^2)} \right) - \beta^2 - \frac{C}{Z} - \frac{\delta}{2} \right] \quad (2.1.1)$$

with  $r_e$  the classical radius of the electron,  $m_e$  the mass of an electron,  $c$  the velocity of light,  $N_A$  the Avogadro constant,  $Z$  the charge of the target atom,  $A$  the mass of the target atom,  $z$  the projectile charge,  $\beta$  the particle velocity,  $I$  the mean excitation energy. The last two terms are correction terms.  $\frac{C}{Z}$  is the shell correction taking into account that the atomic electrons are not stationary and gets relevant at particle energies smaller than the orbital electron velocity. The density correction  $\frac{\delta}{2}$  refers to the dielectric polarization of media which changes the electric field interacting with the projectile. This effect becomes important for kinetic energies higher than  $m_e c^2$  which is out of range for therapeutic applications. Given the stopping power of the transversing particles their range in matter  $R(E)$  is also a function of the initial energy  $E$ . The average path length can be derived by the *Continuous Slowing Down Approximation* (CSDA). There the range of a particle is defined as the path length where the mean particle energy is zero.

$$R_{CSDA}(E) = \int_0^E dE' \frac{1}{S(E')} \quad (2.1.2)$$

A simplified version is known as the Bragg-Kleeman rule:

$$R_{CSDA}(E) = AE^p \quad (2.1.3)$$

where  $p$  has been determined to  $p \approx 1.7 - 1.8$  and  $A = 0.0022 \text{ cm/MeV}^p$ . However, the scattering of a bunch of particles underlies statistical fluctuations resulting in variance of energies and ranges. The so called *range straggling* increases with increasing particle energy. Thus, the Bragg Peak gets broader with increasing energy of the incoming particles. For a large number of interactions a Gaussian shaped probability distribution of energy loss  $\Delta$  with  $\bar{\Delta}$  the mean energy loss and  $\sigma$  the standard deviation can be assumed [Leo, 1994]

$$f(\Delta) \propto \exp\left(\frac{-(\Delta - \bar{\Delta})^2}{2\sigma^2}\right), \quad (2.1.4)$$

where  $\sigma$  depends on the path length, the density and the fraction  $\frac{Z}{A}$  of the material with atomic number  $Z$  and mass  $A$ .

The lateral distribution of a bunch of particles traveling through matter is mainly influenced by multiple elastic Coulomb scattering. The particles are scattered by the electric field of the target nuclei causing a deflection of the particles off their path. Neglecting spin effects and screening, this deflection can be described by the Rutherford cross section for target nuclei with charge  $Z$ , projectiles with charge  $z$  and initial energy  $E$  and is peaked towards small angles  $\theta$ .

$$\frac{d\sigma}{d\Omega} = \left(\frac{zZe^2}{E}\right)^2 \frac{1}{4\sin^4(\theta/2)} \quad (2.1.5)$$

The effect of many small angle deflections is called multi Coulomb scattering (MCS) and was described by *Moliere's Theory* formalism ([Molière, 1948], [Bethe, 1953]). The deflection, thus the width, scales with the penetration depth in matter. Hence, particles with small initial energies and shorter ranges will result in sharper Bragg peaks than particles with higher initial energies. In practice Moliere's theory can be approached by a Gaussian function for the lateral distribution of the fluence

$$L(z, r, E_0) = \frac{1}{2\pi\sigma^2(z, E_0)} \exp\left[-\frac{1}{2} \frac{r^2}{\sigma^2(z, E_0)}\right], \quad (2.1.6)$$

where  $E_0$  is the initial energy of the particles and  $r$  the lateral distance.  $\sigma(z, E_0)$  is the width, that increases with increasing depth  $z$  and consists of two components

$$\sigma^2(z, E_0) = \sigma_0^2(E_0) + \sigma_{MCS}^2(z, E_0) \quad (2.1.7)$$

where the first term describes the machine dependent lateral width of the beam caused by deflections within the treatment machine's nozzle and the second component refers to the multi Coulomb scattering (MCS) in the traversed matter [Schlegel, 2001].

For treatment of tumors in radiation therapy the most relevant quantity is the absorbed dose inducing cell death. Dose in tissue is defined as the absorbed energy per unit mass measured in Gy.

$$D = \frac{dE}{dm} \left[ \frac{J}{kg} = Gy \right] \quad (2.1.8)$$

According to [Hong et al. \[1996\]](#) the three dimensional distribution of dose  $D(r)$  can be calculated by the product of the depth dose curve along the central ray  $D_{cax}(z, E_0)$  and the lateral dose fall-off  $L(z, r, E_0)$  due to spreading of the beam

$$D(z, r, E_0) = D_{cax}(z, E_0) \cdot L(z, r, E_0) \quad (2.1.9)$$

Besides their physical characteristics protons and heavier ions show also biological properties different from photons. To account for the biological effects of different particles the *Relative Biological Effectiveness* (RBE) is defined as

$$RBE = \frac{D_{ref}}{D_p} \Big|_{isoeffect}, \quad (2.1.10)$$

with the biologically isoeffective doses  $D_{ref}$  and  $D_p$  for a reference photon source such as  $^{60}Co$  and for a particle species  $p$ , respectively. The biologically equivalent dose thus is defined as

$$ED = D_p \cdot RBE. \quad (2.1.11)$$

The RBE depends on the dose, the particle type, the biological system and the *Linear Energy Transfer* (LET), which characterizes the energy transferred per unit path length. Even though it is known nowadays that the RBE is not a constant quantity, in state-of-the-art radiation therapy the RBE for protons is assumed to have a constant value of 1.1. For heavier particles such as carbon ions, the RBE shows a large variation. Therefore, biological models such as the Local Effect Model (LEM) have already been developed at *Gesellschaft für Schwerionenforschung* (GSI) [[Scholz and Kraft, 1996](#)], [[Scholz and Kraft, 1994](#)] and a semi-empirical model at the National Institute of Radiological Sciences (NIRS) ([[Kanai et al., 1999](#)], [[Kanai et al., 2006](#)]).

## 2.2 Proton acceleration

This section summarizes proton accelerator techniques currently applied in hadrontherapy such as cyclotrons (2.2.1) and synchrotrons (2.2.2) as well as recent developments for these techniques. Novel accelerator techniques that are still subject to research and not used in clinical application are introduced in 2.3. An overview on rather new accelerating methods such as laser induced particle acceleration (2.3.1) and dielectric wall accelerators (2.3.2) is given. Although linear acceleration of charged particles is a well known acceleration concept, it is still subject to further developments and applications

in radiation therapy. Along the historical chain of developments of compact linear proton accelerators the reader is introduced to the field of linear particle accelerators (2.3.3).

## 2.2.1 Cyclotrons

A cyclotron as illustrated in figure 2.2.1, consists of two dipole magnets and two D-shaped electrodes with a radiofrequency (RF) generator generating an alternating electrical field between the D electrodes and a particle source in the middle. The dipole induced constant magnet field perpendicular to the electric field deflects the particles onto a spiral path. While the particles pass the electric field between the D-electrodes they are accelerated. With increasing energy the radius of their path increases.

For a circular orbit caused by the deflecting magnetic field  $B$  the magnetic force (also called *Lorentz force*) for a particle with mass  $m$  is equal to the centripetal force

$$\frac{mv^2}{r} = Bqv \quad (2.2.1)$$

with  $r$  the radius and particle charge  $q$  and its velocity  $v$ . Thus the time required for one circle ( $2\pi r$ ) is independent of the radius

$$T_{circ} = \frac{2\pi m}{BQ}. \quad (2.2.2)$$

However, when particles approach the speed of light  $c$  the mass increases as a function of their speed  $v$

$$m = \frac{m_0}{\sqrt{1 - (\frac{v}{c})^2}}, \quad (2.2.3)$$

with the rest mass  $m_0$  of the particle.

Since the circular velocity is given by  $v = \omega r$  with  $\omega$  being the angular frequency, the circulation time increases with increasing radius. Additionally, for very strong magnetic fields a decrease of the magnetic field with increasing radius can be observed. This also leads to an increase of the circulation time with the radius. In order to compensate for these effects one can either vary the alteration frequency of the electric field or the magnetic field. Decrease of the frequency of the RF field with increasing radius is realized in a synchro-cyclotron allowing for strong magnetic fields and a reduction of the cyclotron in size. However, a synchro-cyclotron does no longer deliver a continuous particle beam.

The alternative method of increasing  $B$  with increasing radius is called isochronous cyclotron. This can be realized by an azimuthally varying magnetic field keeping the particles on their path. Cyclotrons with a diameter of 3.5 m to 5 m are commonly used for lighter particles such as protons in radiation therapy up to now [Paganetti, 2012]. For heavier particles more sophisticated solutions must be developed to match the requirements with regard to space and weight.

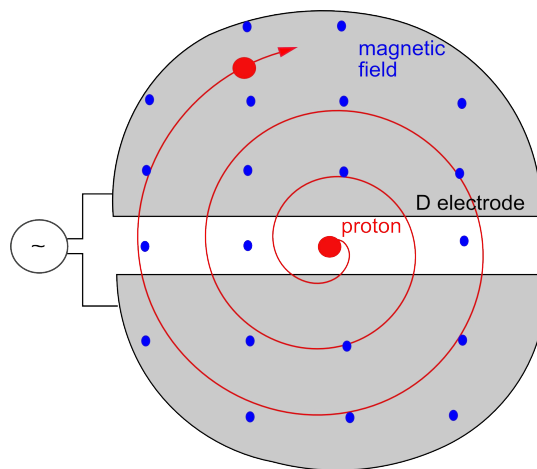


Figure 2.2.1: Schematic drawing of a cyclotron. A proton source is positioned in the middle between two D-shaped electrodes. Due to a magnetic field perpendicular to the electric fields, protons travel on a spiral path and are accelerated each time they pass the gap between the electrodes.

For all types of cyclotrons energy variation, which is crucial in particle therapy, can only be realized by the use of degraders which comes along with an activation of the degrader material and the necessity of shielding. One advantage of cyclotrons is the continuous available beam and the energy variation within 50 - 100 ms by moving absorbers in the beam's path [Amaldi et al., 2010].

Newer developments focus on the reduction of size by using superconducting magnets. A 30 MeV cyclotron mounted on a gantry for neutron therapy has been built first by [Maughan et al., 1994]. Varian (former ACCEL) [Varian Medical Systems] together with Paul Scherrer Institute (PSI) have designed and constructed the first superconducting cyclotron reaching energies up to 250 MeV for proton therapy. It employs a 3.8 T magnet which leads to an overall diameter of 3.5 m and a weight of approximately 100 tons [Schippers and Lomax, 2011], [Schillo et al., 2001], [Klein et al., 2005]. MEVION medical systems (former Still Rivers) [MEVION] has built a superconducting synchrotron of 1.8 m diameter as shown in figure 2.2.2 operating at a 10 T magnetic field [Mevion Medical Systems, 2012]. Energy variation and beam shaping is realized through degraders, modulators and collimators that are potential source of additional dose due to activation processes. IBA has also developed a single room proton therapy solution called "ProteusOne" [IBA]. Here the synchro-cyclotron is positioned on the ground while the beam is bent on a gantry around the patient. Even though up to date all operating sites using carbon ions are synchrotron based, a compact superconducting cyclotron for carbon, helium ions and protons has been proposed [Jongen et al., 2010].

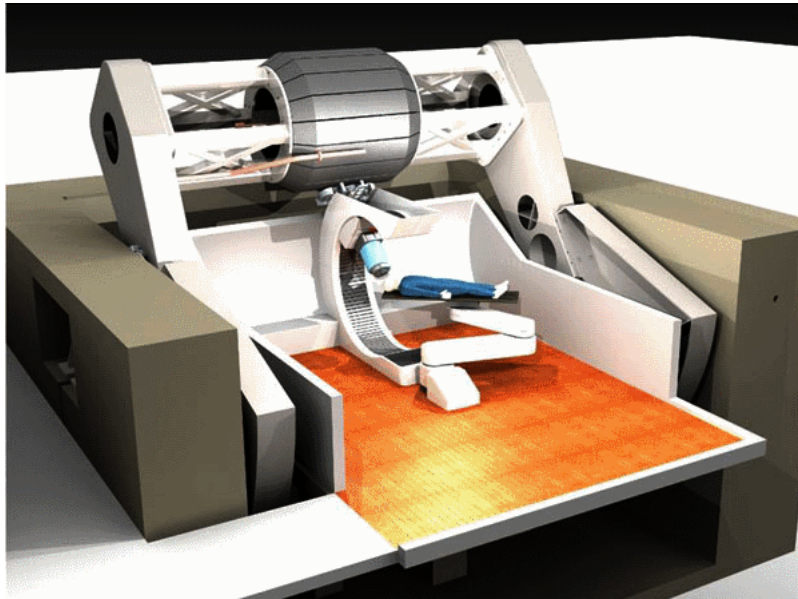


Figure 2.2.2: Design of a single room proton therapy system by *Mevion* [MEVION]: MEVION S250. The superconducting cyclotron is mounted on a gantry.

## 2.2.2 Synchrotrons

In synchrotrons particles are kept on a constant circular radius by increasing the electric and magnetic fields as the particles gain energy. Similar to a cyclotron, in synchrotrons particles are accelerated by passing the accelerating sections multiple times on a circular path as visualized in figure 2.2.3. A bunch of particles that originates from a source is pre-accelerated and then injected into the accelerator ring where the particles are accelerated and deflected on a circular orbit. Dipole magnets keep the particles on their path while quadrupole magnets are required for focusing of the beam. The Coulomb force of an alternating electric field accelerates the particles in multiple accelerating sections in about one million of cycles. With synchrotrons, higher energies are achievable than with cyclotrons. The energy of the particles can be varied without the use of degraders just by extracting the particles after the required number of turns. This avoids the harmful effect of activation of a degrader that can occur in cyclotrons. Once the bunch of particles with the required energy is extracted, the synchrotron has to be refilled to accelerate another bunch of particles. The time consuming energy variation (several seconds) is one major drawback for application of synchrotrons in radiation therapy especially for moving tumors. The overall irradiation time is increased which is crucial for radiation therapy for moving organs with motion management techniques such as rescanning and gating (2.5.3.2). These techniques elongate the treatment time on principle. Unfavorable beam time structures as for non-continuous beams produced

by synchrotrons with long energy variation time compromise the treatment time even more.

While synchrotrons for protons are about 6 m in diameter, for carbon ions they are even larger (25 m). The size and costs of conventional synchrotrons are major limitations to the widespread use of synchrotrons for large proton therapy centers compared to photon therapy. For carbon ions, synchrotrons are the only accelerator type in use for medical purposes up to day while for protons other accelerating techniques, such as the cyclotron and the techniques described in the following sections, are employed, too.

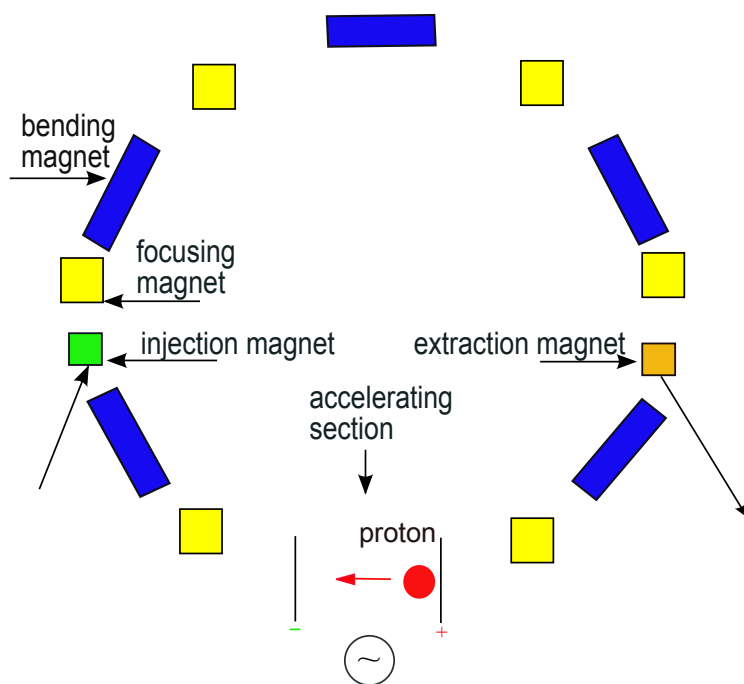


Figure 2.2.3: Schematic drawing of a synchrotron. Charged particles are injected into a ring structure with several accelerating units and magnets for bending and focusing of the beam. While the particles travel on an circular orbit, the accelerating units are passed multiple times before the particles are extracted.

More recent developments focus on the design of smaller synchrotrons or improved time scales of the beam acceleration and extraction. A rapid cycling synchrotron with an increased repetition rate of 30 Hz has been proposed in 2002 [Peggs, S and Barton, D, 2002]. There, all protons accelerated to the required energy are extracted at once. Alternative and more efficient energy selection patterns are investigated [Iwata et al.,

2010], where the beam is accelerated to its maximum energy and then stepwise decelerated. Extended flattops provide the possibility to extract particles at various energies at a single synchrotron cycle. Also, smaller synchrotrons for protons of a diameter of 2.1 m and energies up to 200 MeV have been studied by TERA [Picardi et al., 1994]. *ProTom* together with MIT-Bates Linear Accelerator Center has proposed a compact synchrotron accelerating protons up to 330 MeV for 3D beam scanning [Protom International]. According to *Protom*, this device should fit into two conventional linac rooms.

### 2.2.3 Fixed Field Alternating Gradient accelerators (FFAGs)

For several years the use of FFAGs in particle therapy has been studied. FFAGs combine a fixed magnetic field with varying frequency of a synchro-cyclotron with alternating gradients along the beam line as used in synchrotrons. Thus, the accelerator provides a continuous beam with strong focusing. The bending magnet is split up into sector magnets that are arranged in triplets with opposed alternating bending directions. Two different basic designs are studied: in scaling FFAGs the magnetic field of the bending magnets increases with the radius of the orbits of the accelerated particles. Thus, with increasing particle energy the orbit moves outwards while keeping the same shape. In non-scaling FFAGs orbits do not keep the same shape with increasing radius. That makes the extraction at different energies even more complex because all beams have to be guided through the same transport system with limited momentum acceptance [Amaldi et al., 2010], [Fourrier et al., 2008]. The non-scaling FFAGs are smaller in size, however, the magnet design and the alternating high magnetic fields make the construction and operation challenging [Paganetti, 2012]. Of interest in application in radiation therapy is the possibility for fast energy and intensity variation due to higher repetition rates as used in synchrotrons. However, scaling FFAGs with a radius of 7-8 m are not small nor light (weight of 150-200 tons)- moreover, both types need an injector accelerating particles to several MeVs before entering the FFAGs [Paganetti, 2012], which enlarges the accelerating system further.

## 2.3 Novel accelerator techniques

### 2.3.1 Laser induced acceleration of protons

A promising compact and cost-effective alternative to synchrotron and cyclotron based methods is the laser-driven acceleration of charged particles. A compact laser accelerator could, in principle, be installed in normal rooms and possibly, require less shielding than cyclotrons and synchrotrons.

Up to now, the most commonly studied technique is the *Target Normal Sheath Acceleration* (TNSA) [Wilks et al., 2001], [Schippers and Lomax, 2011]. A high-intensity

laser ( $I_{laser} \geq 10^{18} \frac{W}{cm^2}$ ) is focused on a thin solid target with its front side saturated with hydrogen. Within the focal spot of the laser on the target material a plasma is generated. The interaction of the laser with the plasma results in heating of the electrons traveling to the rear side of the target and build up a strong electric field in the order of  $\frac{TV}{m}$ . The atoms of the target foil are ionized and protons from the front side of the target are then accelerated out of the rear end due to the strong electric field as shown in figure 2.3.1. With this method, protons as well as ions can be accelerated to high energies. However, the accelerated particles are not monoenergetic and cannot be directly used for radiotherapy. Therefore, energy selection systems have to be installed to select the particles with the required energy. In order to avoid the inefficient effect of particle loss the use of broader beams within certain parts of the target volume is investigated [Schell and Wilkens, 2012].

Another method of laser-driven particle acceleration is *Radiation Pressure Acceleration* (RPA) [Robinson et al., 2008]. The laser is focused on a very thin target foil ( $\leq 100$  nm) which is then accelerated as a plasma slab. Advantages of this method are higher resulting energies of the particles and less energy spread [Paganetti, 2012].

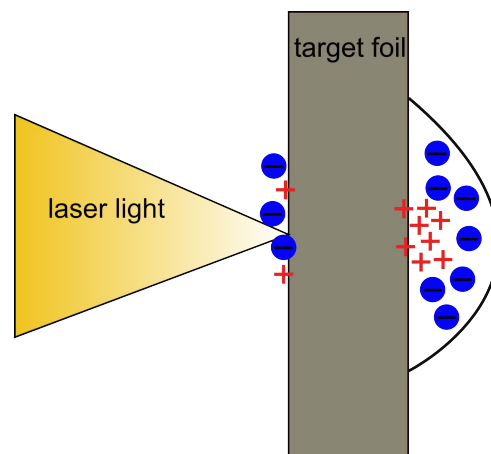


Figure 2.3.1: The laser light induces a plasma within the target foil. Electrons (blue) penetrate to the rear end. The resulting electric field ionizes the atoms within the foil and protons are accelerated out of the foil. Adapted from [Schippers and Lomax, 2011].

Today, high-power lasers as required for radiation therapy use with protons are very bulky and costly. This is one of the reasons for which laser induced proton acceleration for proton therapy, as actively pursued by many research groups, has still to face these and other challenges. Therefore, one cannot expect to have a clinically applicable and competitive solution in less than ten years.

### 2.3.2 Dielectric wall accelerator

In 1998 a new technique of proton acceleration has been patented by a developer group at Lawrence Livermore National Laboratory (LLNL) [[Sampayan et al., 1998](#)]. In *Dielectric Wall Accelerators* (DWAs) an electromagnetic wave travels through a tube surrounded by dielectric material as shown in figure 2.3.2. The electromagnetic wave is generated by an external source switched on and off rapidly inducing very short (ns) current pulses. While the electromagnetic wave travels through the tube, an electric field is generated which accelerates the protons. In order to reduce the size very high gradients are required. In *High Gradient Insulators* (HGIs) layers of alternating insulating and conductive material are stacked and form the inner wall of the accelerator tube. The so called Blumeline transmission lines - which are very rapidly switched by the laser pulses illuminating the photoconductive switches shown in figure 2.3.2 - produce very intense electric fields between two successive metal electrodes of the HGI. By that an electromagnetic wave is propagated through the transmission lines. [[Caporaso, 2011](#)]. The interruption of insulators by conductive material prevents the generation of electron avalanches and breakdowns since the electrons are repelled from the insulators [[Caporaso et al., 2009](#)]. The major advantage of HGIs is that the achievable accelerating electric field can be increased while keeping the size of the accelerator small. Compared to normal induction cavities where the field is limited to 20 MV/m, the accelerating field achieved with HGIs is up to 100 MV/m for a nanoseconds-pulse [[Caporaso et al., 2008](#)]. According to [Alonso \[2011\]](#) an accelerating field of 100 MV/m would result in a proton DWA of about 2 m length.

After cooperation of LLNL with *Tomo Therapy* in 2007, CPAC (*Compact Particle Accelerator Corporation*) [[CPAC, 2013](#)] as a *Tomo Therapy* spin-off took over responsibility for the commercialization of the DWA. There are still many technical challenges to overcome on the way to development of the DWA for clinical application. In 2012 CPAC reported successful operation of the DWA prototype with a 20 MeV/m gradient. For 2013 an upgrade to 35 MeV/m was claimed. CPAC announces the first clinical system, which should fit into two conventional electron linac rooms and is supposed to reach energies from 50 MeV to 150 MeV. In contrast to the very early concepts for clinical use, in this concept no gantry mounting of the DWA is foreseen. However, 3D beam scanning with a fixed beam will be feasible and an upgrade of the maximum energy to 215 MeV is forecasted [[CPAC, 2013](#)].

### 2.3.3 Linear particle accelerator

The principle of radiofrequency linear acceleration of particles is far away of being new. However, the acceleration of charged particles heavier than electrons for radiation therapy treatment is challenging, since the accelerator size increases for heavier particles, where larger electric gradients are required, resulting in much longer accelerators than

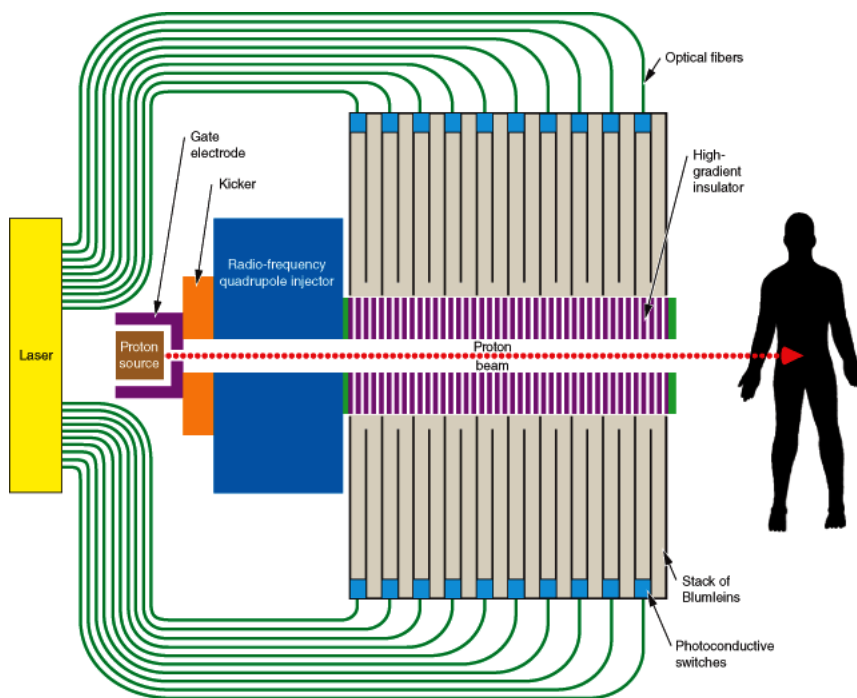


Figure 2.3.2: Schematic drawing of a dielectric wall accelerator (DWA) taken from [S&T Review, 2011], Lawrence Livermore National Laboratory (LLNL). Protons are injected into a tube lined with high gradient insulators (HGIs) and are accelerated by an electric field generated by rapidly alternating voltage. A laser delivers power to the switches in the Blumleins

the ones used in X-ray therapy. With the idea of reducing the size of particle linacs for radiation therapy applications, these accelerators came also into the focus of research again. In principle, linear accelerators (linacs) accelerate particles through a RF controlled alternating electric field between subsequent cylindrical electrodes (cavities). Due to the increasing velocity of the particles the electrodes must be increased in length to ensure particle acceleration within the next gap. A long time ago, linear accelerators for protons were investigated for treatment of eyes [Lennox, 1989], where the required energy is below 70 MeV. In following approaches linear accelerators aimed to accelerate particles to higher energies required for radiation therapy treatment. In 1991, Hamm et al. [Hamm et al., 1991] proposed the first side coupled linac (SCL) operating at 3 GHz which accelerates protons from 70 MeV to 250 MeV. In later approaches proton linacs were also designed to boost particles pre-accelerated by a cyclotron to radiation therapy relevant energies [Amaldi et al., 2009]. In 1993, TERA foundation (*Fondazione per Adroterapia Oncologica*) proposed a *cyclinac* - a novel concept of compact proton accelerators [Amaldi, U. and Grandolfo, M. and Picardi, L., 1996]. A cyclinac as shown in figure 2.3.3 consists of a high frequency linear accelerator working at a high repetition rate and serving as a booster of a cyclotron. The high frequency ensures compactness of the accelerator even if today one knows that the old Kilpatrick scaling law, which stated that the accelerating electric field scales with the square root of the frequency ( $E \propto f^{\frac{1}{2}}$ ) [Kilpatrick, 1957] is not applicable any more. The many experiments performed in connection with the development of future electron-positron colliders have brought to better models, in particular the "power flow model" [Grudiev et al., 2009] and the "defect model" [Nordlund and Djurabekova, 2012]. However, it is certainly true, that with increasing electric fields, the length of the accelerator can be decreased to reach the same output energy. The first design was introduced in 1998 and named LIBO (*LInac BOoster*). A prototype of LIBO which is one module of the full linac consisting of nine modules has been constructed and tested. One module comprises 4 tanks with a number of cavities. Operating at 3 GHz a gradient of 28.5 MV/m per tank was reached [Amaldi et al., 2004]. The first TERA linac was designed to accelerate protons from 60 MeV to 200 MeV and would consist of nine of such modules on a total length of 15 m. The modules of the accelerator are powered by individual klystrons that make the energy variation of the beam flexible and fast.

## 2.4 Dose delivery and treatment planning with proton beams

### 2.4.1 Introduction

The goal of radiation therapy is to destroy malignant tumour cells by radiation induced damage while sparing healthy surrounding tissue. In order to precisely shape the pro-

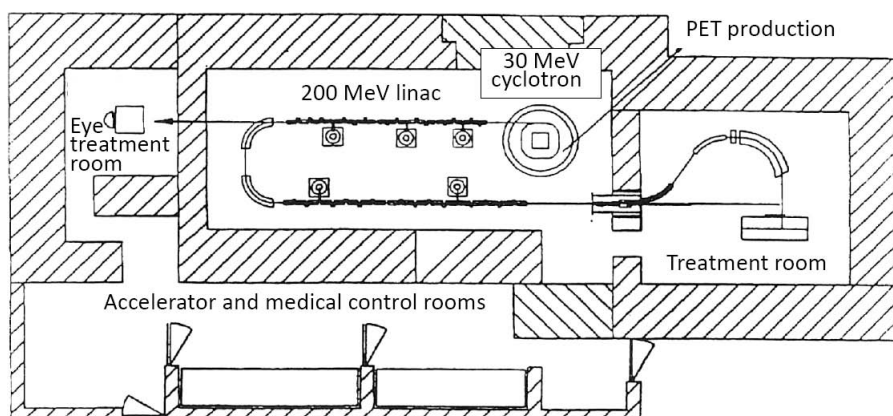


Figure 2.3.3: Schematic drawing of the 1993 cyclinac proposal (taken from [Amaldi et al., 2009]). A commercial 30 MeV cyclotron is used as an injector to a high frequency linac.

ton beam to match the tumour contours, different delivery and treatment planning techniques are used.

Depending on the applied accelerating method basically two different methods for proton beam delivery are available - passive and active proton beam delivery. In passive proton beam delivery the beam is modulated in lateral and longitudinal direction by the use of scattering and range-shifting material positioned in the beam path. Active scanning uses a magnetic deflection system to move the beam laterally across the target volume while the energy is varied actively by the accelerator. Both methods are applied in currently operating proton therapy facilities, however, the majority of them is using passive beam delivery even though the physical advantages of active beam scanning are predominate. In the following both methods are described and compared. In section 2.4.2 different delivery strategies for proton therapy are summarized. Sections 2.4.3 and 2.4.4 introduce the reader into the fundamentals of treatment planning.

## 2.4.2 Dose delivery methods for proton beams

Currently, two different methods are applied in proton therapy - active and passive beam delivery.

In **passive beam delivery** as visualized in figure 2.4.1, the beam is modulated through the use of absorbers, degraders and compensators put into the beam's path [Chu et al., 1993]. Particles are accelerated to their maximum energy and decelerated by the loss of energy in a degrader material. Since the entire target volume has to be covered with dose the beam is spread out by overlaying narrow Bragg peaks of different energies. The beam first passes through scattering foils where multiple Coulomb scattering spreads the beam in the transversal plane. Subsequently, a rotating wheel

of variable thickness along its circumference within the beam's paths decelerates the beam depending on the absorber thickness at the point of interaction. The resulting *Spread Out Bragg Peak* (SOBP) is laterally conformed to the target's shape by patient specific compensators ("boluses") and collimators; in modern radiation therapy also movable collimators (called "multileaf collimators") are used. Obviously, the amount of material provides a potential source of secondary radiation due to interaction processes within the materials. The proton field shaped by the compensators and degrader is uniform [Goitein et al., 2002]. By the use of compensators energy modulation can only be performed on the beam's cross section which is supposed to match the projection of the tumor cross section in the beam direction. Therefore, density changes, i.e. due to tumor movement, that cannot be taken into account by the compensator, can lead to additional dose to healthy tissue. [Schippers and Lomax, 2011]. Also, the energy variation and lateral shaping of the beam through scattering comes along with a significant particle loss [van Goethem et al., 2009]. However, there are reasons why up to now passive beam delivery is the most widely spread delivery technique. Since the entire target is treated with one modulated spread out bragg peak at the same time the method is less sensitive to organ movement. Since passive beam delivery does not depend on a continuous beam, another advantage is that it can be used for all currently used accelerator systems in radiation therapy [Schippers, 2009].

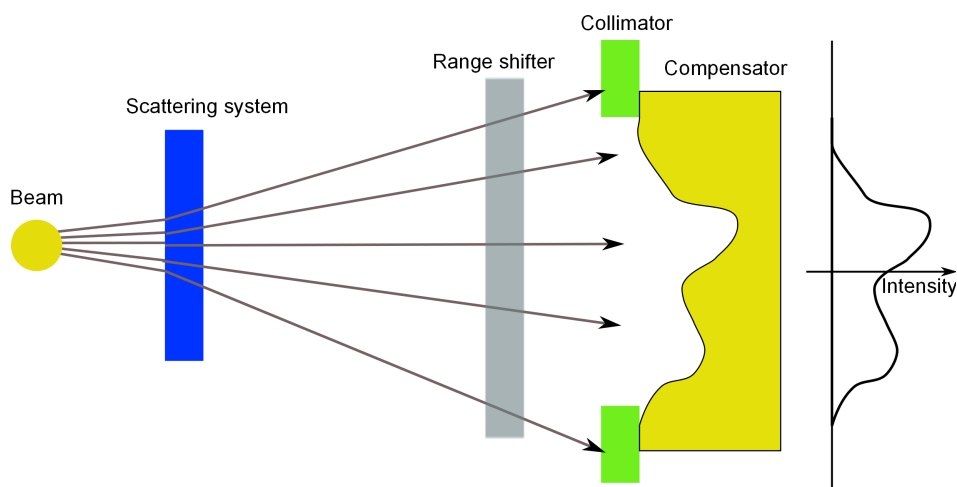


Figure 2.4.1: Passive beam delivery. Scattering foils spread the beam which is shaped by collimators and a compensator to match the target. A range shifter modifies the energy (range) of the particles.

In **active beam scanning**, the beam is laterally scanned across the target by a magnetic deflection system as shown in figure 2.4.2. For active energy variation the target is divided in isoenergy slices. The particles are accelerated to the required energy by the accelerator and the scanning system moves the beam through one isoenergy

slice. Once it is covered with spots the energy is changed to match the next isoenergy slice and the lateral scanning starts again. This procedure is repeated until all isoenergy slices are supplied with dose. This method can be applied for synchrotrons where the energy can be varied for every spill or also for cyclotrons using range shifter plates positioned upstream the patient surface within the beam's path. Using active beam scanning, two methods are applied nowadays: spot-scanning which has been developed at *Paul-Scherrer-Institute* (PSI) [Pedroni et al., 1995] where the beam is switched off while it moves to the next spot and raster-scanning developed at *Gesellschaft für Schwerionenforschung* (GSI) [Haberer et al., 1993] where the beam is on while continuously moving to the next spot. Newer methods such as continuous scanning where the beam is swept along a trajectory through a transversal plane while the intensity is varied, are currently investigated at PSI [Pedroni et al., 2004]. With 3D spot-scanning, full *intensity modulated proton therapy* (IMPT) is feasible [Lomax, 1999] meaning that the intensity of each single spot can be optimized so that the highest flexibility is achievable. The individual modulation of each spot allows for sophisticated delivery methods such as *Distal Edge Tracking* (DET). In DET, only one or several rows of spots along the lateral width of each slice are positioned at the rear end of the target. This reduces the number of spots and irradiation time while delivering a highly conformal dose to the target as proven by Nill et al. [2004]. In all active scanning methods, since pristine Bragg peaks with individual weights are delivered, the target can be shaped more precisely than by passive shaping with compensators resulting in a better sparing of healthy tissue and a high target dose coverage [Oelfke and Bortfeld, 2003]. Since the amount of material within the beam path can be drastically reduced compared to passive beam delivery dose losses are small and activation of material reduced.

Since active beam delivery cannot provide a continuous beam with variable energy on a timescale fast enough to avoid interference of beam and target motion, treatment of moving tumors with active scanning is more challenging. Even though the very precise shaping of the dose to a static target is one of the major advantages of active beam scanning, it is one of the greatest challenges for treatment of moving tumors since the sensitivity to organ motion is increased with active spot scanning. The problem of proton beam irradiation in the presence of tumor motion is discussed in section 2.5.

### 2.4.3 Treatment planning

Treatment planning is usually based on a CT (*Computed Tomography*) whose electron densities, represented by *hounsfield units* (HUs), can be converted into stopping power. In the planning process, the relevant target volumes are delineated in the CT. A physician prescribes the doses to the volumes of interest that, due to biological effects, most commonly are delivered in several fractions. Following the guidelines given by the *International Commission on Radiation Units and Measurements* (ICRU) ([ICRU report 50], [ICRU report 62], [ICRU report 78], [ICRU report 83]), the *Gross Tumor Volume* (GTV)

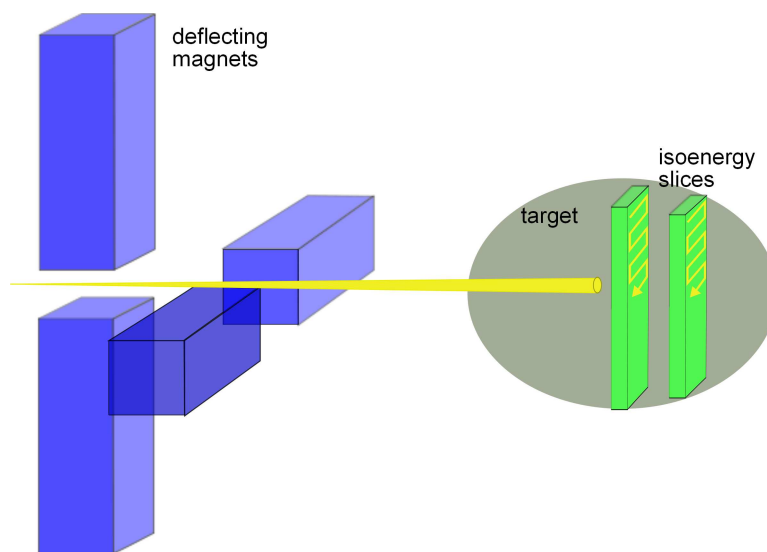


Figure 2.4.2: Active beam scanning. The beam is deflected by scanning magnets. For each energy the beam scans through one isoenergy slice.

comprising the visible tumor volume is defined. The GTV is expanded to a *Clinical Target Volume* (CTV) including suspected microscopic spread of the cancer. Additionally, setup-errors or motion induced geometric displacements are considered by the *Planning Target Volume* (PTV). In case of physiological motion and expected deformations as for lung or liver tumors the *Internal Target Volume* (ITV) must be added to the CTV. In addition to contouring of target volumes healthy tissue that might be affected by the radiation is delineated as *Organs At Risk* (OARs). According to [ICRU report 50], 100 % of the PTV volume should receive between 95 % and 107 % of the prescribed dose. In order to reach that goal the most crucial step is the optimization of beam weights. The degree of freedom differs depending on the delivery method applied. For passive beam delivery, where a uniform dose is applied to the target, the particle fluence can only be modulated by material in the beam's path. However, for active beam delivery methods such as spot-scanning each proton spot can be weighted by inverse planning techniques. Since the Bragg peaks can be modulated in three dimensions, IMPT provides the highest flexibility of beam shaping. In the following, this work will concentrate on active beam delivery. Hence, only the process of IMPT is described in detail in the following section 2.4.4.

## 2.4.4 Treatment planning for proton beams

In treatment planning for proton therapy, the energy, position and the number of protons delivered by each individual spot have to be determined. First, the spot positions for each individual Bragg peak are defined. This is usually performed by raytracing [Siddon,

1985] of the treated volume where the radiological depths are determined from the conversion of the HUs of the planning CTs into stopping power values. According to equation 2.1.2 the radiological path length for a given geometrical depth can be derived from the stopping power  $S(E)$ .

$$r_{rad}(E) = \int_0^E dE' \frac{1}{S(E')} \quad (2.4.1)$$

In this work, the optimization of all treatment plans is based on the inhouse treatment planning system 'KonRad' [Nill et al., 2004]. Dose calculations presented here were either performed with KonRad or the dose calculation algorithm developed within the scope of this work and described in 4.2. Both employ a pencil-beam algorithm in which the dose is divided into a central axis contribution of the dose and a lateral part according to equation 2.1.9. The central axis dose was measured for a broad proton beam. The resolution of data points around the Bragg Peak is 1 mm from which the dose value at the actual depth can be interpolated during dose calculation. The lateral distribution  $L(z, l_{x,ij}, l_{y,ij})$  accounts for the lateral spread of the beam due to scattering within the accelerator head and Multiple Coulomb Scattering (MCS) within the patient. For lateral distances of the central beam  $l_{x,ij}$  and  $l_{y,ij}$  for voxel  $i$  and spot  $j$ , and radiological depth  $d_{rad}$  the lateral distribution is given by

$$L(d_{rad}, l_{x,ij}, l_{y,ij}) = \frac{1}{\sqrt{2\pi\sigma_x'^2(d_{rad})}} e^{-\frac{l_{x,ij}^2}{2\sigma_x'^2(d_{rad})}} \frac{1}{\sqrt{2\pi\sigma_y'^2(d_{rad})}} e^{-\frac{l_{y,ij}^2}{2\sigma_y'^2(d_{rad})}}. \quad (2.4.2)$$

The  $\sigma$  is split into two parts:

$$\sigma_x'(d_{rad}) = \sqrt{\sigma_{x,0}^2 + \sigma_{MCS}^2(x)} \quad \sigma_y'(d_{rad}) = \sqrt{\sigma_{y,0}^2 + \sigma_{MCS}^2(y)}, \quad (2.4.3)$$

where  $\sigma_{x,0}$  accounts for lateral spread of the beam before entering the patient, caused by scattering within the accelerator nozzle.  $\sigma_{MCS}(d_{rad})$  comprises the MCS within the patient and is pre-calculated according to [Gottschalk et al., 1993].

The conversion of mass stopping power  $\frac{S}{\rho}$  into radiological depth  $d_{rad}$  takes into account density inhomogeneities according to equation 2.4.4.

$$d_{rad}(E) = \int_0^E dE' \left( \frac{1}{\rho} S(E') \right)^{-1} \quad (2.4.4)$$

To calculate the dose for a given voxel  $i$   $d_i$ , the dose is stored in a dose influence matrix  $D_{ij}$ . Each element of the  $D_{ij}$ -matrix stores the dose contribution for a given spot  $j$  to a voxel  $i$ . The dose of all spots  $N$  is superimposed and weighted by the individual spot weight  $w_j$ .

$$d_i(d) = \sum_{j=1}^N D_{ij} w_j. \quad (2.4.5)$$

In IMPT, where inverse planning is applied, the optimal number of protons for each beam spot is determined through an iterative optimization of a cost function characterizing the difference between the desired dose and the dose calculated at the current step of the optimization. The performance of the dose optimization and dose calculation steps of KonRad can be studied in more detail in the publication by [Nill et al. \[2004\]](#).

## 2.5 Treatment of moving organs with protons

With modern proton beam delivery techniques such as active beam scanning and IMPT the physical advantages of proton beams could be fully exploited for the treatment of static tumors [[Lomax, 1999](#)]. The increased accuracy of the delivery combined with the physical behavior of protons when transversing through matter allows for improved target coverage of tumors while sparing surrounding healthy tissue. While active scanning methods have the potential to better conform the dose to the target volume than passive beam delivery for static targets, this holds no longer true in the presence of target motion. Due to the motion of the target and the beam it might occur that the tumor moves partwise or completely out of the beam. Thus, the interfering beam and target motion can lead to severe miss-dosage. Therefore, the application of active spot-scanning and its increased accuracy are mainly applied for static targets up to now. However, many organs are affected by organ motion. So far, only passive beam delivery where the problem of motion can be handled by the use of margins covering the tumor in all motion states is used for treatment of moving tumors with particles. However, margins are not fully exploiting the beneficial physical behavior of protons in matter. Margins are a treatment planning concept commonly used in photon therapy that show an exponentially decreasing dose fall off with increasing depth in tissue. For protons and heavier ions that loose their energy through direct ionization when traversing matter, margins are used to account for setup errors and also in case of organ motion for passively scattered particles. Also, misregistration of the range compensator and the patient, in organs where density variations are particularly high as in the lung, are taken care of by smearing through modifying the thickness of the compensator [[Engelsman and Kooy, 2005](#)].

In order to exploit the advantages of active beam delivery to moving tumors the investigation of motion mitigation techniques as well as accelerator developments are subjects of particular interest in particle therapy. In the following sections motion in radiation therapy (2.5.1) and it's consequences (2.5.2) to the dose distribution are described. Motion management strategies are introduced in 2.5.3.

## 2.5.1 Organ motion in radiation therapy

Organ motion within the patient's body appears on various time scales and extents. The motion and thus the tumor position can vary during the course of irradiation, between individual fractions (*interfraction motion*) and within the delivery of one fraction (*intrafraction motion*) [Paganetti, 2012].

Motion appearing during the course of treatment is related to shrinkage or growth of the tumor [Britton et al., 2007], weight loss or gain of the patient as well as bowel or rectum filling. Also, different patient positions in different treatment sessions can cause different organ positions. However, patient position related motion can be handled by careful patient positioning and verification of the position in relation to the planning CT, and thus will not be further discussed in this work.

**Interfractional motion** typically happens on a day-to-day level but can also appear between hours or minutes. It often affects organs of the digestive tract or those close to [Langen and Jones, 2001]. Different fillings of the bowel and rectum (or bladder) cause the affected organs to change their shape and neighboring organs such as the prostate to move [Fokdal et al., 2004]. Also shrinkage of the lung and variations in the breathing amplitude or baseline drifts can occur from fraction to fraction [Sonke et al., 2008].

**Intrafractional motion** happens on a timescale smaller than the delivery time of one fraction of the prescribed dose. Typical organs subject to intrafractional motion are respiratory organs and organs close to the diaphragm such as the liver and the heart. A large contribution to the movement of the abdomen is given by respiration. The largest extent of motion due to respiration is observed in the superior-inferior (SI) direction [Langen and Jones, 2001], [Seppenwoolde et al., 2002]. Due to the motion pattern of the lung, organs attached to the diaphragm or close by experience the largest extent of motion. Maximum peak-to-peak values up to 3 cm for lung motion in SI direction have been found. However, the average amount of motion is below 1 cm [Paganetti, 2012]. In left-right (LR) and anterior-posterior (AP) direction motion is often less than a few millimeters [Seppenwoolde et al., 2002]. Due to being positioned in the direct neighborhood of the diaphragm, the liver is also affected by breathing motion. The extent of lung and liver motion has been summarized in detail by [Shirato et al., 2004]. They reported peak to peak values of 19 mm in SI direction. Also the prostate underlays variation of position due to spontaneous gas movements within the rectum. However, intrafractional changes in the position of the prostate are typically below a few millimeters ([Stroom et al., 1999], [Kupelian et al., 2007]).

## 2.5.2 Consequences of organ motion for proton beam therapy

Even though protons and other particles allow to shape the dose precisely to the tumor, organ motion can seriously confine the advantages of this technique. Physiological organ motion can cause movement of the tumor and the surrounding tissue,

which can have debilitating effects on the dose distribution because the tumor might be shifted partwise or completely outside the planned treatment field. The motion induced anatomical changes lead to blurring and spatial deformation of the dose and are independent of the delivery method [Bortfeld et al., 2004]. This effect is not specific to proton beams and can be dealt with by fractionated delivery of the dose and the application of multiple fields [Bortfeld et al., 2004]. Additionally, the dose distribution can be harmed by motion induced density changes and, in case of active scanning methods, the beam motion can interfere with the target motion. Both effects are described in the following sections 2.5.2.1 and 2.5.2.2.

### 2.5.2.1 Density changes

One of the reasons for the detrimental effects on the dose distribution are density changes in the beam path due to organ movement. As explained in detail in section 2.1, the changes in the density influence the particles path length. While the impact of density changes on the dose in photon therapy is rather small, in proton beam therapy it gets more pronounced due to the Bragg peak and the finite range of particles in tissue. For a single uniform field (SFUD) this effect is concentrated to the edges of the tumor where the dose gradients are steepest. In IMPT where the individual fields might be very different, density changes can also affect the dose in the middle of the tumor. In a study by Mori et al. [2009] average range fluctuations up to 21.8 mm-WEPL (water equivalent path length) in lung over an entire breathing cycle were reported. Severe changes of path length in lung due to motion were also reported by Bert and Durante [2011]. The consequences of range uncertainties with respect to dose for a lung tumor were studied by Hui et al. [2008]. For the majority of cases studied they found a rather minor reduction of target coverage while organs at risk were found to suffer from a 4 % increase of the dose. Significant reduction of CTV dose as an effect of a combination of a setup-error of 5 mm and a breathing amplitude of 10 mm was found by Engelsman and Kooy [2005].

Currently, density effects are taken care of by the use of safety margins and by smart treatment planning on 3DCTs. Furthermore, in 4D treatment planning, which is based on a 4DCT and adaptation of planning parameters to the changes, motion induced anatomical and resulting dose variation can be partially incorporated in the treatment plan [Bert and Rietzel, 2007].

### 2.5.2.2 Interplay effects

Modern delivery techniques employing a moving proton beam such as active spot-scanning can deliver a highly conformal dose distribution to a target volume. However, this advantage is currently limited to static targets. For moving targets the motion of the beam might interfere with the target motion and can cause unintended distortions of

the dose distribution. Active spot-scanning has been applied only in very few cases for moving targets. Rinecker Proton Therapy Center (RPTC) treats thoracical and adominal tumors using apneic oxygenation to mitigate breathing induced motion during treatment with a scanning proton beam [Bert and Durante, 2011]. The Heidelberg Ion Therapy center (HIT) recently reported treatment of patients suffering from hepatocellular carcinoma (HCC) using a vacuum pillow as patient immobilization and abdominal pressure. One patient was treated with beam gating (2.5.3.2) [Habermehl et al., 2013]. Patients for treatment of prostate cancer with protons and Carbon Ions are currently being recruited [Combs and Debus, 2013]. Interplay effects due to their nature can only occur for non-static beam delivery where the time scale of beam and target motion can interfere. In active beam delivery systems one isoenergy slice can typically be scanned within 100 - 300 ms, while the time to change the energy and fill the synchrotron with particles is in the range of seconds (1 - 5 s). Since breathing with typical breathing periods of 3 - 6 s happens on the same time scale, organs affected by breathing motion can suffer from interplay effects.

The distortion of the dose resulting in an increased inhomogeneity of the dose is caused by more or less overlapping adjacent spots due to the motion of the beam and the target. This process is visualized in figure 2.5.1. Of course, this can result in severe over- and underdosage of the target and organs at risk. While in the target cell-damage can be insufficient, surrounding healthy tissue might suffer from an increased dose, thus leading to increased risk of side effects of radiation therapy.

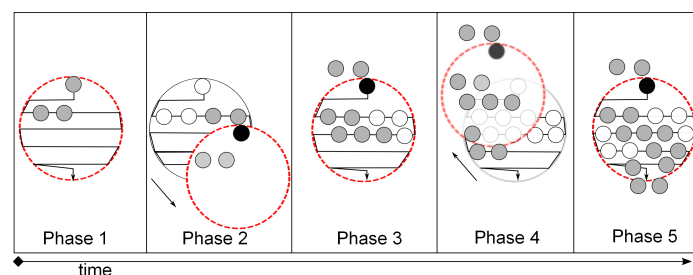


Figure 2.5.1: Schematic drawing of interplay effects. The target moves while the beam is scanning through one isoenergy slice. While the tumor is in motion phase 1 the spots are correctly positioned as planned (on phase 1) (grey). In a different phase the tumor might have moved partwise out of the irradiation field resulting in hot (black) and cold (white) spots. (adapted from Bert et al. [2008])

Interplay effects have now been studied for quite a long time [Bortfeld et al., 2004], [Blattmann and Coray, 1990], [Lambert et al., 2005], [Bert et al., 2008], [Furukawa et al., 2010], [Kraus et al., 2011], [Zenklusen et al., 2010], [Knopf et al., 2011]. Motion parameters and their influence on the quality and magnitude of interplay effects have also been investigated by several researchers. The majority of results showed a strong

impact of motion amplitude and/or baseline drifts on the dose homogeneity and target coverage [Phillips et al., 1992], [Bert et al., 2008], [Kraus et al., 2011]. The study of Bert et al. [2008] revealed also a strong correlation of the periodicity of motion and initial phase of irradiation with the effects on the dose distribution. In this work, machine specific parameters were also investigated. The lateral scan time was found to be a relevant factor for interplay effects [Bert et al., 2008]. Furukawa et al. [2010] investigated a fast scanning system for phase-controlled rescanning and gating and found dose differences less than 2 % compared to a static delivery.

Interplay effects cannot be completely compensated by the use of margins [Lambert et al., 2005]. In newer studies margins accounting for target motion and changes in the radiological path length were found to generally improve the dose distribution compared to the use of CTVs, though [Knopf et al., 2013]. Including the variations of radiological path lengths only resulted in slight improvements of the target dose but increased dose to healthy tissue. Therefore, other motion mitigation and management strategies to be applied in addition to an adequate safety margin have to be further investigated. Details on motion management are described in the following section 2.5.3.

### 2.5.3 Motion management

The accuracy of proton therapy is hampered by the inability to track the tumor during dose delivery. Therefore, various methods have been developed to assess the tumor motion. In section 2.5.3.1 a brief summary on existing motion monitoring methods is given. For radiation therapy of moving tumors different methods to mitigate the motion and strategies to deliver the dose have been developed. These are described in section 2.5.3.2.

#### 2.5.3.1 Motion monitoring

Motion monitoring can be divided into direct measuring of the tumor position and measuring of a tumor motion surrogate. Direct motion monitoring systems include fluoroscopy, ultrasound and radiofrequency transponders implanted inside the tumor.

In fluoroscopy, which is basically a 2D x-ray image, the photon beam is attenuated on its path through the patient's body and detected by a fluoroscopic screen often available in a conventional treatment room. The position of a fiducial marker implanted in or close to the tumor is detected [Shirato et al., 2003]. This method provides time resolved 2D position information and is often used in x-ray guided surgery. However, it gives additional radiation to the patient and for 3D image acquisition even more than one projection is required. Also the dose in the target can suffer from the implanted markers in particle therapy [Jäkel, 2006]. This holds true for motion monitoring through implanted sensor coils within an electromagnetic field studied by Seiler et al. [2000]. Electromagnetic transponders commercialized by Varian Medical Systems have been

proven for motion monitoring of the prostate ([Willoughby et al., 2006]) and are currently studied for their application in lung tumor motion detection [Shah et al., 2013]. Recently, the Calypso System is used at Roberts Proton Therapy Center (University of Pennsylvania, USA) for pre-clinical studies [CALYPSO MEDICAL, PRESS RELEASE]. For lung tumors, however, the signal of the transponders does not measure the real tumor position because the beacons are not directly implanted within the tumor tissue. Electromagnetic transponders can effectively measure the tumor or internal organ motion without delivering of additional dose.

In the interest of sparing the patient from overdosage, also other non-ionizing imaging methods for motion detection are emerging. *Magnetic Resonance Imaging* (MRI) within the treatment room has been proposed by Lagendijk et al. [2008] for photon irradiation. This is a promising, though challenging approach even for photon beams. For proton beams the problem of beam deflection is not resolved yet. However, there are endeavors to exploit the behavior of protons in matter in combination with a magnetic field on a theoretical basis up to now. Whereas Raaymakers et al. [2008] found the influence of a 0.5 T magnetic field on a proton beam to be minor, [Wolf and Bortfeld, 2012] calculated beam deflections greater than 1 cm depending on the initial energy. Lattanzi et al. [1999] studied ultrasound for position acquisition of the prostate. In later studies the accuracy of ultrasound for thoracical and abdominal motion detection was assessed and found to be comparable to fluoroscopic accuracy [Harris et al., 2010].

Of course, time resolved *Computed Tomography* (4DCT) is also an option to acquire spatio-temporal information. However, similar to fluoroscopy, continuous motion monitoring throughout the entire irradiation is not applied due to the additional dose delivered to the patient. However, 4DCTs can provide important motion information for treatment planning in case of periodic motion. In order to acquire a 4DCT the motion cycle (i.e. breathing cycle) is divided into motion states. A surrogate motion detection system triggers the acquisition of a CT scan over the motion cycle resulting in several 3DCTs correlated with the motion information along the motion trajectory. A 4DCT can be used for delineation of the volumes of interest and margin assessment as indicated in section 2.4.3.

Besides direct imaging methods, there is also the possibility to measure a surrogate motion signal such as lung volume filling or motion of the chest wall instead. The main drawback of this method is its dependency on the correlation of the surrogate motion signal and the tumor motion. Due to its relatively easy applicability, this is currently used in clinical practice. One method is putting a pressure belt around the patient's torso to measure the expansion of the thorax due to breathing. As described above this method can be used for the acquisition of 4DCTs but also potentially for gated irradiation. The commercialized version by Anzai Medical Co. LTD 'AZ-733V' has been used for motion acquisition for the cases reported within this work.

Surrogate motion monitoring based on an infrared signal for gated heavy ion therapy has also been investigated by [Minohara et al., 2000]. An infrared light emitting

diode is put onto the patient's chest wall and its signal detected by a position resolved detector. The signal is fed back to request beam from the accelerator as required for gated irradiation. Another optical motion monitoring system was investigated by [Baroni et al. \[2000\]](#). Charged coupled device (CCD) cameras equipped with infrared light emitting diodes (LED) are positioned at the ceiling of the treatment room and send infrared light flashes. These are detected by small electronic circuitries positioned on the patient's surface to measure surface motion in real time. Furthermore, this method was used for motion detection in combination with deep inspiration breath-hold technique for stereotactic treatment of lung and liver tumors. Position reproducibility was below a few millimeters for inter- and intra-breath-hold motion detection.

These, and other optical motion measurement systems are also often used in combination with ultrasound imaging to register the position in the treatment room [[Yan et al., 2002](#)]. Other systems measure the contour with the laser in the treatment room on the patient surface [[Wilks and Bliss, 2002](#)].

Furthermore, both - direct and indirect motion acquisition methods can be combined to avoid their main disadvantages. Prediction models are used to determine the internal target motion based on data acquired via training of the algorithm and triggered by external motion information. The Cyberknife Synchrony (Accuray, Sunnyvale, CA) already uses such a model based approach of motion monitoring [[Nioutsikou et al., 2008](#)].

### **2.5.3.2 Motion mitigation and dose delivery strategies**

One approach to overcome the motion induced detrimental effect on the dose distribution is to reduce the extent of motion. There are various methods to decrease the magnitude of motion. In the following a brief overview on existing techniques is given.

#### **Motion immobilization strategies**

One way to reduce the abdominal motion amplitude is by putting a pressure plate onto the patient's abdomen during treatment. Due to the strong pressure the residual motion of the diaphragm is reduced. [Negoro et al. \[2001\]](#) studied the effectiveness of a stereotactic body frame with an abdominal pressure plate applying pressure if the tumor motion exceeded 5 mm measured via fluoroscopy. The maximum motion amplitude thereby reduced to almost half of its original extent. Even though the residual motion is significantly reduced, one has to bear in mind that due to the device mounted around and onto the patient, treatment planning can be harmed due to less available beam directions. For organs affected by the motion of the digestive tract the magnitude of motion can be limited by using gas or water filled rectum ballons [[Smeenk et al., 2010](#)]. This method is used for treatment of prostate cancer with photons as well as protons [[Bert and Durante, 2011](#)]. Furthermore the position of organs close to the bladder or

rectum can be influenced by dietary protocols and controlled filling status of rectum and bladder at the time point of treatment ([[Mayahara et al., 2007](#)], [[Nihei et al., 2005](#)]).

### **Breath-hold techniques**

Another possibility to control breathing induced displacement of the tumor is by active breathing control and deep-inspiration breath hold (DIBH) [[Hanley et al., 1999](#)]. The patient breathes through a mouthpiece while the volume of air is measured. In the latter approach the patient is triggered to hold breath while radiation is delivered. The breath-hold elongates the time the tumor is in an almost stationary position and radiation delivered. Of course, one can imagine, that especially pulmonary comprised patients have difficulties to hold their breath. [Hanley et al. \[1999\]](#) reported that patients were able to comfortably hold breath for up to 16 s. In active breathing control [[Wong et al., 1999](#)] irradiation is triggered by preselected respiration levels measured through controlled air volume during breathing. In addition, immobilization of the tumor through jet-ventilation or even apnea is used. For proton therapy the later approach has already been applied at RPTC.

### **Gating**

In gating, which has already been installed in several particle therapy centers, the beam is paused as long as the motion is outside a pre-defined motion window [[Ohara et al., 1989](#)]. The gating can be phase or amplitude controlled, meaning that the tumor is either irradiated within a certain motion phase or if its displacement is within pre-defined borders. For beam-on-time often the maximum exhale phase is chosen since it is considered to be best reproducible due to relatively small residual motion. Obviously, the duty cycle of the beam is significantly reduced, thus the irradiation time increases.

Dose delivery with a scanning beam to a moving tumor still remains challenging due to the interference of the scanning beam with the residual motion within the gating window. However, HIT recently published data on the treatment of hepatocellular carcinoma (HCC) with respiratory gating combined with an ITV margin comprising the tumor during the whole respiratory cycle [[Habermehl et al., 2013](#)]. To overcome the problem of interfering beam and target motion, gating can be combined with other motion mitigation techniques such as margins, as in the referred patient case at HIT or rescanning [[Furukawa et al., 2010](#)].

### **Rescanning**

A different approach to handle intrafractional tumor motion during treatment with scanned particles is rescanning, also referred to as repainting [[Phillips et al., 1992](#)]. Whereas

gating confines the motion to a pre-defined gating window and thereby reduces the extent of motion, rescanning averages out local misdosages on the costs of small dose deviations to a larger volume. Delivery of the entire prescribed dose in multiple fractions has already an averaging effect on local dose discrepancies [Bortfeld et al., 2002]. Also, delivering from multiple field directions was found to average out local deviations of the dose [Knopf et al., 2011]. Since the statistical error of the dose in a point decreases with the square root of fractions (rescans), additional fractionation of the dose within one treatment session further reduces dose distortions and is referred to as rescanning. However, since the dose averaging is a statistical process, an increased number of fractions does not necessarily lead to improved dose distributions. Unfortunate combination of the beam delivery and target motion can harm the effectiveness of rescanning. Therefore, careful consideration of the scan speed and direction with respect to the motion pattern is required. Rescanning can only average out local misdosages if the motion and delivery patterns do not coincide for the different rescans. Even though, in principle rescanning is independent from patient motion information, for some delivery strategies motion acquisition might be required. In order to avoid the effect of matching motion patterns from rescan to rescan Furukawa et al. [2007] proposed a method which aims at spreading of rescans to an entire breathing cycle. In a later approach this so called phase-controlled rescanning was used in combination with gating [Furukawa et al., 2010]. Thereby, the extraction rate of the synchrotron must be adjusted to ensure delivery of one isoenergy slice within the duration of one gating window. The results of Furukawa et al. [2010] revealed that phase-controlled rescanning in combination with gating has the potential to deliver a homogeneous dose distribution with 2 % deviation from a statically delivered dose distribution. An alternative approach to deal with detrimental timing patterns of subsequent rescans are random time delays between the individual rescans or random choice of energy slices for volumetric rescanning as proposed by Seco et al. [2009].

There are various rescanning strategies that can be divided into volumetric and non-volumetric methods. In non-volumetric rescanning each slice is rescanned until the preselected number of rescans is reached, then the energy is changed and the procedure is repeated for the next isoenergy slice. In contrast to this, the entire volume is scanned at each rescan in volumetric rescanning. Which method is used, depends on the time structure of the applied delivery and thus on the accelerator technique used. One can imagine that synchrotrons are not suited for volumetric rescanning due to large energy change times within the range of a few seconds. However, researchers from HIMAC (*Heavy Ion Medical Accelerator*, Japan) investigate a single cycle synchrotron able to change the energy within one acceleration cycle, thus avoiding long energy change times. Also, along with the development of novel accelerator techniques, as described in section 2.3 more favorable timing structures for rescanning can be achieved.

Zenklusen et al. [2010] studied also different delivery strategies for rescanning that are referred to as scaled repainting and isolayered repainting. In scaled repainting the

dose per fraction scales with the number of rescans, whereas in isolayered rescanning the number of rescans is proportional to the number of protons for each spot. The latter approach is characterized by inhomogeneous spot patterns that can result in different beam paths for each rescan. However, this method comprises the possibility to control the number of spots delivered with each spot avoiding the problem of low particle numbers that can be a technical limitation [Bert and Durante, 2011]. The study of Zenklusen et al. [2010] revealed that isolayered rescanning might be preferred for treatment of tumors moving less than 5 mm with spot scanning. For treatment of tumors exceeding an amplitude of 5 mm they proposed to combine rescanning with another motion encompassing method such as gating or breath-hold techniques.

It has been proven that rescanning is technically feasible in various studies. However, there are also some drawbacks to this method. Rescanning does not suppress the motion and consequently all peculiarities coming along with motion have still to be dealt with during imaging and treatment planning [Paganetti, 2012]. As a matter of fact, rescanning increases the treatment time, combined with gating the method might even experience the limitations of applicability with regard to time during daily clinical routine.

### **Beam tracking**

In contrast to rescanning, beam tracking tackles the problem of motion directly by synchronous correction of the beam position for the displacement of the tumor in real-time. It possibly is the most sophisticated motion management technique but also technically most challenging. Originally, beam tracking was proposed for photon beam irradiation [Keall et al., 2001] and has already been applied in the Cyberknife Synchrony system (Accuray Inc, Sunnyvalke, CA) for x-ray radiosurgery [Nioutsikou et al., 2008]. At GSI comprehensive studies have been examined to investigate beam tracking for scanned Carbon ion beams from a technical as well as dosimetric point of view ([Grözinger et al., 2004], [Bert et al., 2007], [Bert et al., 2010], [Saito et al., 2009], [Chaudhri et al., 2010]). A full tracking system has been integrated and tested. Lateral adjustment is performed by the scanning magnets, whereas a motor-driven wedge system is used for longitudinal range adaptation [Weber et al., 2000]. Comparison of dose distributions achieved for a moving tumor and beam tracking with a stationary tumor showed good agreement with deviations less than 1 % [Bert et al., 2010]. Though, beam tracking is technically feasible, it has not been applied for radiation therapy with scanned particles, yet [Riboldi et al., 2012]. It relies on real-time position information during treatment, however, the 4D imaging data in clinical routine is acquired hours or even days before the treatment. Therefore, real-time 4D imaging and fast plan adaptation is needed for its clinical use. Furthermore, in order to correct for changes of the particle ranges, a pre-calculated range correction has to be performed on each motion phase prior to treatment. This is based on 4D CTs using image registration which is still an element of uncertainty.

In conclusion, beam tracking is - from a physical point of view - the best method to deal with the problem of organ motion. A further improvement can be obtained by combining it with rescanning, since statistical fluctuations can be averaged out when the tumor is rescanned about 10 times and, moreover, any error made in one scan can potentially be compensated in a next one.



## Chapter 3

# TULIP - TUrning LInac for Proton therapy

### 3.1 Introduction

In section [2.2](#) the various proton accelerator techniques and machines currently used or investigated for hadron therapy are described. This section describes a novel accelerator system for proton therapy called "TULIP" (*TUrning LInac for Proton therapy*) designed and patented by TERA [[Amaldi et al., 2008](#)] and introduces the reader into the scope of this work.

#### 3.1.1 Motivation

About 10000 patients are treated with protons per year summing up to total number of about 100 000 patients who will have been treated with protons by the end of 2013. However, the number of available proton therapy facilities is restricted. Currently, there are about 40 operating centers worldwide offering proton therapy. For Carbon ions the situation with respect to availability is even worse. All proton facilities in operation nowadays are based on cyclotrons and synchrotrons. For carbon ions or even heavier particles synchrotrons are the only available option up to now. Besides the technological advantages and disadvantages listed also in section [2.2](#) there are major restrictions for these types of accelerators preventing widespread application in medicine as they are: they require large space and come along with high costs up to 130 Mio Euros. Therefore, most of today's hadron therapy facilities are so called multi-room centers employing one particle accelerator whose beam is used in several treatment rooms allowing for radiation therapy of about 400-500 patients per year in each room [[Amaldi et al., 2008](#)]. To spread hadron therapy and increase the availability of particles for radiation therapy throughout the world apart from large and cost intensive multi-room centers, researchers in research centers as well as in commercial industry have started to design

and construct so called 'single room facilities' [Amaldi et al., 2010]. Part of these efforts is the development of compact accelerators with reduced costs that can be integrated into smaller or even existing rooms for electron linacs at hospitals without the extensive and elaborate installation of an entire new hadron therapy center. TERA foundation has patented a novel proton acceleration system for medical application [Amaldi et al., 2008] which will be described in the following since it is the basis of this work. TULIP has the potential to fulfill the requirements for single room facilities as they are the cost of the high-tech part of such a single room facility will be approximately 30 Million Euros with a 400 m<sup>2</sup> area (shielding included) and this without making compromises on the physical and/or clinical benefits of proton therapy. The system involves a pre-accelerator (cyclotron) and a linear accelerator mounted on a gantry rotating around a patient capable of active proton scanning. Details on the accelerator, the design and output of this machine are described in the following sections 3.1.2 and 3.1.3. Due to highly innovative accelerator technique and sophisticated design the system will be massively reduced in size and costs compared to large cyclotron or synchrotron facilities.

In this work, the dose delivery of TULIP is investigated. In this chapter, first dose delivery to static targets with TULIP is analyzed. Details on the hardware conditions concerning dose delivery are described in chapter 4.

### 3.1.2 TULIP - Design

TULIP is a high frequency linear accelerator mounted on a gantry capable to rotate around the patient and deliver protons via active beam scanning.

There are many relevant parameters to be considered when designing a particle accelerator. The TULIP specific parameters are summarized in table 3.1.1.

For high gradient operation one of the most crucial choice is the RF frequency (S-Band (2998.5 MHz) or C-Band (5712.0 MHz)) which has been carefully investigated by Degiovanni et al. [2011], Andres et al. [2012] and Amaldi et al. [2012]. For TULIP S-band showed to be superior compared to the C-band design in terms of total length and beam performance. Also, the commercially available power sources operating at the desired frequency play an important role for the design. The maximum energy of 230 MeV has been chosen to meet the required therapeutic goals for most of the occurring tumors. In order to reduce the costs a 24 MeV cyclotron, equipped with an external proton source, has been chosen as injector, even though in previous designs other cyclotrons with maximum energies above 30 to 35 MeV have been considered. Also the number of modules, tanks per module and cells per tank is subject of development since they affect the length and energy gain of the accelerating section. To suffice and realize the changes in the hardware parts, the support system and overall structure has been adapted several times. In figure 3.1.1 different versions of Tulip in the time line of development are shown. The most recent design is shown in figure 3.1.2. While in the previous versions of TULIP the linear accelerator was divided into several sec-

<b>General Parameters</b>	
RF frequency [MHz]	2998.5 (S-Band)
Number of units	11
Number of tanks	28
Number of cells	396
Maximum peak surface electric field [MV/m]	159
Maximum peak magnetic field [kA/m]	81
Average axial gradient in the cells [MV/m]	22.3-32.2
Iris diameter [mm]	6.0
Total linac length [m]	11.1
Input Energy [MeV]	24.0
Output Energy [MeV]	230.0
Energy steps per unit	11-25
<b>Energy Consumption</b>	
Peak power needed per RF unit [MW]	6.3 - 8.0
Total peak power needed [MW]	92
<b>Transverse Focusing System</b>	
Number of Permanent Magnetic Quadrupoles (PMQs)	29
Magnetic field gradient of PMQs [T/m]	176-120
Length of PMQs [mm]	33.0
Diameter of PMQs [mm]	7.0
<b>Beam Performance</b>	
Repetition rate [Hz]	120
Duration of the RF pulse at the flat-top [ $\mu$ s]	1.6
Transversal magnet scan speed [m/s]	5-10
Lateral field size [cm <sup>2</sup> ]	20x20
Normalized transverse acceptance [ $\pi$ mm mrad]	1.9
Normalized longitudinal acceptance [ $\pi$ deg MeV]	8.7
Total transmittance [%]	6.3
Average beam current [nA]	1.0

Table 3.1.1: TULIP specific design parameters.

tions with different directions, the most recent design holds only two subsequent linear accelerating sections directly attached to each other. After preacceleration, the beam is focused by quadrupole magnets in the High Energy Beam Transfer line (HEBT) and directed into the accelerating section. Two bending magnets bend the beam towards the patient while two scanning magnets move the beam across the tumour covering a treatment field of  $20 \times 20 \text{ cm}^2$ .

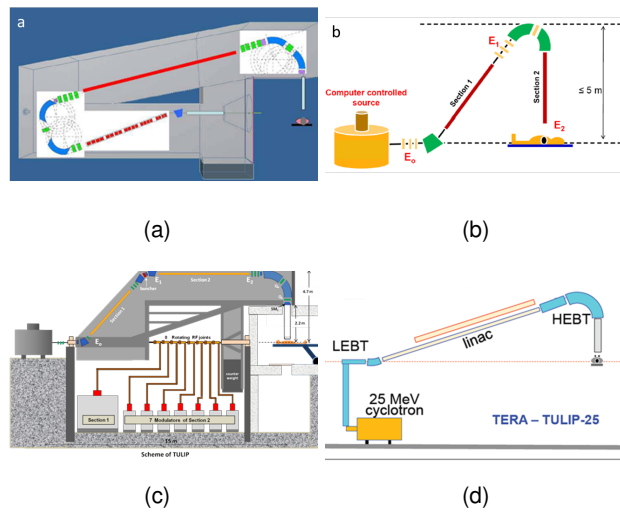


Figure 3.1.1: Schematic drawing of previous versions of TULIP designs. Picture (a) shows the first proposal for the TULIP design of 2006. The entire accelerator is mounted in a gantry. (b) shows an idea where the linear accelerating part is divided into two sections and the final linac points to the patient. In (c) a trapezoidal layout of the supporting structure has been chosen. The gantry rotates around the patient from  $0$  to  $330^\circ$ , no lateral beam scanning is applied. In picture (d) a simplistic sketch of the most recent design is presented. Both accelerating units are put subsequently on the gantry transporting the beam in the same direction. To save space the cyclotron is positioned below the gantry. The gantry rotation is limited to  $220^\circ$  and the beam can be laterally scanned.

### 3.1.3 TULIP - accelerator and beam line

The cell coupled linac is based on the cyclinac concept described in section 2.3.3. The protons are pre-accelerated by a 24 MeV cyclotron and then are guided by the Low Energy Beam Transport channel (LEBT), where the beam is shaped to match the required transverse acceptance. Since no energy variation is envisioned within the LEBT it can

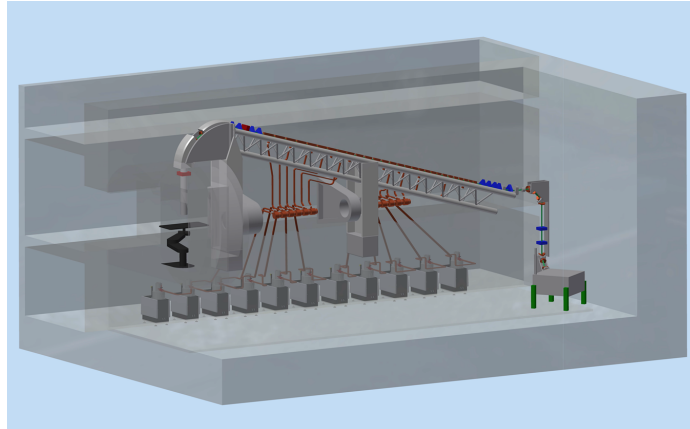


Figure 3.1.2: Drawing of the most recent TULIP design. The accelerating parts of the linac are mounted on a gantry which can rotate  $\pm 110^\circ$  around the patient. A 24 MeV cyclotron serves as injector to the linac. The patient is positioned on a robotic couch which can be rotated in all directions around a vertical axis. 11 accelerating units are fed by individual klystrons that are connected via rotating joints to the RF accelerating structures.

be made of permanent quadrupole magnets. After the LEBT protons with an energy of 70 MeV are accelerated up to 230 MeV in the linac, before they enter the High Energy Beam Transport section (HEBT). Within the HEBT the particles are focused and bent by 4 quadrupoles, 2 bending magnets and 2 scanning magnets and accelerated to their final energy up to 230 MeV. The accelerator itself consists of 11 RF units with 28 tanks for a total of 296 accelerating cells giving the linac an overall length of 11 m. Each unit is independently powered by an individual klystron with a repetition rate of 120 Hz that produces 3 GHz power pulses [Degiovanni et al., 2011]. Each pulse is about 1.5-2.5  $\mu\text{s}$  long which corresponds to a duty cycle of 0.04%. In high gradient tests of a prototype at 3 GHz, gradients of 35 MV/m with a surface field of 170 MV/m to accelerate the protons could be reached [Amaldi et al., 2012]. At these high gradients a breakdown rate of about  $2 \cdot 10^{-6}$  bpp/m was measured, which corresponds to a breakdown every 400 seconds for a repetition rate of 120 Hz and a length of approximately 10 m. The high repetition rate holds the potential of very fast active energy variation on a pulse-by-pulse basis by modulation of the klystron input power. The beam intensity can also be changed every pulse by a computer controlled source. These characteristics make TULIP suitable for fast dose application with protons to tumours. Furthermore, energy and intensity variation within milliseconds hold the potential to treat moving tumors with protons. A waveguide system transports the power from the 11 klystrons to the linac modules. Since the linac is rotating while the klystrons are statically mounted on the ground, rotating joints proposed by I. Syratchev (CERN) are required. The first three

modules, that are responsible for acceleration of protons to a fixed energy of 70 MeV, consist of 4 tanks with a number of cavities (13-17). The rest of the modules comprise 2 tanks each to allow for energy variation by amplitude and phase variation of the klystron power. The linac (both subsequent sections) mounted on the gantry is about 11 m long. It can rotate around the patient covering an angle segment of  $\pm 110^\circ$  like competitive systems (*ProteusOne* (IBA), MEVION S250) mentioned in section 2.3.3. To increase the degrees of freedom for radiation therapy treatment the patient couch is mounted on a robotic arm which allows rotation around a vertical axis in any direction. The beam is delivered throughout the tumor by 2 scanning magnets allowing for a  $20 \times 20 \text{ cm}^2$  field to be covered by the magnetic scanning. For the most recent design we assume a lateral magnet scan speed of 5 to 10 m/s. For the previous designs, no lateral scanning was envisaged, since the beam was supposed to rotate around the patient for a total angle equal to  $330^\circ$ .

# Chapter 4

## Static proton dose delivery with TULIP

Throughout the time of development of TULIP there have been different design proposals that led to two conceptional different dose delivery techniques. Both systems were investigated and will be described in the following.

Since TULIP is a modular linear accelerator it is predestinated for active energy variation on a milliseconds scale by variation of the power levels and the phases of the klystrons. A repetition rate of maximum 120 Hz allows for energy variation within 8.3 ms. A momentum acceptance of the bending magnets allows for fast energy variation within a proton range in matter of roughly 7 %. Larger energy steps require the adjustment of the magnet current within the HEBT section which can happen within 100 ms. The energy range is limited by the LEPT output energy (70 MeV) and maximum energy of the HEBT (230 MeV). Two scanning magnets move the beam across a field of 20 x 20 cm<sup>2</sup> with a scanning speed of 5 to 10 m/s. The intensity (number of protons) can also be varied on a pulse-by-pulse basis with a precision of 3 %. However, due limitations of the proton source, the maximum number of protons per pulse is limited to  $5 \cdot 10^7$ . These machine specific physical parameters allow for fast intensity modulated beam delivery. Two conceptionally different beam delivery methods could be thought of: rotational proton therapy and 3D spot scanning. These dose delivery methods have been studied with regard to resulting dose distributions and performance (irradiation time). For this purpose a C++ based simulation software has been developed. The first part of this work describes the development and mode of operation of this software (4.1) as well as dosimetric results for the delivery to a stationary tumor with rotational proton therapy and 3D spot scanning (4.2).

### 4.1 Dose Delivery Simulation Software

In order to study proton dose delivery based on a novel accelerator design, a C++ based algorithm has been developed to simulate this process. The software was supposed to

fulfill three main criteria listed below:

- simulate static dose delivery to static tumors
- TULIP specific parameters should be easily alterable by user input
- should be extendible to dose delivery simulation to moving tumors

#### 4.1.0.1 Input Data

##### Patient specific input data

In order to meet these demands, we implemented a C++ algorithm performing dose calculation on a patient specific CT using spot weight and position data determined by an external IMRT optimization treatment planning system. Therefore, prior to application of the dose calculation algorithm, referred to as *TuDoCa* (TULip DOse CAlculation) in the following, a static treatment plan has to be calculated by a treatment planning system (TPS). For this purpose the DKFZ (*Deutsches Krebsforschungszentrum*) inhouse TPS 'KonRad' was used [Nill et al., 2004]. This step is unavoidable, because for dose calculation with *TuDoCa*, the number of protons delivered by each spot is required as input parameter. These are determined by an iterative optimization process by KonRad (see also 2.4.4). There was no point to include the entire optimization process into *TuDoCa*, since it is mostly independent of the accelerator type, thus not crucial for TULIP specific dose calculation. Machine specific parameters independent from machine movement, that were taken into account, concern the source to axis distance (SAD), energy range and field sizes. These could be modified in KonRad prior to optimization. Since *TuDoCa* performs a dose calculation, the radiological depth of each spot must be determined through a ray-tracing [Siddon, 1985]. For conversion of density values into proton stopping ranges the patient planning CT is needed as input. Additionally, information on tumor and body contours is required to restrict the dose calculation to the relevant regions. Of course, these data are needed also for the optimization by the TPS. Therefore, the volumes of interest (VOIs) were delineated by a clinician prior to dose calculation.

##### Beam specific input data and parameters

Besides the patient specific data, measured or simulated pristine depth dose curves are required to calculate dose. The data used here is equivalent to the data used in KonRad. A measured water depth dose curve for a broad proton beam was used.

The values of the initial  $\sigma_0$ , describing the lateral width of the beam when exiting the accelerator nozzle, have been modified to match the expected TULIP specific nozzle

beam output. Figure 4.1.1 shows the used values for  $\sigma_0$  with increasing energy. Additionally, the corresponding *Full Width Half Maximum* (FWHM) values are shown. These can be calculated from initial values  $\sigma_0$  using the following formula:

$$FWHM = 2\sqrt{2\ln(2)}\sigma_0. \quad (4.1.1)$$

For TULIP specific modeling of the beam penumbra a *Source-to-Axis-Distance* (SAD) of 2.275 m has been implemented within the dose calculation algorithm.

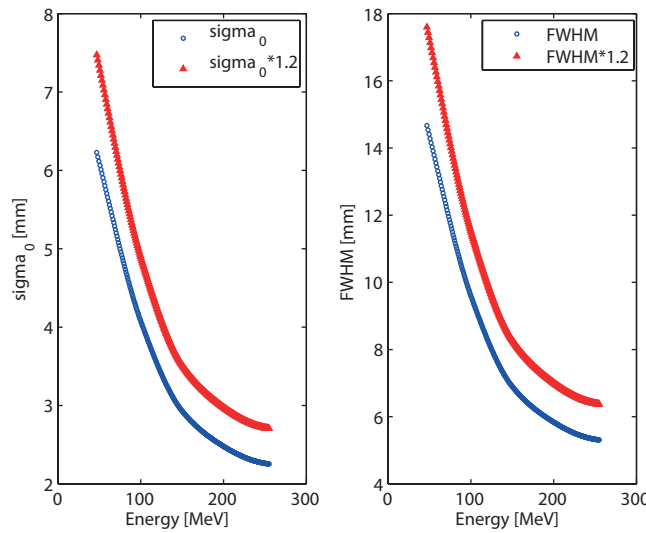


Figure 4.1.1: Left: initial  $\sigma_0$  for increasing proton energies are shown. The blue circles show the original initial  $\sigma_0$ , the red triangles show the same values multiplied with a constant factor of 1.2 which matches better the realistic requirements for TULIP. Right: corresponding FWHMs.

The number of protons that can be delivered within one pulse depends on the cyclotron and its external proton source. For TULIP a 24 MeV Cyclotron by ACSI (Advanced Cyclotron Systems Inc., Canada) with an external proton source is considered and investigated. In this study a maximum number of protons per pulse of  $5 \cdot 10^7$  is assumed. If more particles are needed the original spot is delivered in multiple pulses. Another parameter important for linac design is the breakdown rate (BDR). The very high electric fields on the surface of the accelerating cavities can lead to a so-called breakdown - a localized dissipation of the stored energy in the accelerating structure. This effect has been experimentally studied for TULIP by Degiovanni et al. [2011], Amaldi et al. [2012] and Andres et al. [2012]. For a single-cell cavity operated at 3 GHz the maximum BDR for a maximum electric field of 170 MV/m and RF pulses of 2.5  $\mu$ s was  $3 \cdot 10^{-6}$  bpp/m. According to these results the effect of a broad range of BDRs has been investigated within the dose delivery study presented in this work. For further reading

on breakdown tests for TULIP, the reader is referred to the literature indicated above. In addition to the fixed beam parameters, also beam parameters whose values were to be studied within the scope of this work have been included and can be easily modified by user input. These are the lateral magnet scan speed  $v_{scan,lat}$  and the gantry rotation speed  $v_g$ . Depending on the length of the irradiated volume the TULIP field size of 20 x 20 cm<sup>2</sup> might not be sufficient. In these cases the couch must be shifted with a couch motion velocity  $v_c$  which is assumed to be 1 mm/s. For initial studies also the pulse rate was subject of investigation and has been fixed at a later time point to 120 Hz. Table 4.1.1 summarizes the required patient and beam specific input data.

<b>TuDoCa Input Parameters</b>	
<b>Patient Specific Input</b>	
(4D)CT	
VOIs	
Spots	Energy Position Weight (number of protons)
(ANZAI motion data)	
<b>Beam Specific Input -fixed</b>	
Depth dose curve (water)	Bragg Peak position
HU -rel. stopping power conversion table	lateral beam broadening $\sigma$ Source-to-axis distance SAD
<b>Beam Specific Input - variable</b>	
Number of protons per pulse	$5 \cdot 10^7$
BDR	$10^{-6} - 10^{-3}$ bpp
Lateral scan speed $v_{scan,lat}$	5 - 10 m/s
Gantry rotation speed $v_g$	1 - 6 °/s
Couch motion speed $v_c$	1 mm/s
Pulse rate $f$	$\leq 120$ Hz

Table 4.1.1: Patient and beam specific data and parameters for TuDoCa. Values in brackets are only used for dose delivery simulation to moving targets.

### 4.1.1 TULIP DOse CAIculation software -TuDoCa

The process flow is illustrated in a flow chart in figure 4.1.2. For each fraction the dose delivered by all beams is summed. The basic part of the algorithm, where most of the TULIP specific features are implemented, is the organization of a spot list. Before the spot list is filled with the individual spot characteristics, the time to move the gantry and the couch to the required position is added. Since the important TULIP parameters are the pulse rate and the couch and gantry rotation, the time must be updated throughout the entire delivery process. For filling of the spot list all spots are addressed subsequently and the delivery time ( $t_{delivery} = \frac{1}{f}$ ) is added. There is the option either to rotate the gantry during dose delivery or to use common 3D spot scanning. For rotational delivery, the gantry moves with the user defined gantry speed  $v_g$  during the delivery of the current spot. This simulates a 'semi-continuous' beam delivery during gantry motion. For normal 3D spot scanning the spots are sorted in isoenergy slices (IES). The delivery time is added for each spot. Also, the additional time it takes to move the beam to the next spot position, denoted as  $t_{scan,lat}$ , is added. The lateral scanning time is calculated based on the distance between subsequent spots and the scan speed:  $t_{scan,lat} = \frac{d_{spot}}{v_{scan,lat}}$ .

Once all spots of all beams are added to the spot list, the dose calculation for the dose of one fraction is performed. The dose distributions for all fractions are summed and stored to a final dose distribution.

The dose calculation performed within the algorithm is a pencil beam dose algorithm as described in section 2.4.4 and also used in KonRad. A major difference from the KonRad intrinsic algorithm is the cube on which the dose calculation is performed. Whereas KonRad builds up a new dose calculation grid around the isocenter voxel, which is assumed to be the middle of a voxel, TuDoCa directly uses the CT cube with its original resolution. For validation of TuDoCa, KonRad dose distributions were used. Therefore, it should be emphasized here already, that both dose calculation algorithms are not identical. The different dose calculation cubes used may induce differences in the dose calculation when comparing both dose calculation algorithms.

The dose calculation algorithm described here has been extended to simulate dose delivery to moving tumors. Chapter 5 is devoted to the required software modifications and results for dose delivery to moving targets.

### 4.1.2 Evaluation of the dose calculation software

In order to use the dose algorithm to study TULIP specific dose delivery it must be verified that the dose is calculated correctly. It is obvious that software development and testing involves many steps that cannot be described here entirely. The results presented in the following include a lot of simple dose calculation verification steps such as dose validation for single spots and range checks by direct comparison to

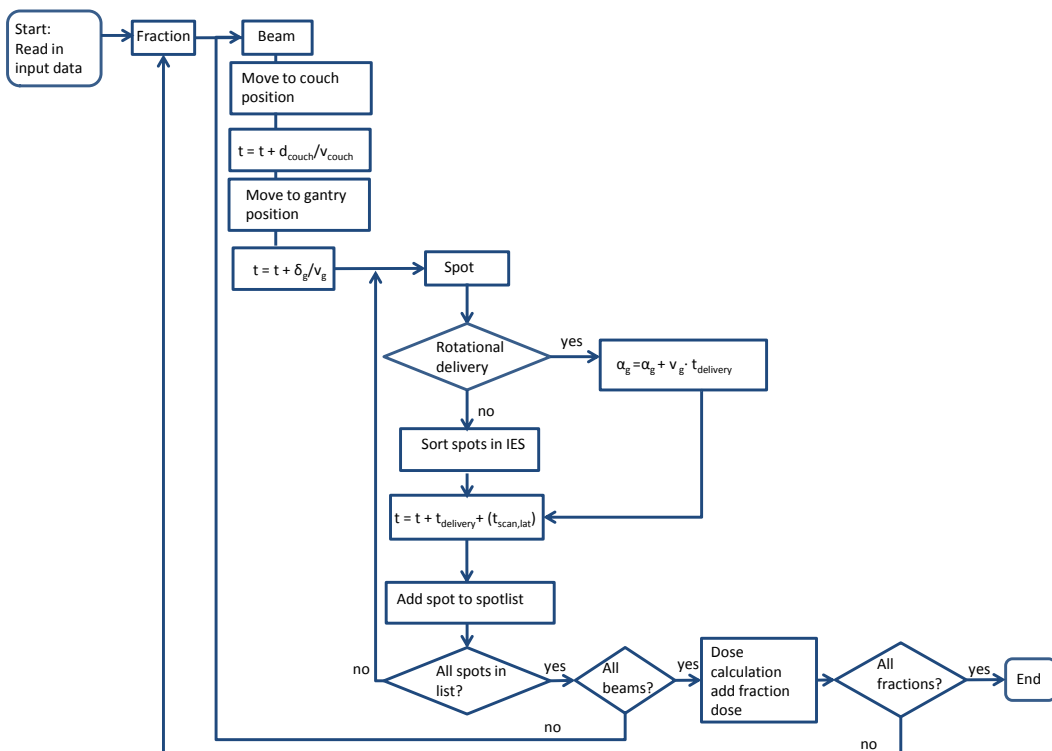


Figure 4.1.2: TuDoCa flow chart. The time dependent dose calculation is shown.  $\delta_g$  indicates the difference between gantry angles for two subsequent beam gantry positions.  $\alpha_g$  indicates the gantry angle difference between two subsequent spots for rotational dose delivery.

analytically calculated dose distributions. After successful performance of these basic evaluation steps, first, the general functionality of the algorithm and the calculated dose for a 3D spot scanning and for rotational dose delivery were evaluated (4.1.2). During code evaluation the relative position of the isocenter within the voxel grid has been exposed as an essential parameter when comparing dose calculations performed by the algorithm presented here and KonRad. Therefore, section 4.1.3 is dedicated to show the influence of the isocenter position relative to the voxel grid on the resulting dose distribution.

#### 4.1.2.1 Methods and Materials

The implementation of the dose calculation algorithm as described in section 4.1.1 has been tested for two principally different dose delivery techniques: 3D spot scanning, which is described in section 2.4.2, and rotational dose delivery. Dynamic rotational dose delivery is not applied in proton therapy up to now. It delivers the dose while the gantry is continuously moving around the patient. The technique has been thought to be applicable for TULIP due to the feasibility of combination of fast dose delivery with a rotating gantry.

In this section, only the translation of the method into software code is evaluated. Influences of this delivery technique on the dose are evaluated in section 4.2.1.

For evaluation, a cylindrical water phantom with a diameter of 17 cm and a length of 9.9 cm was used. The CT grid resolution in x-, y-direction and z-direction was  $\Delta x = \Delta y = \Delta z = 1$  mm, where x gives the extension from right to left of the patient, y points from anterior to posterior of the patient and z gives the longitudinal extension from bottom to top. For dose calculation three volumes of interest (VOIs) have been delineated: a circular target volume which exceeds only over one z-slice, a contour outlining the circumference of the water phantom and the outline contour with an additional 4 mm margins added in all directions. Figure 4.1.3 shows the phantom and the relevant contours. Table 4.1.2 summarizes the parameters for the cylindrical phantom which will be denoted as Phantom1 in the following.

The dosimetric outcome for 3D spot scanning and rotational dose delivery for a static and a moving gantry was calculated. For 3D spot scanning (3DSS) 3 beam directions and, in accordance to the lateral spot size, a lateral spot grid of 3 mm was chosen and spots were set with a 1 mm range difference. The dose prescribed to the target was 60 Gy. First, a static treatment plan was calculated using the treatment planning system (TPS) 'KonRad'. The calculated spot energies, positions and weights were then used as input to the dose calculation algorithm. In case of 3DSS TuDoCa subsequently performed a new dose calculation with static gantry and beam positions as given by the static treatment plan. In case of rotational dose delivery, first a comparison for static gantry positions between KonRad and TuDoCa was performed, since KonRad is not capable to perform dynamic dose calculation. In case of static rotational delivery, a

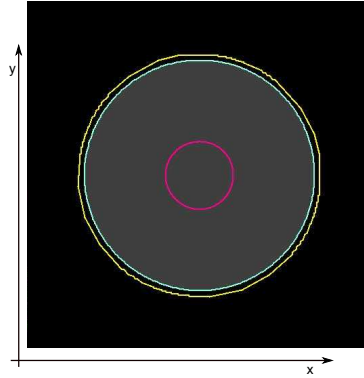


Figure 4.1.3: Transversal view of the CT of the cylindrical water phantom 'Phantom1'. The target is delineated in pink, the outline of the phantom in cyan and the outline with a margin of 4 mm in yellow.

<b>Phantom1</b>	
length [cm]	9.9
diameter (phantom) [cm]	17
diameter (target) [cm]	5
slice distance [mm]	1
CT voxel grid x(y) [mm]	1 (1)
# of target slices	1
total volume [voxels]	9077000
target volume [voxels]	7860

Table 4.1.2: Cylindrical phantom 'Phantom1' CT data

static treatment plan with multiple (110) beam directions was calculated by KonRad and compared to the same plan calculated by TuDoCa. After evaluation of the static dose distribution, the TULIP specific dynamic rotational dose calculation was simulated. In order to do so, the gantry angle position for each beam  $\alpha_{static}$  was used to be shifted for each individual spot according to the current time of dose delivery depending on the gantry rotation speed. The result is an individual gantry angle for each spot  $\alpha_{dyn,spot}$ :

$$\alpha_{dyn,spot} = \alpha_{static} + v_g \cdot t_{delivery}. \quad (4.1.2)$$

The process is visualized in figure 4.1.4.

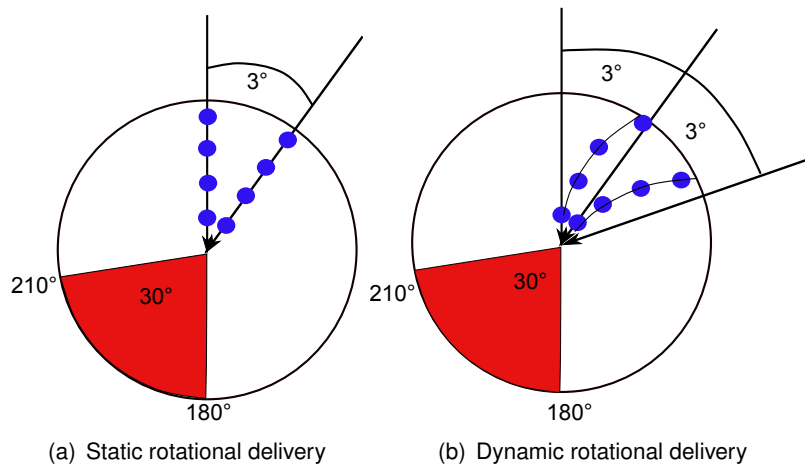


Figure 4.1.4: Rotational dose delivery with TULIP. The static spot positions, shown in (a) are shifted during delivery for dynamic rotational delivery as indicated in (b). The  $3^\circ$  angular step between the static beam positions is marked.

For rotational dose delivery, it must be taken into account that TULIP in its first design version would only be capable to deliver beams from  $0^\circ$  to  $330^\circ$  since the residual  $30^\circ$  are required for static support of the gantry. For dose calculation, the  $330^\circ$  are divided into 110 static beam directions. This was found to be reasonable, since for dynamic rotational delivery, the dynamic gantry positions for each spot could then differ by a maximum of  $3^\circ$  from the statically calculated beam position. Since TuDoCa is using the statically calculated beam energies and beam weights to perform dynamic rotational dose delivery, the gantry positions for static and dynamic dose delivery should not differ too much to avoid density changes and secure validity of the optimized beam weights. Within  $3^\circ$  the differences in density, thus energy and optimized beam weight are small and therefore, the method of shifted static beam positions for dynamic rotational beam delivery is applicable.

The resulting static dose distributions are then compared to KonRad dose distributions using dose volume histograms (DVHs) and differences of dose distributions. Differences to minimal doses received by 1 %, 50 % and 99 % of the target volume and the maximum dose difference between the KonRad dose and the dose calculated by TuDoCa allow for further quantification of the dosimetric differences. The results of the dose algorithm evaluation are presented in section 4.1.2.2.

#### 4.1.2.2 Results

For 3DSS the dose distributions calculated by KonRad and TuDoCa were compared. All results are summarized in table 4.1.3. Apart from dynamic rotational delivery (DR), for all other dose delivery scenarios, the minimum dose values for 99 %, 50 %, 1 % of the target volume deviate less than 1 Gy ( $D_{prescribed} = 60$  Gy) from the reference dose values calculated by KonRad. However, the absolute value of the maximum difference is greater than 14 Gy for all cases. Therefore, in figure 4.1.5 histograms showing the number of voxels that deviate by a certain dose value are shown. For 3DSS the histogram clearly shows that the dose of only a small number of voxels deviates more than 0.5 Gy from the dose calculated by KonRad. The number of voxels increases for static rotational delivery (SR). However, in relation to the total number of voxels of about  $9 \cdot 10^6$  (see table 4.1.2), the fraction of voxels deviating more than 1 Gy is below  $10^{-5}$ . For dynamic rotational delivery we are not expecting the resulting dose distribution to match the static dose distribution calculated by KonRad since the gantry angles for each spot are shifted in that case. The histogram is shown anyway, to illustrate the magnitude of the effect on the dose distribution caused by the continuous gantry rotation.

The deviation of the statically calculated dose distributions are the result of non equal dose calculation cubes used by the two algorithms and by different implementations of dose calculation start voxels. As described above, KonRad builds up a new dose calculation cube around the isocenter. In this case the voxel resolution is the same but the grids are shifted against each other. Additionally, the calculation of the dose calculation start voxel differs. The contour defining the volume in which the dose should be calculated is the same for both algorithms. Due to differing discretization and translation of the data points into voxels, the dose calculation start point may differ by one voxel. Also the allocation of Hounsfield values within a defined contour might differ due to this discretization. Figure 4.1.6 illustrates this effect by means of depth dose profiles for 3DSS. The corresponding dose distributions and the differences between dose distributions are shown in figure 4.1.7. The effect of different start points becomes more obvious if more beam angles are applied as can be observed for static rotational delivery. Therefore, the depth dose curves are shown in figure 4.1.8 and the corresponding dose distributions in figure 4.1.9. For static rotational delivery a ring shaped margin of one or two voxel rows around the contour remains, where the dose calculation algorithms differ due to different discretization of the contours and different calculation

of dose calculation start voxels.

<b>Phantom1</b>							
Delivery method	#beams (static)	$\Delta x$ [mm] ( $\Delta y$ ) [mm]	$v_g$ [ $^\circ/s$ ]	target dose [Gy]			
				$D_{99}$	$D_{50}$	$D_1$	$ D_{diff,max} $
3DSS,KonRad (reference)	3	3 (3)	0	59,3	60,1	60,6	0
3DSS,TuDoCa	3	3 (3)	0	58,6	59,8	60,3	14,8
SR,stat,TuDoCa	110	-	0	58,6	60,0	60,8	18,5
DR,dyn,TuDoCa	110	-	6	56,4	59,9	63,7	17,7

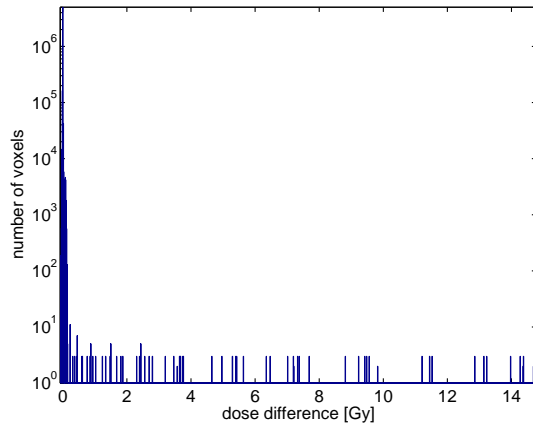
Table 4.1.3: Results: evaluation of dose algorithm TuDoCa. SR refers to static rotational delivery and DR refers to dynamic rotational delivery. 3DSS stands for 3D spot scanning.

#### 4.1.2.3 Discussion

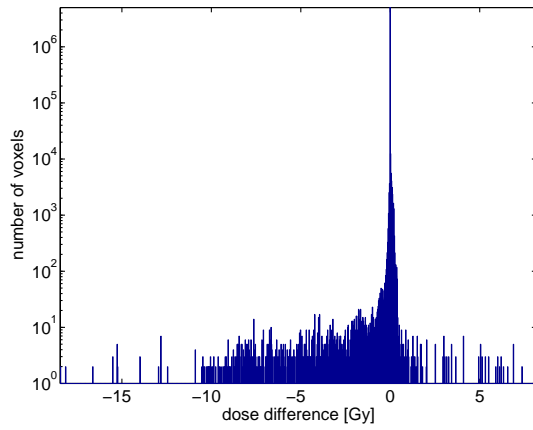
The results of the dose calculation evaluation show deviations of the dose distributions calculated by the treatment planning system KonRad and the dose calculation algorithm TuDoCa in the order of less than 1% for static dose calculations. Considering discretization and numeric effects, agreement of dose values within 1% is an acceptable result. However, a limited number of outliers showing increased dose deviations of up to almost 19 Gy were observed. These can be explained by different dose calculation cube grids and different implementations of the dose calculation start voxel and are no result of wrong implementation of dose calculation in the dose calculation algorithm presented in this work. None of the resulting doses can describe the real applied dose perfectly since both algorithms discretize the volumes of interest for dose calculation and can only represent an approach to what really happens during irradiation. For the purpose of this work, TuDoCa has proven the ability to correctly calculate dose within a predefined volume. The algorithm so far includes the required features as they are: simulation of dose delivery to static tumors and flexible input of TULIP specific beam parameters. Extension to dose delivery to moving tumors is discussed in chapter 5.

#### 4.1.3 Influence of relative isocenter position on the dose distribution

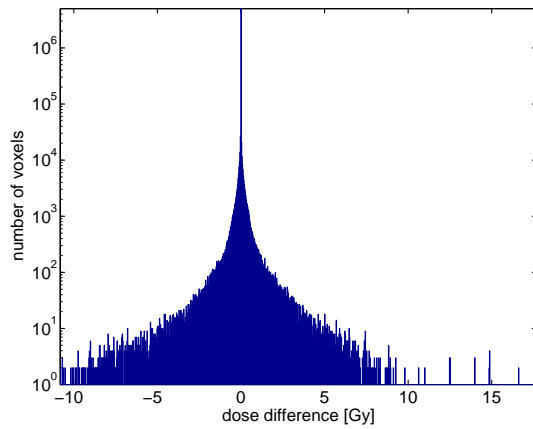
During evaluation of the dose calculation software, we noticed that the resolution of the dose calculation grid and the relative position of the isocenter (IC) within this grid can play a crucial role in proton dose calculation. Due to small shifts of the isocenter even



(a) 3D spot scanning

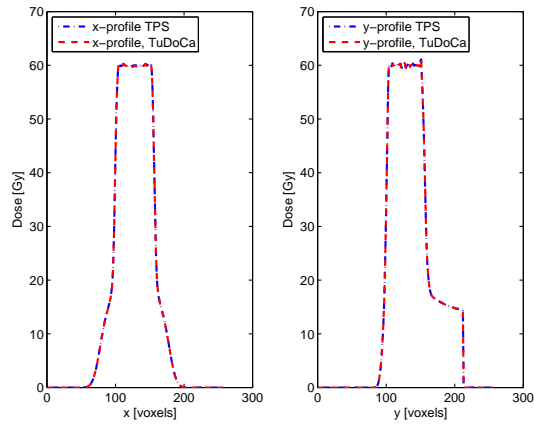


(b) Static rotational delivery

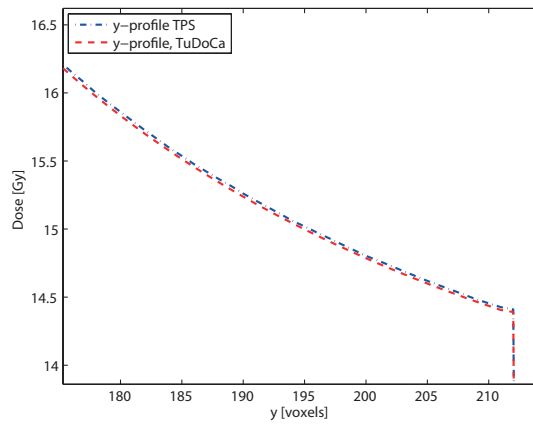


(c) Dynamic rotational delivery

Figure 4.1.5: TuDoCa evaluation: histograms showing the number of voxels that deviate by a certain dose value for 3D spot scanning (a), static rotational delivery (b) and dynamic rotational delivery (c) on a logarithmic scale.



(a) Depth dose profiles for 3DSS.



(b) Magnified detail of the y profile shown in (a). The dose calculation start voxel is identical, but different HU value allocations lead to slightly different dose values for both algorithms.

Figure 4.1.6: Depth dose profiles for 3DSS. In (a) the depth dose profiles along the center of the dose distributions through one slice is shown. (b) shows a magnified detail of the y-profile in (a).

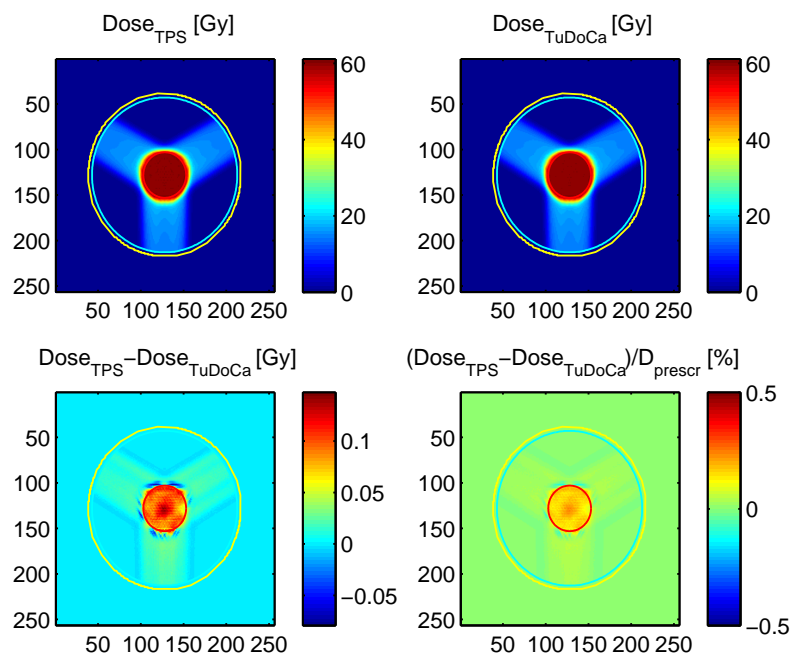
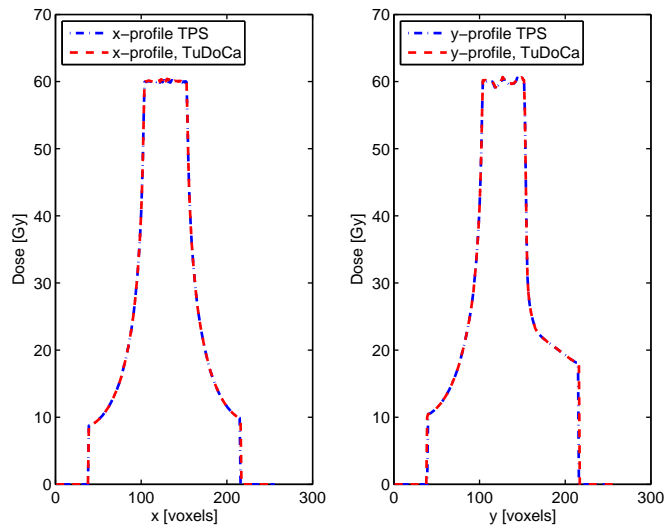
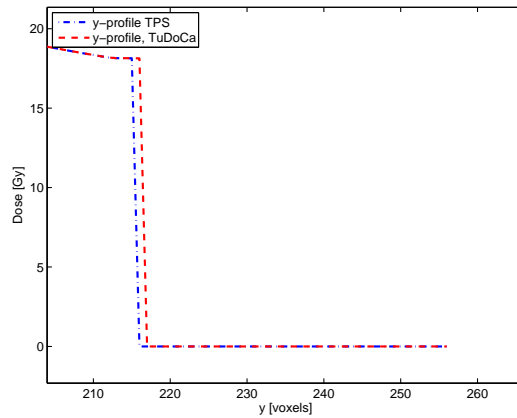


Figure 4.1.7: Transversal slice of the dose distributions for 3DSS and dose differences between KonRad and TuDoCa. Scales in x and y directions are in voxels. Additionally, the contours are shown: target (red), water phantom outline (cyan), water phantom outline plus 4 mm margin (yellow). The lower plots show the differences of dose distributions. For more detailed visualization of dose deviations within the dose calculation volume, values above 1 Gy occurring only at the very border of the outer contour are cut off.



(a) Depth dose profiles for static rotational delivery.



(b) Magnified detail of the y profile shown in (a). The dose calculation start voxel differs leading to slightly different dose values and shift of the depth dose curve.

Figure 4.1.8: Depth dose profiles for static rotational dose delivery. In (a) the depth dose profiles along the center of the dose distributions through one slice is shown. (b) shows a magnified detail of the y-profile in (a).

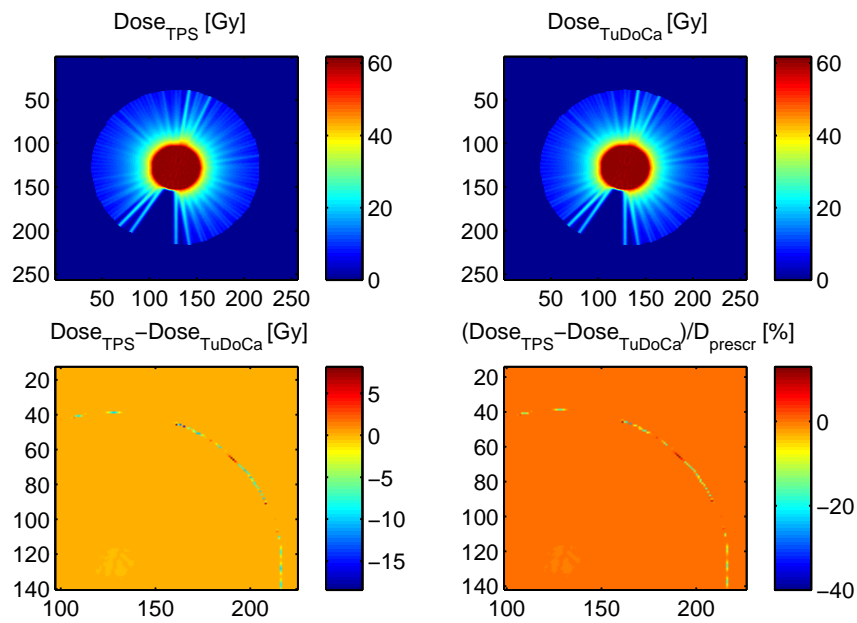


Figure 4.1.9: Transversal slice of the dose distributions for static rotational delivery and dose differences between KonRad and TuDoCa. Scales in x and y directions are in voxels. Additionally, the contours are shown: target (red), water phantom outline (cyan), water phantom outline plus 4 mm margin (yellow). The lower plots show the difference of dose distributions between KonRad and TuDoCa dose distributions. Here, the values were not cut off to show the limited number of voxels that differ by several Gy occurring at the very border of the dose calculation volume.

within one voxel, the dose deviates from the dose calculated with the isocenter at the planning situation. Isocenter shifts, even greater than a few millimeters, are not a TULIP specific problem, but may appear during the course of radiation therapy independent from the delivery technology, i. e. through patient positioning errors between different fractions or even through patient motion within one fraction. Therefore, we tried to gain more insight into patient misalignment caused dose errors during proton therapy and point out how TULIP dose calculation is affected by this effect.

#### **4.1.3.1 Materials and Methods**

When comparing TULIP dose distributions to dose distributions calculated by the treatment planning system KonRad, we noticed that different dose calculation grids have an effect on the dose distributions. The dose calculation volume is subdivided into small volume elements (voxels). Though KonRad uses the original CT as input for the dose calculation, it internally builds up a new dose calculation cube with the isocenter in the middle of the new voxel. The grid resolution remains at a pre-defined fixed value. TuDoCa, in contrast, uses the original CT as input, therefore, the isocenter positions may not always be in the middle of a voxel. In radiotherapy, the CTs used for dose calculation show often the same resolution in x and y direction and a much bigger, thus different resolution in z direction. A cylindrical water phantom of 3.3 cm length and 5 cm diameter with a cylindrical target in the middle is used for the following investigations. The CT grid used here is equidistant with a resolution of 1 mm. Three different delivery methods applicable for TULIP are investigated. These are 3D spot scanning (3DSS), rotational dynamic delivery as described above as well as Distal Edge Tracking (DET) as described in [2.4.2](#), where only a limited number of spots is placed on the target borders. For all techniques, a treatment plan was calculated by KonRad and re-calculated by TuDoCa. In case of dynamic rotational delivery, a dynamic dose calculation was performed as described in section [4.1.2.1](#). The effect of different grid resolutions between KonRad and TuDoCa resulting in different isocenter positions, was modeled by shifting the isocenter and re-calculating the dose. Shifts of 0.4 mm, which is below the voxel size, were simulated. The resulting dose distributions were analyzed by comparison of minimal doses received by 1%, 50% and 99% of the target volume. Additional dose distributions illustrate the effect.

#### **4.1.3.2 Results**

In table [4.1.4](#) the investigated cases for 3DSS, dynamic rotational delivery (DR) and DET are listed.

The most significant results were observed for dynamic rotational delivery. Figure [4.1.10](#) shows the corresponding dose distributions. It clearly shows the shift in the dose distribution caused by the isocenter shift.

## Phantom1

Delivery method	#beams (static)	rel target point [mm]	target dose [Gy]		
			$D_{99}$	$D_{50}$	$D_1$
3DSS	3	(0 0 0)	56.89	59.80	60.02
	3	(0.4 0.4 0.4)	56.73	59.79	60.26
DR	110	(0 0 0)	56.89	59.97	61.64
	110	(0.4 0.4 0.4)	55.81	59.56	64.27
DET	9	(0 0 0)	59.74	60.04	60.28
	9	(0.4 0.4 0.4)	46.10	59.78	60.76

Table 4.1.4: Results: Influence of relative isocenter shift on the dose distribution for three different delivery techniques. The relative target point positions differ by 0.4 mm in all directions.

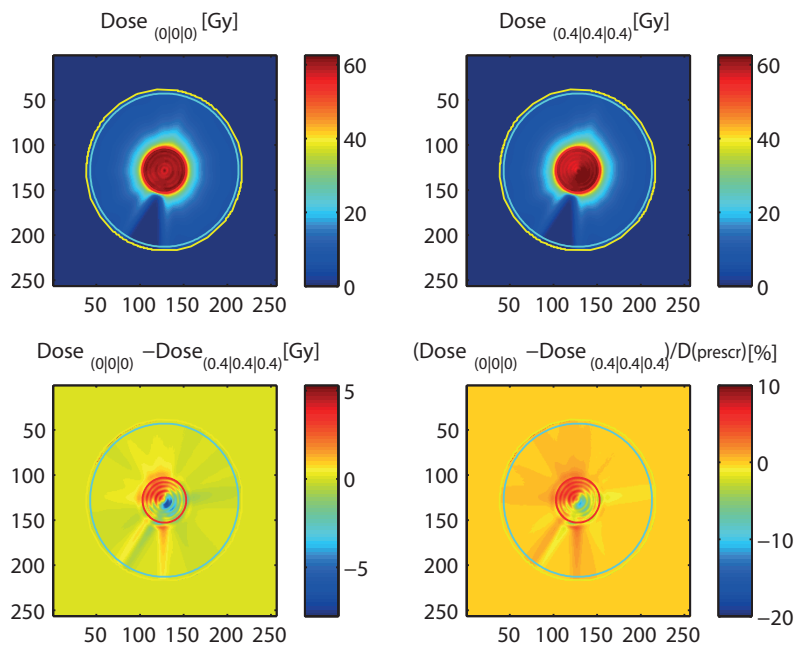


Figure 4.1.10: Transversal slice of the dose distributions for dynamic rotational delivery and dose differences between the dose calculated with the isocenter in the middle of the voxel and shifted by 0.4 mm. X- and y-axis are in voxels. Additionally, the contours are shown: target (red), water phantom outline (cyan), water phantom outline plus 4 mm margin (yellow). The difference of dose distributions clearly shows the effect of the isocenter shift on the transversal slice.

DET has also been found to be very sensitive to isocenter shifts as visible in figure 4.1.11. Since with DET, all spots are placed at the target edges, the dose gradient is the steepest in these regions. The influence of a submillimeter isocenter shift caused dose deviations of up to 8 %.

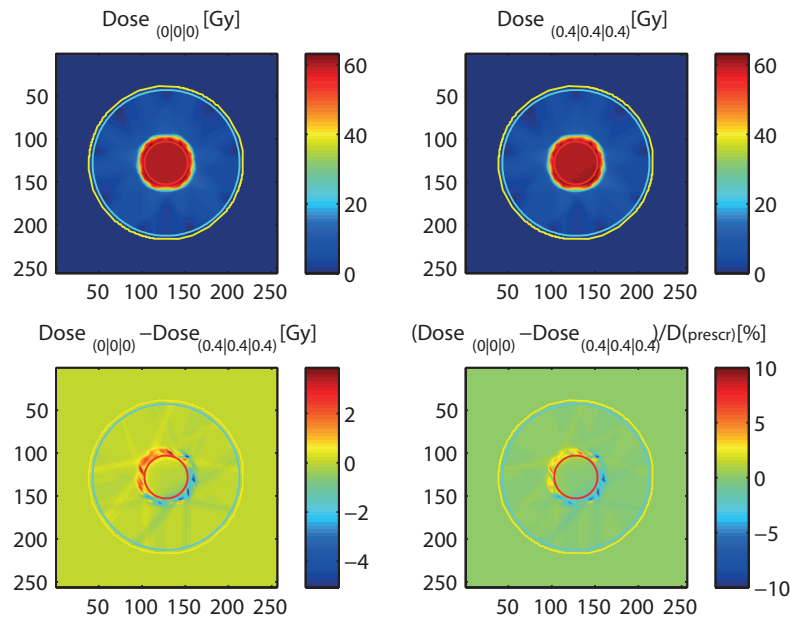


Figure 4.1.11: Transversal slice of the dose distributions for DET and dose differences between the dose calculated with the isocenter in the middle of the voxel and shifted by 0.4 mm. Additionally, the contours are shown: target (red), water phantom outline (cyan), water phantom outline plus 4 mm margin (yellow). The difference of the dose distributions indicates that DET is the most sensitive to isocenter shifts within the steep dose gradients on the target edges.

### 4.1.3.3 Discussion

The results presented in the previous section give an insight into the magnitude of the dosimetric effect of submillimeter isocenter shifts on proton dose calculation. Whereas the effect for 3D spot scanning is rather small, it gets more pronounced for DET and dynamic rotational delivery. Dose differences of several Gy could be observed caused by isocenter shifts of 0.4 mm. The dose differences for DET are mostly due to the steep dose gradient at the target edges. In a real radiation therapy situation, these could be taken into account by the use of safety margins. For dynamic rotational delivery the dose differences can also be noticed within the target volume and could not be

significantly diminished by a margin. Dynamic rotational delivery is very sensitive to small misalignments, since for each proton spot position the dosimetric effect is the same because all spots are placed on one ray with no lateral spots. Also, for opposite beam directions, the effect can be detrimentally enhanced. 3D spot scanning delivers the dose by many spots placed next to each other on a transversal plane. The effect of the isocenter shift might be different for the neighboring spots and therefore might not necessarily be increased by the contribution of each spot.

The results presented here show that tissue misalignment during proton therapy is a crucial issue for proton dose calculation. Therefore, careful patient positioning has to be assured for each therapy session. Nevertheless, protons have the ability to precisely conform the dose to a target, but only if the geometry of patient and beam positioning matches the planning situation.

However, the main purpose of this investigation was not to manifest the potentially harmful effects of setup errors for proton therapy. This has already been extensively studied ([Park et al., 2012], [Park et al., 2013]) and different solutions as incorporation of setup uncertainties in the optimization process ([Fredriksson, 2012],[Casiraghi et al., 2013]) and sophisticated margin concepts [Park et al., 2012] were proposed. Our emphasis was rather put on the study of this effect with particular respect to the dose delivery method and the dose delivery simulation algorithm used in this work and the consequences for the design of TULIP. The dose deviations that were observed within the target cannot be taken into account by safety margins and thus require special attention during planning and irradiation. Concerning the effects on the dose calculation algorithm and its evaluation, we draw the conclusion, that in order to guarantee comparability between dose calculations performed by TuDoCa and the KonRad employed here, the dose calculation grids must match exactly. Otherwise, one cannot distinguish whether potential dose differences are due to mismatch or due to miscalculation within one of the algorithms. Consequently, for further studies, CTs were re-sampled if required to impart matching grids.

## 4.2 Dose delivery to static targets

After successful evaluation of the dose calculation algorithm TuDoCa, TULIP specific dose delivery was studied in order to find the most effective dose delivery procedure. In this chapter the dose delivery to static tumors is studied. The subsequent chapter 5 is dedicated to dose delivery to moving tumors. Part of this dose delivery studies was to find the optimal dose delivery for a suitable design of TULIP. Therefore, in the following, two different designs of TULIP are studied regarding dose delivery. First, the initial design of TULIP, allowing for rotational dose delivery was studied (4.2.1). Subsequently, 3D spot scanning dose delivery with TULIP is investigated in section 4.2.2.

### 4.2.1 Dynamic rotational dose delivery

In rotational therapy the radiation source moves around the patient. For photon therapy, this concept has already been put into practice through several techniques. In helical tomotherapy [Mackie et al., 1993] a rotating fan beam delivers the dose to the patient who is moved through the gantry bore. Also the idea to perform arc therapy with conventional photon linear accelerators was proposed long ago [Takahashi et al., 1983]. In Intensity Modulated Arc Therapy (IMAT) the dose is delivered from multiple superimposed arcs. The field shape is modulated through the Multi Leaf Collimator (MLC) of the accelerator but the dose rate is constant. The first commercialized single arc therapy system was RapidArc<sup>TM</sup> by Varian [Varian medical systems, 2008]. Other techniques such as Volumetric Modulated Arc Therapy (VMAT) commercialized by Elekta AB allow also for variation of the dose rate with the purpose of reduction of irradiation time. These techniques are commercialized by several vendors nowadays and are already widely used for cancer treatment. These rotational delivery methods offer the possibility of fast and highly conformal dose delivery. There have been attempts to deliver proton dose distributions from multiple static beam positions ([Flynn et al., 2007], [Rechner et al., 2012]), but so far, no dynamic rotational dose delivery system is applied in clinical use. However, with the invention of new accelerator techniques for protons, proton rotational delivery came into the focus of research. Caporaso et al. [2008] proposed rotational dose delivery performed with a dielectric wall accelerator as described in section 2.3. Physical requirements for proton arc therapy have further been investigated by Sengbusch et al. [2009]. Also, for TULIP, rotational delivery represents one option of dose delivery since the accelerator is mounted on a gantry providing a pulsed beam on a milliseconds time scale. In this first section, we deal with rotational proton dose delivery performed by TULIP as shown in picture 3.1(c). The accelerator is mounted on a gantry which can rotate around the patient by  $330^\circ$  with a rotation speed in the range of 1 rpm to 1.5 rpm. A sector of  $30^\circ$  cannot be used as incoming beam directions since the gantry needs to be statically supported. Dose is delivered by a pulsed beam with a repetition rate of maximum 120 Hz. With these parameters TULIP provides the possibility to perform fast rotational dose delivery. Additionally, two scanning magnets are installed in the accelerator nozzle that allow for transversal movement of the beam covering an area of  $20 \times 20 \text{ cm}^2$ , thus enabling 3D spot scanning. In the following we investigate rotational proton therapy for TULIP with respect to feasibility, dosimetric outcome and irradiation time and compare the results to 3D spot scanning, also performed with TULIP. The purpose is to find the optimal dose delivery procedure for TULIP and to suggest potential modifications of the device according to these findings.

#### 4.2.1.1 Materials and Methods

Rotational dynamic delivery was modeled within the dose calculation algorithm TuDoCa as described in section 4.1.2.1. First, a static treatment plan had to be calculated by a treatment planning system (KonRad) in order to get the spot weights and the static spot positions and energies. A set of 110 initial beam directions covering  $330^\circ$  for calculation of the static treatment plan has been found to be reasonable for the following dynamic dose calculation with TuDoCa. As illustrated in figure 4.1.4 the static beam angles are shifted for each spot due to the gantry motion during dose delivery. By dividing the total of  $330^\circ$  into 110 subsections, each section covers an angle  $\alpha = 3^\circ$ . By assuming the shape of a realistic tumor to be approached by a sphere of radius 10 cm the length of the circle section is  $L = 2\pi r \cdot \frac{\alpha}{360^\circ} \approx 0.5$  cm. Since the minimum CT pixel size used for this study is 1 mm, density changes within this section are assumed to be minor. This is important, since the original beam energies calculated for the static delivery based on the CT are used for dynamic rotational dose delivery. For density changes within the beam's path, the energies would change to avoid over- or undershoot of the target. Also, for dynamic rotational delivery (DR), the maximum angle to be covered by the spots of one static beam is limited to the beam section of  $3^\circ$ . If the gantry moves faster, so that not all of the spots planned for this section can be delivered within the time the gantry would move along that angular step, the gantry is stopped for the delivery of the residual spots of that beam. For comparison, also the dose delivery with a continuously moving gantry - without stopping after a certain angle section - has been simulated and is denoted as CDR.

Throughout the entire delivery process the time is updated. Additionally to the spot delivery time of  $\frac{1}{120}$  s and the time to change the magnet current of 100 ms is taken into account. The momentum acceptance of the scanning magnets is assumed to be approximately  $\pm 2\%$  which converts to a range acceptance of  $\pm 7\%$  due to equation 2.1.3. This means that the magnet current has to be adjusted if the range difference of neighboring spots exceeds  $\pm 7\%$ . The 100 ms needed to change the current are added whenever the critical range difference is exceeded.

In order to cover targets exceeding the longitudinal size of the scanning field of 20 cm, multiple isocenter positions would be calculated and the couch would be moved to the next isocenter position. In this case the spots for one isocenter position and for all longitudinal positions and the same energy are delivered first, then the energy is changed. Again all of these spots are delivered within  $3^\circ$  of gantry rotation.

For 3D spot scanning the static treatment plan is re-calculated while the time is tracked throughout the delivery process to compare irradiation times for the two delivery methods. The delivery time for each spot is the same as for rotational delivery based on the pulse rate of the linac. For moving the gantry to the next beam positions the same gantry rotation speed as for rotational dose delivery is assumed.

Dose delivery studies were based on a water phantom geometry and on a lung

patient case, considering the tumor to be static for the purpose of this investigation. The phantom used is a cylindrical water phantom with a cylindrical target of 5 cm diameter in the middle. The outline of the phantom is delineated as well as an additional 5 mm margin in all directions around the outlined volume. All relevant parameters are given in table 4.2.1. The patient case is a lung tumor patient which in this case is not a realistic patient case since usually the lung and with it the tumor would move. For the purpose of this study, tumor motion does not play a role, since we are only interested in realistic organ and tumor volumes and densities. Therefore, we calculated a treatment plan for the PTV which is assumed to be static. The patient specific parameters can be found in table 4.2.1.

<b>Cylindrical phantom</b>	
CT slice distance [mm]	1
CT voxel grid x(y) [mm]	1 (1)
# of target slices	32
total volume [voxels] ([cm <sup>3</sup> ])	9077000 (2269.25)
target volume [voxels] ([cm <sup>3</sup> ])	235260 (58.815)
<b>Patient lung A</b>	
CT slice distance [mm]	0.98
CT voxel grid x(y) [mm]	0.98 (0.98)
total volume [voxels] ([cm <sup>3</sup> ])	30677263 (28553,8)
target volume [voxels] ([cm <sup>3</sup> ])	11860 (11.04)

Table 4.2.1: CT data for cylindrical phantom and lung patient A

For both, phantom and patient, a dose distribution is calculated for dynamic rotational delivery and for 3D spot scanning (3D), meaning that a field is scanned from a fixed gantry position, and the results are compared. To illustrate the effect of a continuously moving gantry during dose delivery, first, the gantry speed and the repetition rate was varied for dose calculation for the phantom. Within the machine limitations, the optimal set of parameters should be found. Therefore, several combinations of parameters covering the realistic machine ranges have been chosen to perform dose calculations and systematically evaluate the effect of each parameter. A summary of the parameter combinations applied is given in table 4.2.2.

#### 4.2.1.2 Results

Rotational dynamic delivery to a cylindrical water phantom was simulated by shifting static gantry positions according to the corresponding gantry speed. In figure 4.2.1

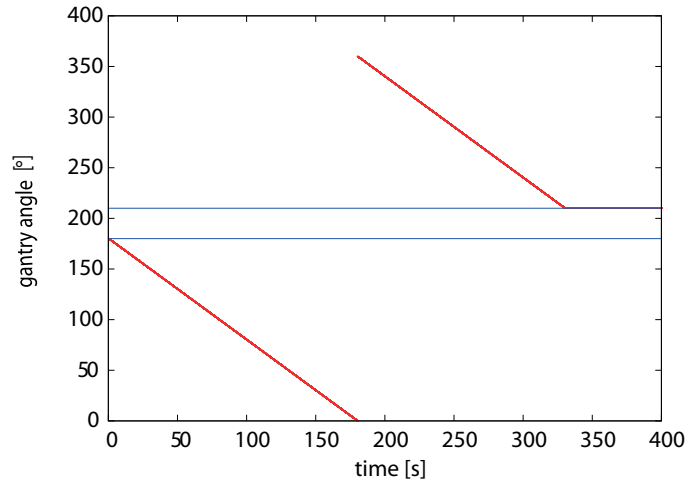
Phantom/ Patient	delivery method	$D_{prescr}$ [Gy]	# of static beam angles	$v_g$ [°/s]	$f$ [Hz]
$P_{Cyl}$	CDR	60	110	1	120
$P_{Cyl}$	CDR	60	110	3	120
$P_{Cyl}$	CDR	60	110	6	120
$P_{Cyl}$	DR	60	110	1	variable
$P_{Cyl}$	3DSS	60	3	1	120
Pat A	CDR	60	110	1	120
Pat A	DR	60	110	1	120
Pat A	DR	60	110	1	variable
Pat A	3DSS	60	3	1	120

Table 4.2.2: Parameter combinations for dynamic and static dose delivery with TULIP. Two cases are studied: a cylindrical water phantom  $P_{Cyl}$  and a lung patient Pat A. Continuous dynamic rotational delivery is denoted as CDR. When the gantry is stopped after an angular step of  $3^\circ$  the delivery is denoted as DR. 3DSS refers to 3D spot scanning.

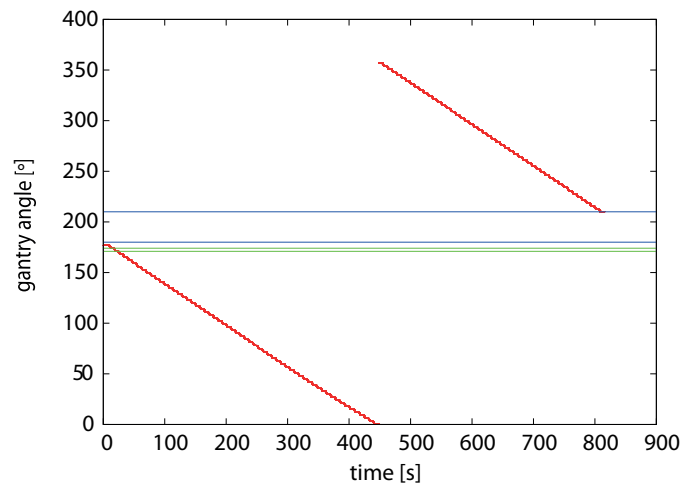
the gantry angles for individual spots are plotted with respect to time. The figure visualizes the difference between continuous rotational dose delivery and dose delivery with gantry stops at the fixed beam positions. If the gantry motion would exceed the user defined maximum  $3^\circ$  angle spacing between static beam positions the gantry is stopped for the delivery of the residual spots. Also, the section between  $180^\circ$  and  $210^\circ$  is marked. This part cannot be reached by the gantry head since the static support is located there.

In table 4.2.3 the dosimetric results for the water phantom as well as for the lung patient case are summarized. To quantify the effects of the delivery method and parameters on the dose, minimal doses to 95, 50 and 5 % of the target volume are given. Since the delivery time, the time to change the magnet current for larger energy variations and total irradiation time as well as lateral scan time for 3DSS are of interest for comparison of the two delivery methods, these are also presented in table 4.2.4.

The table clearly shows the influence of continuous gantry motion during dose delivery. For all investigated combinations of dynamic parameters, the minimal dose to 50 % of the target volume deviates heavily from the prescribed dose of 60 Gy for the water phantom. For a gantry rotation speed of  $3^\circ/s$   $D_{50}$  deviates by over 82 % from the prescribed dose. Dose deviations of the minimal dose received by 5 % of the target volume deviate enormously from the prescribed dose. Additionally, the gantry reaches its maximum position at  $210^\circ$  long before all spots are delivered. Therefore, the residual spots are delivered from the same maximum gantry position. Both effects are consequences



(a)



(b)

Figure 4.2.1: Gantry positions for dynamic rotational dose delivery with TULIP. In (a) gantry positions in the course of continuous rotational dose delivery are shown in red. (b) shows the gantry positions if the gantry is stopped if the range of  $3^\circ$  is exceeded. Small angular steps can be noticed in (b). Additionally, the blue lines the angle segment which cannot be reached by the gantry. The green lines indicate an arbitrary  $3^\circ$  segment.

	DM	Dynamic parameters			Dose <sub>target</sub>		
		$v_g$ [°/s]	$f$ [Hz]	$t_{mag}$ [s]	$D_{95}$ [Gy]	$D_{50}$ [Gy]	$D_5$ [Gy]
$P_{Cyl}$	CDR	1	120	0.1	22.7	28.1	230.8
$P_{Cyl}$	CDR	3	120	0.1	1.4	10.5	331.7
$P_{Cyl}$	CDR	6	120	0.1	6.8	14.0	309.8
$P_{Cyl}$	DR	1	120	0.1	57.9	60.0	61.7
$P_{Cyl}$	DR	1	var	0.1	58.6	59.8	60.9
$P_{Cyl}$	3DSS	1	120	0.1	58.5	59.9	60.1
Pat A	CDR	1	120	0.1	21.0	58.0	115.9
Pat A	DR	1	120	0.1	42.9	53.3	60.3
Pat A	DR	1	var	0.1	32.1	53.2	74.2
Pat A	3DSS	1	120	0.1	58.8	59.8	60.5

Table 4.2.3: Dosimetric results for rotational dynamic and 3D spot scanning dose delivery with TULIP. For different delivery methods (DM) and dynamic parameters, dose values for a cylindrical water phantom  $P_{Cyl}$  and a lung patient Pat A are given.

	DM	Dynamic parameters			Time			
		$v_g$ [°/s]	$f$ [Hz]	$t_{mag}$ [s]	$t_{total}$ [s]	$t_{delivery}$ [s]	$t_{mag}$ [s]	$t_{scan}$ [s]
$P_{Cyl}$	CDR	1	120	0.1	814.6	716.1	97.6	0
$P_{Cyl}$	CDR	3	120	0.1	814.6	716.1	97.6	0
$P_{Cyl}$	CDR	6	120	0.1	814.6	716.1	97.6	0
$P_{Cyl}$	DR	1	120	0.1	1638.2	716.1	97.6	0
$P_{Cyl}$	DR	1	var	0.1	427.6	330	97.6	0
$P_{Cyl}$	3DSS	1	120	0.1	555.7	308.5	0.9	4.4
Pat A	CDR	1	120	0.1	312.3	179.8	112.6	0
Pat A	DR	1	120	0.1	2100	179.8	112.6	0
Pat A	DR	1	var	0.1	1219.6	990	112.6	0
Pat A	3DSS	1	120	0.1	349.7	57.3	0.9	0.02

Table 4.2.4: Results with regard to time for rotational dynamic and 3D spot scanning dose delivery with TULIP. For different delivery methods (DM) and dynamic parameters, dose values for a cylindrical water phantom  $P_{Cyl}$  and a lung patient Pat A are given.

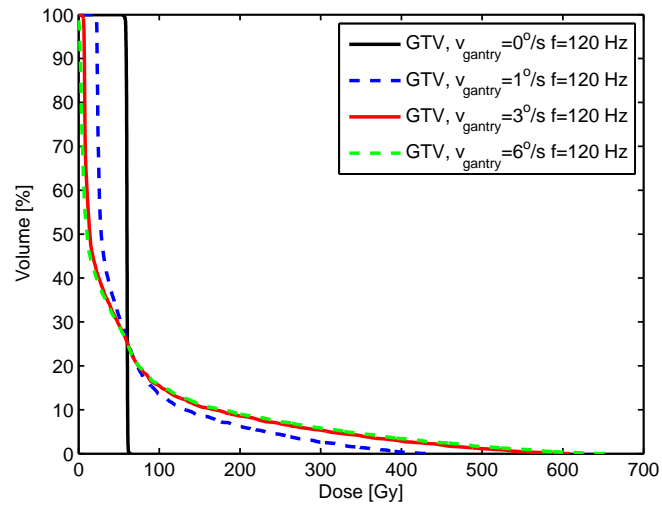
of a too fast gantry rotation so that too many spots cannot be delivered close to their static position. An example of dynamic rotational delivery for the three gantry speeds without stopping the gantry during delivery is shown in figure 4.2.2. For comparison, dvhs for dose delivery with gantry stops after each  $3^\circ$  if required are shown in 4.2.2. Of course, for real application, this must be avoided by a beam control system. However, this would only avoid the huge overdosage at the final beam angle. For demonstration of all effects happening during dynamic rotational irradiation without modifications this data is shown.

As stated above, for continuous gantry rotation, the number of spots to be delivered exceeds the number of spots that can be delivered during the time the gantry moves along the  $3^\circ$  segment. Thus three possibilities to avoid spots being delivered far away from their statically calculated position can be thought of. First, a reduction of the number of spots, second, a decrease of the gantry speed, and third, an increase of the repetition rate. Theoretically, the number spots  $n_{\Delta\alpha}$  that can be delivered for a given gantry speed  $v_g$  and a fixed repetition rate  $f$  within an angle segment  $\Delta\alpha$  can be derived as follows:

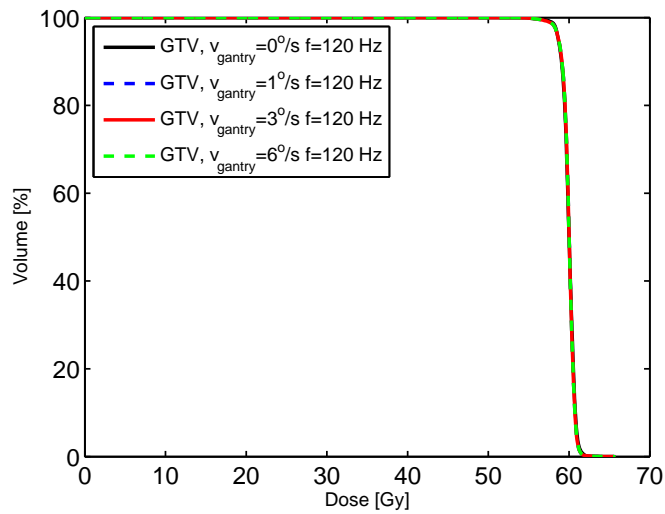
$$n_{\Delta\alpha} = \frac{\frac{\Delta\alpha}{v_g}}{t_{delivery}} \quad (4.2.1)$$

with  $t_{delivery} = \frac{1}{f}$ .

For  $\Delta\alpha = 3^\circ$ ,  $f = 120$  Hz and  $v_g = 1^\circ/\text{s}$ , the maximum number of spots that can be delivered during this section is 360. For the investigated phantom and treatment plan, the mean number of spots per beam is 781 and the maximum number is 969 for each static beam direction. These numbers can be reduced by decreasing the longitudinal spot grid. However, the dose would lose its uniformity. Alternatively, the gantry speed must be decreased to  $0.37^\circ/\text{s}$  to ensure delivery of all spots with the given angular step of  $3^\circ$ . For a full rotation ( $330^\circ$ ) this corresponds to a very slow gantry motion of 0.06 rpm (rounds per minute), which would lengthen the irradiation time and could approach the technically feasible limitations of continuous gantry motion. The last possibility to decrease the delivery time can be realized by increasing the pulse rate. Dose delivery without a fixed limitation for the pulse rate has been simulated. In this case, the pulse rate is varied for each beam according to the number of spots within a certain angular step. The spots should be optimally spread within the angular step, defined by the original static treatment plan. This segment should be covered by the gantry moving with a dedicated gantry speed until the next original gantry position is met. The pulse rate  $f$  for a number of beams for one static gantry position  $n_{beam}$  to be delivered while the gantry moves with  $v_g$  along the angle segment  $\Delta\alpha$  can be determined as follows:



(a) Dvhs for rotational dynamic dose delivery without a fixed angular step



(b) Dvhs for rotational dynamic dose delivery with a fixed angular step

Figure 4.2.2: Dvhs for rotational dynamic dose delivery with (a) and without (b) a fixed angular step. The unwanted distortion of the dose due to rotation of the gantry becomes obvious in (a).

$$f = n_{beam} \cdot \frac{v_g}{\Delta\alpha} \quad (4.2.2)$$

Comparing the results for continuous rotation (CDR) to rotation with potential gantry stops during dose delivery (DR) with a variable pulse rate, clearly improved dose values are observed for the phantom. This is not the case for the patient. This confirms that the pulse rate is only optimized to spread the number of spots of one original beam direction within a dedicated angle segment covered by the gantry within the corresponding time. The striking difference between the phantom and patient case is, that for the patient, the mean repetition rate per beam is smaller than 120 Hz used for simulating dose delivery with a fixed pulse rate, while for the phantom case it is the other way around. Always the dose delivery with a fixed pulse rate results in a higher homogeneity of dose. Figure 4.2.3 visualizes the pulse rates for static and variable pulse rate for the patient case and for comparison also for the water phantom.

For the patient case three isocenter positions are used to cover the entire target volume in cranio-caudal direction. Therefore, the number of beams is 330 in total, since 3 rotations with 110 static beam positions per rotation are performed. The dosimetric results also manifest in the total irradiation time. When the gantry is stopped until all spots for one static beam position are delivered, this time is added and results in an increased overall irradiation time compared to continuous rotational delivery. For variable pulse rate delivery the total time is minimal since the delivery time depends only on the time the gantry needs to rotate along the 3° angle and no gantry motion pauses must be added.

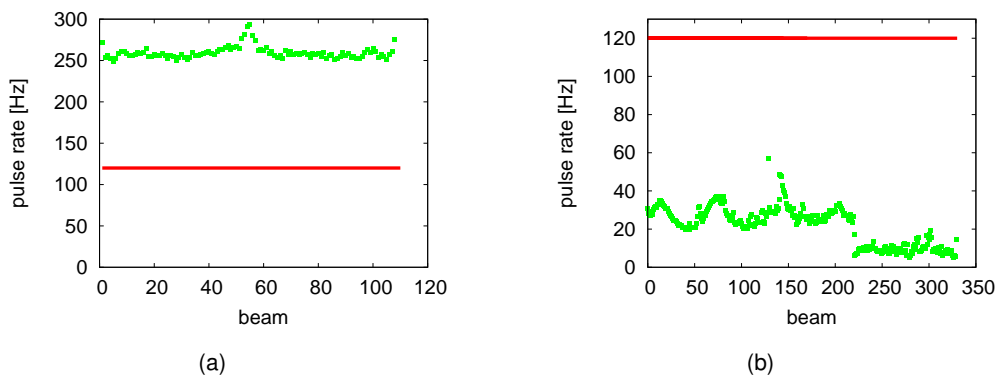


Figure 4.2.3: Pulse rate for each beam for fixed (120 Hz) (red line) and variable pulse rate (green points) for the cylindrical phantom (a) and lung patient Pat A (b).

The results for 3D spot scanning (3DSS) are stinkingly better than the ones obtained with rotational dose delivery (DR) for a fixed pulse rate: the minimal doses to 95, 50 and

5 % deviate less than 2.5 % from the prescribed dose for the water phantom. For Pat A even the optimized repetition rate does not improve the dose distribution compared to CDR. This is due to the fact, that in this case, the repetition rate is generally decreased to optimally spread the spots within the static angle segment (see figure 4.2.3). In this case the spots therefore deviate more from their original position than for using a fixed but higher (120 Hz) pulse rate. The total irradiation time is less than 6 minutes for the lung patient.

Even though it is feasible with an optimized set of dynamic parameters to achieve an acceptable dose distribution with dynamic rotational dose delivery, the dose distribution for 3D spot scanning is favorable with respect to dose to normal tissue. Figure 4.2.4 clearly shows the difference in dose for a transversal slice of Pat A for rotational and 3D spot scanning delivery. Corresponding dose profiles are shown in figure 4.2.5. Due to multiple spread beam directions, the dose to normal tissue is increased for rotational dose delivery.

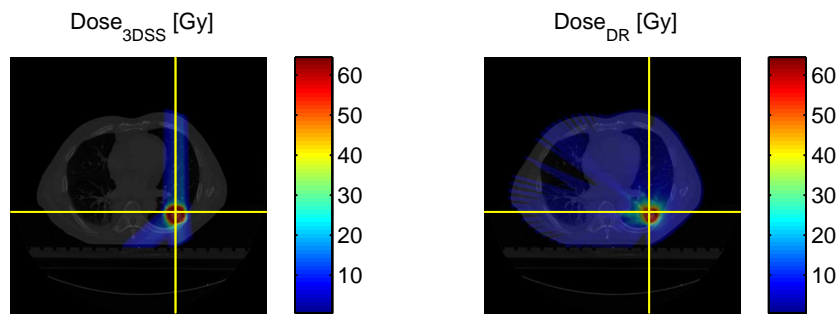


Figure 4.2.4: Comparison of dose distributions for 3D spot scanning and dynamic rotational delivery. Rotational delivery results in a detrimental dose bath to normal tissue.

#### 4.2.1.3 Discussion

The results presented in the previous section illustrate the challenges of dynamic rotational dose delivery for protons with TULIP. For a cylindrical water phantom and a lung patient it has been shown that rotational dose delivery with a continuously rotating gantry leads to severe dose distortions when the time influencing parameters are not carefully adjusted. We have depicted the optimal timing parameters that would result in acceptable dose distributions. To minimize the time to be spent for spot delivery during gantry rotation, the number of spots could be reduced. However, this was not pursued within this work, since it is only a feasible approach for limited cases and could harm the steepness of dose gradients. The second approach investigated here, is the decrease of gantry speed. The suitable gantry speed to deliver the spots without large deviations

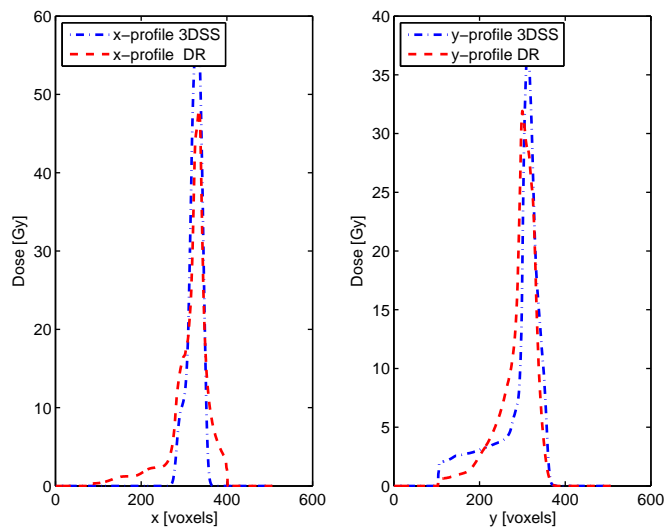


Figure 4.2.5: Dose profiles for 3D spot scanning (blue, dashed dotted line) and rotational delivery (red, dashed). The profiles are drawn along the yellow lines indicated in figure 4.2.4. In the entrance channels both methods apply dose to normal tissue. Dynamic rotational delivery (DR) delivers an increased dose to surrounding tissue due to multiple incoming beams.

from their static positions has been calculated for the water phantom. However, the resulting value of 0.06 rpm is below the limit of what is technically feasible for TULIP, since the TULIP gantry is supposed to rotate with a minimum speed of 1 rpm due to statics. Thirdly, the pulse rate was adjusted to match the number of spots to be delivered within the time the gantry moves along a small angular step. This also was shown to be strongly dependent on the individual number of spots per static beam direction. In the investigated cases, a repetition rate of 120 Hz which is technically feasible would suffice for rotational delivery to a lung tumor. For the water phantom, the required repetition rate was far beyond that limit. Consequently, a method was developed with gantry stops for each angular step defined by the original incoming beam directions until all spots belonging to that beam are delivered. This leads to acceptable dose distributions, however, this would mean that the gantry has to be decelerated and accelerated multiple times during one rotation, which is technically challenging due to the size and weight of the gantry which has to be moved and could harm the gantry joints.

Of course, some of the challenges and drawbacks listed above are somehow consequences of the dose delivery simulation method. Certainly, an adequate composition of dynamic parameters must be found to assure the delivery of a sufficient number of spots to the target volume while simultaneously avoiding overlaps. While this is still a challenging task, the problem of too large deviations of spots from their static positions

leading to dose deviations is related to the delivery method, which uses the same spots and their weights as calculated for the static delivery. Thus, a time dependent optimization, taking the current spot positions into account, could reduce the dose distortions.

The more generally valid criterion against dynamic rotational dose delivery is the increased dose outside the target. Comparing the results for dynamic rotational dose delivery and 3D spot scanning with regard to dose and time, there seems to be no reason for application of rotational dose delivery for protons with TULIP. Gantry rotation during dose delivery resulted in an unwanted and unnecessary dose bath to normal tissue around the target. The physical advantages of protons thereby are impaired and could be better exploited with 3D spot scanning. The dose delivered to normal tissue is small, but it is spread almost over the entire target surrounding tissue. Even though the dose within each entrance channel for dose delivery with 3DSS using 1 - 5 beams is increased compared to the dose bath for rotational dose delivery, it can be precisely controlled where this dose is deposited. Thereby, critical organs can be spared better by clever patient and beam positioning. Altogether, 3D spot scanning resulted in beneficial dose distributions and reduced delivery times for almost all cases. Dose delivery with TULIP for a realistic tumor was shown to be feasible within less than 6 minutes for a repetition rate of 120 Hz. With higher gantry speeds this time would further decrease.

Altogether, this study led to the decision to not pursue rotational delivery with this design of TULIP any further. If no rotational dose delivery is required, the maximum rotation angle could be reduced to  $\pm 110^\circ$  for the new design leading to a smaller footprint of TULIP while, in combination with the robotic couch, still allowing for all incoming beam angles (0-360°). In the following section the results for 3D spot scanning with TULIP are presented for several patient cases with different tumor indications.

## **4.2.2 3D spot scanning dose delivery with TULIP**

In this section, 3D spot scanning dose delivery is studied with respect to dose and time for technically feasible and TULIP specific parameters. The purpose is to ascertain whether TULIP dose delivery can be applied to and is suited for diverse realistic tumor cases.

### **4.2.2.1 Materials and Methods**

For three different patient cases, 3D spot scanning delivery with TULIP was simulated using the dose delivery simulation software 'TuDoCa' described in section 4.1.1. Patient cases were chosen to be different from each other with respect to tumor position and size as well as organs at risks (OARs) to cover the large spectrum of potential tumors to be irradiated with TULIP. We investigated a patient with a spine sarcoma, where the spinal cord is within the target volume and other organs as the esophagus and trachea are in direct vicinity. The patient received primary radiation therapy since tumor resec-

tion was impossible. Secondly, a patient with a medulloblastoma was treated, where diffuse spread in many organs through the cerebrospinal fluid is a major concern. This patient was chosen since the target volume is extremely large and a time consuming craniospinal irradiation (CSI) is performed. Therefore, several couch positions are mandatory to shift the patient longitudinally within the treatment field. Within the dose calculation algorithm this was modeled by several isocenter positions and TULIP specific lateral field extensions of 20 cm. Thirdly, a prostate tumor patient was chosen since this is a very common and frequently occurring tumor in men. Organs that are prone to suffer from radiotherapy treatment of the prostate are the rectum and the bladder. Table 4.2.5 summarizes the input data for the investigated patients. Beam angles are given in the coordinate system defined by the International Electrotechnical Commission (IEC) standard 61217 [IEC standard]. These can be converted to TULIP specific beam angles and can be realized in practice by couch rotation.

For a better view, transversal, frontal or sagittal views of the CT scans with the most important organ structures delineated are shown in figure 4.2.6

For 3D spot scanning (3DSS), again, the same simulation approach was used as in the previous section 4.2.1. Basically, for 3DSS the algorithm re-calculates the dose derived by KonRad with TULIP specific parameters since no beam motion during dose delivery takes place. However, for calculation of irradiation time, the TULIP time influencing parameters are considered. These are listed in table 4.2.6. The static dose was planned to match or improve the dosimetric planning results for a photon tomotherapy treatment.

For each of the patients listed in table 4.2.5 a 3DSS dose calculation with the parameters indicated in table 4.2.6 was performed using the dose delivery and calculation software TuDoCa.

#### 4.2.2.2 Results

In consideration of the rather complicated cases with respect to positions of organs at risk (OARs) in very close vicinity of the target, 3DSS resulted in clinically acceptable dose distributions for the target volumes as well as in relatively low doses to the organs at risk. The dosimetric outcome as well as the irradiation times are given in table 4.2.7. Dose volume histograms visualize the results for the target volumes and selected oars.

For irradiation of the spine sarcoma, which is clinically required to receive a dose above 66 Gy, the prescribed dose of 70 Gy to the PTV is compromised due to the spinal cord as an organ at risk included within the target volume. The volume of the spinal cord receiving 40 Gy, which in total should not receive more than 50 Gy, however, is only 15 %. The dvh 4.2.7 confirms the successful sparing of the spinal cord. The minimum dose of the spinal cord and the esophagus received by 1 % of the volume - which can also be thought as a measure of total maximum dose to an organ - is almost zero.

Figure 4.2.8 impressively shows the extension of the irradiated volume for CSI. The

<b>Patient spine sarcoma</b>		
CT slice distance [mm]	1.95	
CT voxel grid x(y) [mm]	1.95	
target volume [voxels] ([cm <sup>3</sup> ])	62501 (465.6)	
selected OARs	spinal cord	esophagus
# of beam directions	3	
beam angles [°]	115, 140, 220	
<b>Patient CSI</b>		
CT slice distance [mm]	1.95	
CT voxel grid x(y) [mm]	1.95	
target volume [voxels] ([cm <sup>3</sup> ]) Cranial	207687 (1547.3)	
target volume [voxels] ([cm <sup>3</sup> ]) Frontal	185880 (1384.8)	
target volume [voxels] ([cm <sup>3</sup> ]) Spinal	27038 (201.4)	
selected OARs	spine	optical nerve
# of beam directions	1	
beam angles [°]	180	
<b>Patient prostate</b>		
CT slice distance [mm]	2	
CT voxel grid x(y) [mm]	1.95	
target volume [voxels] ([cm <sup>3</sup> ])	9674 (73.8)	
selected OARs	rectum	bladder
# of beam directions	1	
beam angles [°]	120, 180, 230	

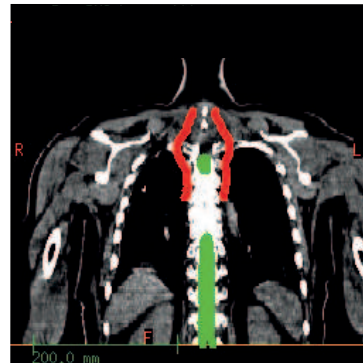
Table 4.2.5: Patient Data for 3D spot scanning dose delivery simulation study.

<b>TULIP beam delivery parameters</b>	
pulse rate $f$	120 Hz
delivery time per spot $t_{delivery}$	$1/f = 8.3$ ms
gantry speed $v_g$	$5.5^\circ/s$
couch speed $v_c$	$1 \frac{mm}{s}$
lateral scan speed $v_{scan,lat}$	$5 \frac{m}{s}$
magnet field change time $t_{mag}$	100 ms

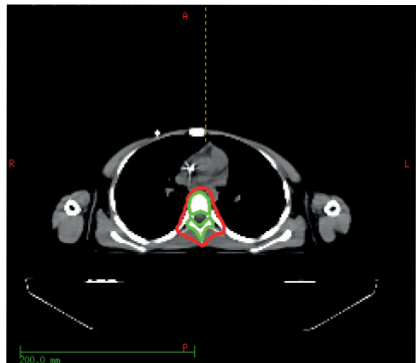
Table 4.2.6: TULIP specific beam delivery parameters.



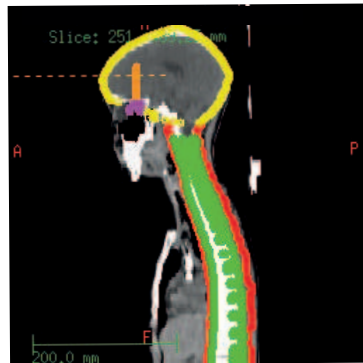
(a) CT Patient spine sarcoma: transversal view. Target: red; spinal cord: green, esophagus: blue.



(b) CT Patient spine sarcoma: frontal view. Target: red; spinal cord: green, esophagus: blue.



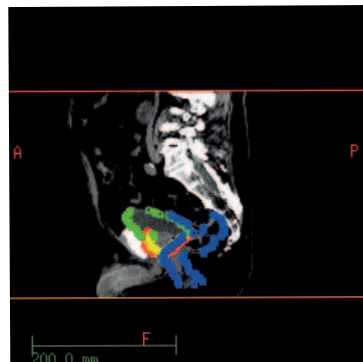
(c) CT Patient CSI: transversal view. Target: red, (yellow, orange); spine: green, (optical nerve: purple).



(d) CT Patient CSI: sagittal view. Target: red, yellow, orange; spine: green, optical nerve: purple.



(e) CT Patient prostate: transversal view. Target: red; prostate: yellow, rectum: green, bladder: blue.



(f) CT Patient prostate: sagittal view. Target: red; prostate: yellow, rectum: green, bladder: blue.

Figure 4.2.6: Different CT views for the three patients. The target volume and the selected critical organs are delineated.

Patient	PTV dose				OAR1		OAR2	
	$D_{presc}$ [Gy]	$D_{95}$ [Gy]	$D_{50}$ [Gy]	$D_5$ [Gy]	$V_{40}$ [%]	$V_{20}$ [%]	$V_{40}$ [%]	$V_{20}$ [%]
							spinal cord	esophagus
Pat spine sarcoma	70	63.4	69.7	72.1	15.1	16.5	0.2	4.4
							spine	left optical nerve
Pat CSI	36	35.5	35.9	36.3	24.3	32.4	-	45.8
							bladder	rectum
Pat prostate	80	75.3	79.9	81.8	24.3	32.4	12.0	25.1

Table 4.2.7: Results for 3D spot scanning dose delivery with TULIP.

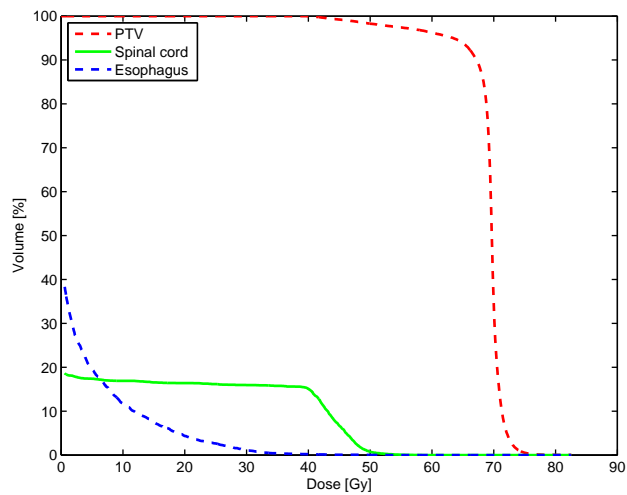


Figure 4.2.7: Inclusive dvhs for 3D spot scanning irradiation of the spine sarcoma. Dose losses to the PTV result from the spinal cord as an OAR lying directly within the PTV.

dose distribution reveals the good dose coverage of the target organs indicated by the dosimetric values given in table 4.2.7, that clearly show very good dose coverage of the spinal PTV.

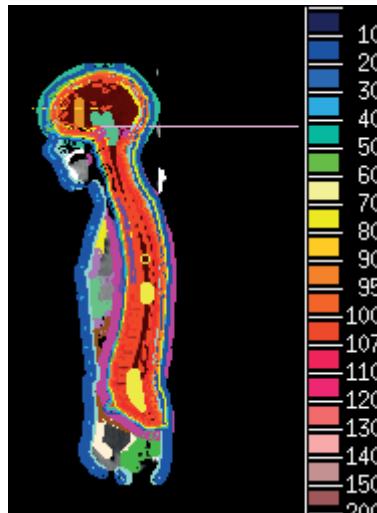


Figure 4.2.8: Dose distribution for craniospinal irradiation with TULIP. The dose values are given in % where  $D_{50}$  corresponds to 100%.

The dose distribution of the prostate PTV is compromised due to the vicinity of the rectum and the bladder. Both organs are very close to the PTV and need to be spared. In this case part of the rectum is included in the PTV leading to high local doses within the rectum. 12 % of the rectum volume receive a dose up to 40 Gy. However, a volume of 25 % receives up to 20 Gy and the dose to 1 % of the volume is 76.3 Gy as can be noticed by the dvhs in figure 4.2.9.

These results confirm what has been calculated with the treatment planning system and proves that by 3DSS with TULIP clinically acceptable dose distributions can be achieved. The more interesting and TULIP specific factor is the irradiation time. Results concerning the time are summarized in table 4.2.8. With TULIP, irradiation of the prostate with protons is feasible within 8.1 minutes assuming single fraction delivery which reduces to roughly 6 minutes for delivery in 40 fractions. Larger volumes as the spine sarcoma require more time mostly due to increased number of pulses. Table 4.2.8 gives the number of pulses that is not necessarily equal to the number of spots calculated by KonRad. TULIP has a limited number of protons that can be delivered within one pulse of the accelerator of  $5 \cdot 10^7$  due to limitations of the proton source. Whenever this maximum is exceeded, the spot is delivered by multiple beam pulses. The delivery time is calculated simply by multiplying the number of pulses with the inverse of the repetition rate. Here, it is important to mention that part of the results in table 4.2.8 assume a single fraction delivery which is not carried out in reality. Therefore, additionally,

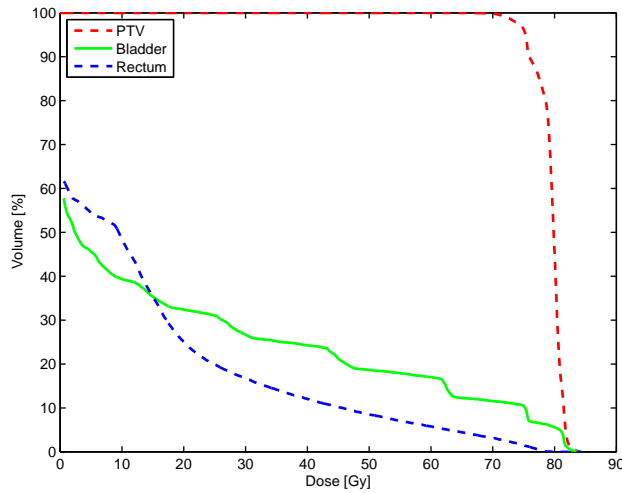


Figure 4.2.9: Inclusive dvhs for 3D spot scanning irradiation of the prostate.

the irradiation time for one fraction in a common fractionation scheme is indicated. For calculation of the irradiation time, the number of pulses is crucial and therefore specified in the table. The total irradiation time is calculated by summation of the different contributions as they are delivery time, lateral scan time to move the beam between the spots of one slice, the time to change the magnet field strength if the range variation is exceeded and the time to move the couch to the next isocenter position, if the field size exceeds 20 cm in one or both transversal directions. The residual time is needed to move the gantry between the different gantry positions. Therefore, it is emphasized here, that what is given here as the total irradiation time comprises the gantry motion time. During that time, the beam is switched off.

Patient	#b	#f	# pulses [min]	$t_{total}$ [min]	$t_{delivery}$ [s]	$t_{scan}$ [s]	$t_{mag}$ [s]	$t_{couch}$ [s]
Pat <sub>spine</sub>	3	1	212241	33.6	29.5	219.0	9.3	0
	3	(35)		(20.5)				
Pat <sub>CSI</sub>	4	1	319798	60.4	44.4	391.9	1.6	570
	4	(20)		(25.5)				
Pat <sub>prost</sub>	3	1	49587	8.1	6.8	49.3	3.3	0
	3	(40)		(6.3)				

Table 4.2.8: Irradiation time for 3D spot scanning with TULIP for single fraction delivery and multiple fractions indicated in round brackets. The number of beams and fractions are denoted as #b and #f, respectively.

### 4.2.2.3 Discussion

The results presented in the previous section show that 3D spot scanning is feasible with TULIP for various tumors. The dose was planned to match or outmatch the dosimetric planning results for photon tomotherapy treatment plans and fulfilled the clinical goals on an individual basis. Regarding the irradiation time, delivery of the dose of one fraction in 6 minutes for the prostate is feasible. Irradiation of the prostate with photons usually requires more than 5 minutes depending on the specific treatment plan and irradiation technique [Steiner et al., 2013]. Delivery of one fraction dose to the spine sarcoma took 20 minutes due to the high number of pulses needed even for fractionated dose delivery. For craniospinal treatment with helical tomotherapy, Sterzing et al. [2008] observed radiation times of 9.5 minutes. With dynamic jaws, treatment times for helical tomotherapy might be improved further [Krause et al., 2012]. For proton therapy with pencil beam scanning, Timmermann et al. [2007] found irradiation times of 21 minutes for craniospinal irradiation. 25 minutes achieved for craniospinal irradiation with TULIP is comparable to what was reported by Timmermann et al.. Treatment times comparable to those reported for tomotherapy could not be reached.

It should be emphasized here, that for TULIP the irradiation time strongly correlates to the number of spots and the number of protons per spot. With a technical limit of  $5 \cdot 10^7$  protons per spot imposed by the source, it might occur that one spot exceeding the maximum number of protons per spot is delivered in several pulses which increases the delivery time. Therefore, an increase of the number of protons per pulse should be considered. This could be realized by another proton source capable of delivering more protons per pulse or by using multiple sources.

Another solution to decrease the irradiation time could be to increase the spot grid, thus a reduction of the number of spots. A reduction of spots might come along with reduced steepness of dose gradients. Whether this is still an applicable solution without too much harm to the dose distribution strongly depends on the individual patient case with its specific positions of target volumes and OARs. The number of spots could also be decreased for different dose delivery techniques. With Distal Edge Tracking (DET), which might be applicable in many cases, the number of spots could be massively reduced. In summary, on an individual basis, both methods could be a promising approach to decrease the irradiation time.

### 4.2.3 Influence of breakdown rate on the dose distribution

As described in section 3.1.3 and 4.2 for very high field gradients, a breakdown of the electric field might occur. According to the experimental data found by Degiovanni et al. [2011], Andres et al. [2012] and Amaldi et al. [2012] breakdowns might happen with a breakdown rate (BDR) in the order of  $3 \cdot 10^{-6}$  bpp/m (breakdowns per pulse per meter) which corresponds to  $3.3 \cdot 10^{-5}$  bpp for an accelerator length of 11 m, thus one

breakdown every 400 s. Assuming one fraction to be 5 minutes, this roughly results in one breakdown for each fraction. In the following, the influence of breakdowns at several breakdown rates is studied for two patient cases.

#### 4.2.3.1 Materials and Methods

Two patient cases were investigated - one receiving a craniospinal irradiation and one with a lung tumor, which, for the purpose of this study is assumed to be static. The first patient is the same patient as described in section 4.2.2.1, the parameters for the lung patient are summarized in table 4.2.9.

<b>Patient lung</b>	
CT slice distance [mm]	2.5
CT voxel grid x(y) [mm]	0.98
target volume [voxels] ([cm <sup>3</sup> ])	77125 (183.9)

Table 4.2.9: Patient Data for studying the influence of BDRs on the dose.

For the two patient cases, static treatment plans were calculated to be used as input for the dose calculation algorithm TuDoCa. The prescribed dose to the PTV for the CSI patient is 36 Gy and 60 Gy for the lung patient. To model breakdowns with a BDR  $r$  within the dose delivery, every  $r^{th}$  spot is deleted and not delivered. Thereby, the number of spots is reduced according to the BDR. For the CSI patient breakdowns every  $10^{-4}$  -  $10^{-5}$  pulse have been modeled for a single fraction delivery. For the lung patient, breakdowns every  $10^{-3}$  -  $10^{-6}$  pulse for single fraction delivery were simulated, and  $10^{-3}$  -  $10^{-4}$  bpp for dose delivery in 10 fractions.

The results are indicated in terms of maximum dose differences occurring for delivery with and without breakdowns and corresponding dose distributions are shown for selected cases.

#### 4.2.3.2 Results

Dose distributions were calculated assuming different BDRs. Maximum dose differences between the dose distribution calculated for a certain BDR and dose distributions assuming no breakdowns are summarized in table 4.2.10. As one might notice, the number of pulses deleted does not exactly correlate with the fraction of pulses that can be derived by the original number of pulses, denoted as  $\# \text{ pulses}_{orig}$  and the BDR. This is due to the different subdivision of spots according to the maximum number of protons in a spot and due to numerical reasons during calculation. Altogether, the dosimetric effect due to breakdowns is rather minor in almost all investigated cases. For all BDR smaller than  $10^{-3}$  bpp the maximum local dose differences are below 1 Gy which does

not massively influence the resulting dose distribution. Only if every 1000th or more of the planned spots are not delivered, we noticed maximum local dose differences of 5.2 Gy. For the same patient and BDR with fractionated delivery the maximum observed dose difference is 1.3 Gy. Figure 4.2.10 shows the difference between the dose distributions for the lung patient between dose calculations assuming no breakdowns and assuming a BDR of  $10^{-3}$  bpp. Looking at the difference of the dose distributions on the bottom, one can notice that on the shown slice indeed one spot is missing.

Patient	#f	BDR [bpp]	# pulses <sub>orig</sub>	# pulses <sub>used</sub>	$ D_{diff,max} $ [Gy]
Patient CSI	1	$10^{-4}$	9147828	9147628	0.35
Patient CSI	1	$10^{-5}$	9147828	9147810	0.35
Patient Lung	1	$10^{-3}$	92215	92081	5.2
Patient Lung	1	$10^{-4}$	92215	92207	0.31
Patient Lung	1	$10^{-5}$	92215	92215	0
Patient Lung	1	$10^{-6}$	92215	92215	0
Patient Lung	10	$10^{-3}$	69804	69750	1.3
Patient Lung	10	$10^{-4}$	69804	69799	0.22

Table 4.2.10: Influence of breakdowns on the dose for single fraction (#f=1) and fractionated delivery (#f=10). Maximum dose differences between dose distributions without breakdowns and those taking into account a specific breakdown rate.

#### 4.2.3.3 Conclusion

Since breakdown of the electric field might occur during patient treatment with TULIP it is important to be aware of the potential influences on the dose in the patient. Therefore, we have investigated the effect of breakdowns during dose delivery with TULIP by simulation of this dose delivery process. Within a wide range of potentially occurring breakdown rates, we have observed almost no effect on the resulting dose distributions. Only for unrealistic breakdown rates greater than  $10^{-3}$  bpp, we noticed influences slightly greater than 1 Gy for fractionated delivery within 10 fractions and over 5 Gy for single fraction dose delivery. Since single fraction dose delivery is not a realistic scenario but was rather studied as a worst case example, we found the influence of breakdowns within the investigated ranges to be minor. For TULIP former experimental studies revealed realistic BDRs of  $3.3 \cdot 10^{-5}$  bpp which is far away of the BDR which has been found to be a critical limit for the investigated cases here of  $10^{-3}$  bpp. Of course, the influence of breakdowns changes with the number of spots and thereby with the fraction dose delivered by one spot. If the same dose is delivered by more spots than in the original plan, the fraction dose of one spot decreases and with its influence in case it is

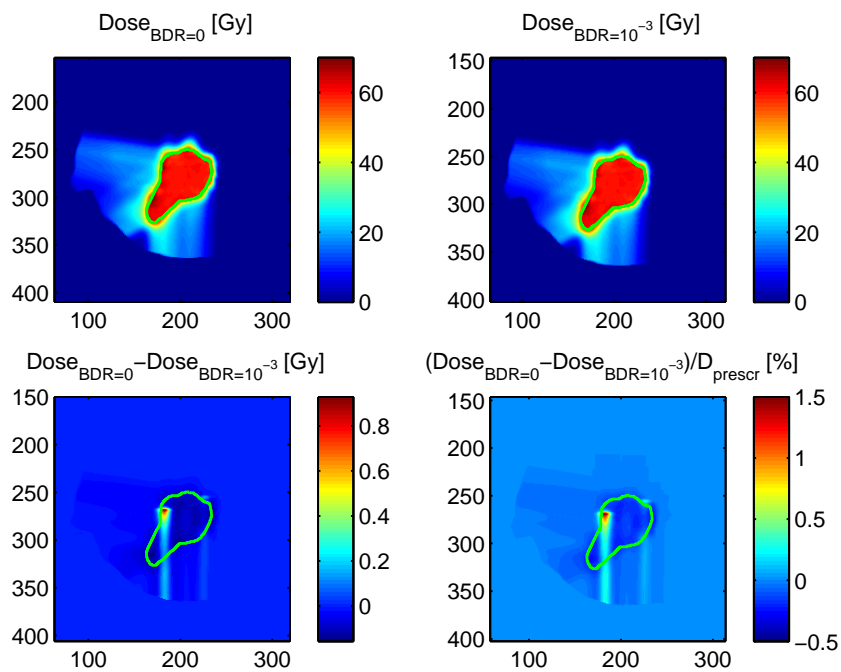


Figure 4.2.10: Dose distributions for a lung patient for different BDRs. The target volume is delineated in green. On the top left picture, the dose distribution without breakdowns is shown on a representative transversal slice. On the right top the same slice but with a BDR of  $10^{-3}$  bpp. On the bottom the differences between the dose distributions are shown. One can notice that on the shown slice one spot is missing.

not delivered due to breakdown. Therefore, plans with spots set more closely and thus an increased number of spots are considered to be less sensitive than plans with broad spot grids. However, the evaluated cases here represent two realistic examples where the spots are placed on a 3 mm lateral spot grid. Therefore, our results manifest, that for most treatment plans and realistically occurring breakdowns, their influence on the dose distribution is negligible.

### 4.3 Discussion and Conclusion

Within this chapter, first, the TULIP specific dose delivery simulation software 'TuDoCa' has been introduced in section 4.1, followed by the results achieved for dose delivery to static tumors in section 4.2. Major part of this work was the development of a dose delivery simulation algorithm that includes the essential TULIP beam delivery parameters and calculates time dependent dose distributions. We have introduced and successfully evaluated that algorithm (4.1.1, 4.1.2). The algorithm showed to match the required features, machine specific beam parameters can be varied for individual dose calculations. For further research the algorithm will be used for dose delivery simulation to moving targets as described in chapter 5. During the evaluation of TuDoCa, we noticed the sensitivity of proton dose calculation to even small setup errors. Therefore, additional effort was put into investigation of the dosimetric influence caused by small misalignment for different proton dose delivery methods. We noticed crucial influence on the resulting dose distributions for submillimeter position shifts during radiation therapy treatment with protons. The dynamic rotational dose delivery method seems to be particularly sensitive to misalignments that can occur during radiation therapy. We observed dose deviations that cannot be easily handled by the use of margins. This is one aspect why dynamic rotational dose delivery is not particularly favored by us for application with TULIP.

This conclusion has been confirmed by the results achieved for dose delivery simulation with TULIP to static targets (4.2). Dynamic rotational dose delivery includes technical as well as dosimetric challenges. From the technical aspect an optimized composition of gantry speed and pulse rate is required to achieve dose distributions comparable to static ones. However, the technical limit for the pulse rate is 120 Hz, the gantry rotation speed should be within the range of 1 to 3 rpm to assure smooth gantry motion and minimized harm to the material. Regarding the dose distributions the unwanted dose outside the target is a major critical aspect of rotational dose delivery. For 3D spot scanning with a fixed and limited number of incoming beam directions, critical organs can be spared better by considerate patient and beam alignment. Between incoming fields, there are regions where the dose is zero. This cannot be easily achieved by rotational dose delivery.

Rotational proton therapy has not yet been studied or even used in clinical routine,

but there are investigations concerning proton arc therapy where multiple static beam directions are used. [Rechner et al. \[2012\]](#) found a decreased risk of radiogenic second cancer of organs at risk for arc therapy of the prostate with protons compared to volumetric arc therapy in certain cases. They used 16 static proton beams to deliver the dose. [Sandison et al. \[1997\]](#) studied proton arc therapy for treatment of the chest wall. In comparison to electron arc therapy the dose to the lung was reduced. [Sengbusch et al. \[2009\]](#) studied proton arc therapy with regard to maximum energies needed for new compact accelerator designs. They concluded that the maximum accelerator energy needed could be reduced if having the ability of treating patients also with arc therapy which could decrease the path length, thus the energy. Arc therapy, and potentially also dynamic rotational therapy with protons can deliver homogeneous dose distributions with low dose to organs in direct vicinity. However, due to multiple beam directions, the dose is spread all around the treated volume. In the cases we have studied, we could hardly observe dosimetric benefit due to rotational therapy. Additionally, we found irradiation times to be increased for rotational dose delivery with TULIP. Altogether, our studies gave no convincing reason to use rotational dose delivery with TULIP.

Therefore, we studied dose delivery with two lateral scanning magnets and found good clinical results from a dosimetric point of view. Concerning the irradiation times, we found that TULIP has the ability to deliver one fraction of the prescribed dose to a prostate tumor in less than 6 minutes. Compared to photon therapy treatment which would require 5 or more minutes this is an encouraging result. Also, for very time elaborate craniospinal irradiation we calculated irradiation times of 25 minutes for delivery of one fraction of dose.

For further investigation of the features of TULIP, we studied the dosimetric influence of breakdowns of the electric field. For the experimentally found value of  $3.3 \cdot 10^{-6}$  bpp/m ([Amaldi et al., 2012](#)), the results of the simulation study do not reveal a harmful effect of these breakdowns.

In summary, TULIP is able to deliver proton plans by 3D spot scanning for most realistically occurring tumors on a short time scale. Based on our studies, the irradiation time could be decreased simply by using a more powerful proton source, that would allow for delivery of more protons per pulse.

In conclusion, with TULIP 3D active spot scanning without the use of degraders and modulators is feasible that are required in other single room facilities as proposed by [Mevion Medical Systems \[2012\]](#) (MEVION S250) and IBA (ProteusOne) [[IBA, Proton Therapy, 2012](#)]. This clear advantage is further enhanced, with respect to MEVION 250, by the fact that the dose distribution is active and not passive.

# Chapter 5

## Dose delivery to moving tumors with TULIP

### 5.1 Introduction

TULIP provides excellent characteristics for the treatment of moving tumors with protons. With pulses of maximal  $5 \cdot 10^7$  protons that can be delivered on a millisecond time base, it is superbly suited for motion mitigation techniques such as rescanning, tracking, or even better, a combination of both. As described in section 2.5, rescanning attempts to average out motion induced local misdosages by delivering the dose in multiple rescans. Naturally, this increases the irradiation time. As reported in the literature, rescanning is also studied in combination with gating, in which dose delivery is restricted to a predefined time or motion interval to further mitigate the effects of motion ([Furukawa et al., 2010], [Mori et al., 2013b]). TULIP provides high flexibility by patient positioning on a movable and rotatable couch, a wide range of potential gantry positions and very fast beam delivery. Therefore, with rescanning there is great potential to save irradiation time by very fast dose delivery while still using active energy variation compared to methods currently available with synchrotrons or cyclotrons. For synchrotrons, the major challenge for treatment of moving organs is the energy variation time of several seconds. For a cyclotron based proton acceleration with the Gantry 2, PSI pursues the way towards fast spot scanning dose delivery which is thought to open the way to treat also moving targets [Zenklusen et al., 2010]. However, since a cyclotron is used, energy variation is performed within 80 ms using a degrader, while lateral scanning requires only few milliseconds. With TULIP the energy variation time can be reduced roughly by a factor of 10. Therefore, the time required for rescanning is expected to be also severely reduced. Also, due to shortening of scanning times, the motion happening within one rescan might be reduced which can beneficially affect the resulting dose distributions.

We want to investigate well the TULIP concept is suited for treatment of moving tumors with rescanning. Therefore, we have performed dose delivery simulation studies based on the extended version of 'TuDoCa' (see section 4.1) for dynamic targets. In the following the modifications of the dose delivery simulation software are described (5.2), followed by the results for dose delivery simulations to two lung and one liver tumor (5.3).

## 5.2 Materials and Methods

### 5.2.1 4D dose delivery simulation algorithm

The dose delivery simulation algorithm described in section 4.1 has been modified and used for dose delivery simulation to moving tumors. Changes to the patient input data and modifications to the dose calculation and summation software code were necessary. An overview of the relevant changes is given by the flow chart in figures 5.2.1 and 5.2.2 indicating the main process flow. Of course, the patient CT data for all motion phases and a measured motion signal has to be read in. Prior to dose calculation, the CT phases are correlated to the motion signal, thus to time. The acquisition of 4DCT data is described in the following section. Subsequently, a list containing all spots for all fractions and all beams is built similar to the dose delivery simulation for static targets. Thereby, each spot  $i$  is correlated to the time of its delivery  $t_i$ , which comprises all steps (scanning, gantry motion, couch motion, magnet change) that potentially might be performed to reach the current spot position. Through the time, the current spot is assigned to the corresponding CT phase. In the end of this simulation step, for each phase a list of appendant spots is built. Once all spots are correlated to their motion phases, the dose calculation for each fraction  $f$  is performed. For each CT phase  $j$ , the dose for all dedicated spots  $i$  denoted as  $D(f,j,i)$  is calculated, remapped to a reference phase  $D(f,ref)$  and summed for all phases. The remapping is performed with help of the displacement vectors giving the displacement between each motion phase and a reference phase, gained by image registration. As reference the maximum exhalation phase has been chosen. It is the same phase as used for treatment planning. After the dose of all spots of all phases for one fraction is accumulated, the next fraction of dose is calculated the same way and summed. Between each fraction a random time step is inserted to avoid matching time patterns for subsequent fractions. The result is the accumulated dose distribution over all motion phases and fractions.

The algorithm accounts for anatomic changes by using CTs from different motion phases. The amount of motion over time is accounted for by the measured motion signal. The motion signal was not measured during radiation therapy but during CT acquisition. This means that the CTs used for the simulation can only represent the anatomic changes induced by the motion during the time of CT acquisition. In a realistic

situation the motion during treatment might differ from the motion during acquisition of planning CTs. For the simulation approach used here, we are assuming identical motion at the time of CT acquisition and during irradiation. The reader should be aware of this, when evaluating the results.

Another intrinsic drawback of the method used here might be the motion measurement and the correlation to tumor motion. As reported in section 2.5.3.1, by using a strain gauge for motion measuring, only movement of the abdomen mainly caused by breathing can be measured. One cannot directly assume a correlation between motion of the thorax or abdomen and the tumor located within the lung or liver. However, building a correct correlation model is beyond the scope of this work. And for the purpose in the context of this work, namely to correlate the CT phases to the time by using the measured motion signal, we consider that assumption to be valid and directly correlate the measured motion signal with the tumor movement.

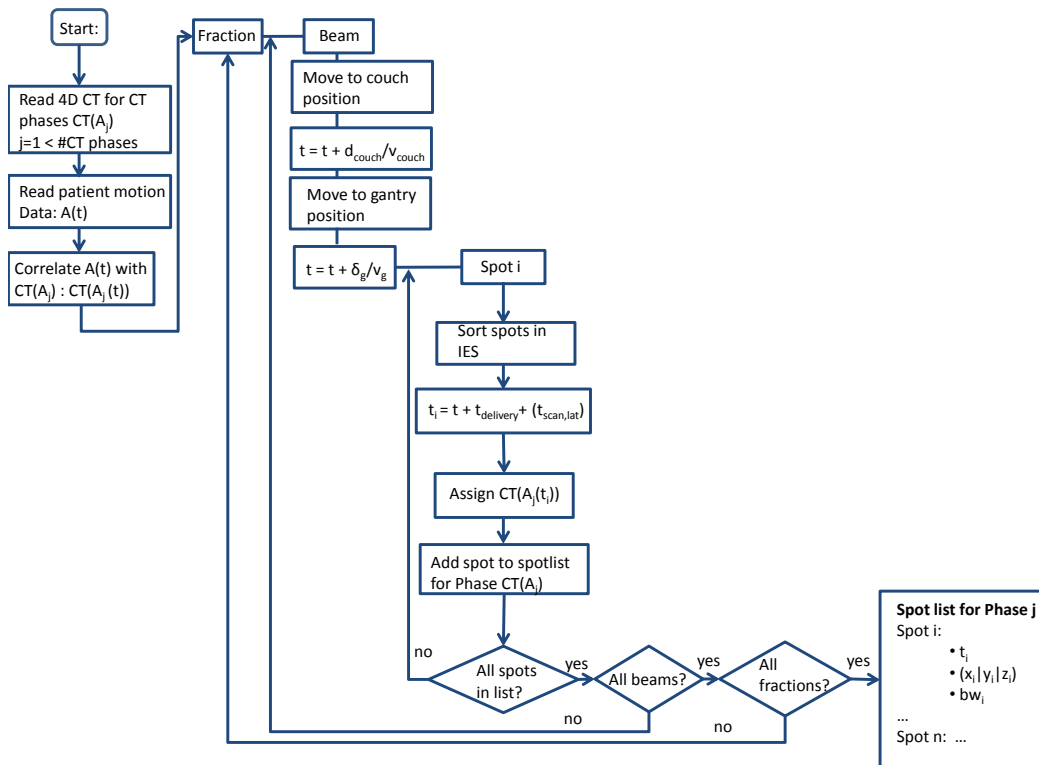


Figure 5.2.1: Process flow of 4D dose delivery simulation software. The processes flow before the dose calculation and accumulation is shown. In the described steps a list of spots for the subsequent dose calculation is created.

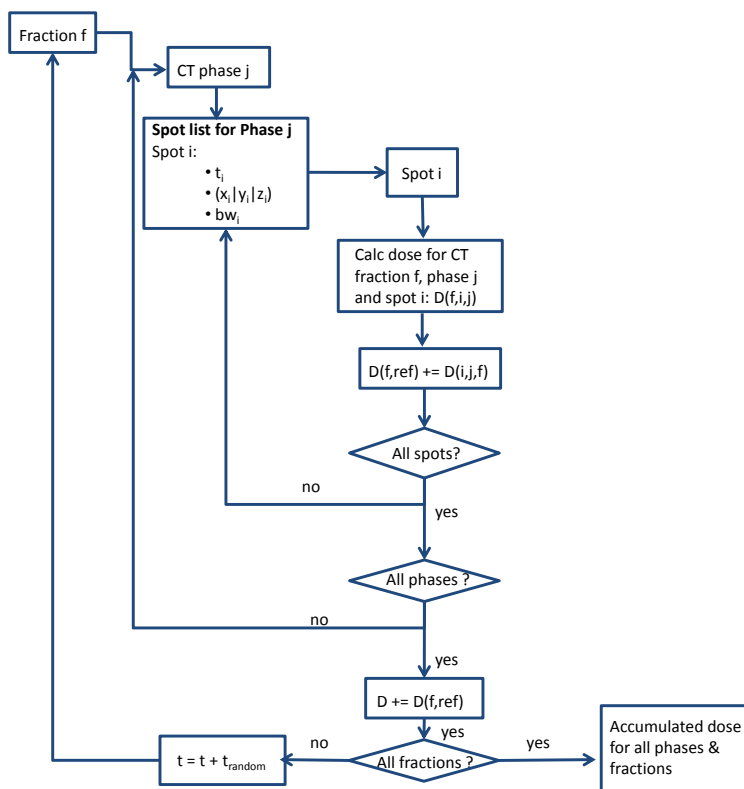


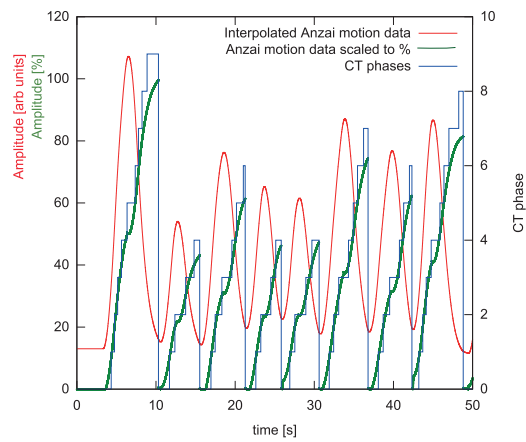
Figure 5.2.2: The dose calculation and accumulation steps based on the spot list generated with the process shown in 5.2.1 is shown.

## 5.2.2 Input data

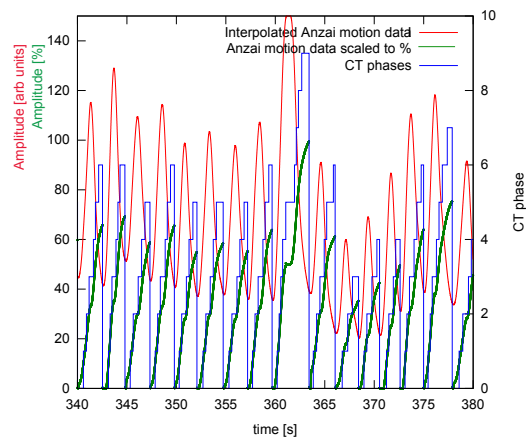
Similar as for dose delivery to a static tumor, patient specific CT data is required for dose delivery simulation to moving targets. However, not only one static CT scan is needed, but multiple CT scans describing the motion induced anatomic changes between different scans. Therefore, a 4DCT scan was acquired for each patient. The motion of the patient's thorax was measured by using a strain gauge around the thorax. Here, only tumors within the patient's thorax and abdomen (lung, liver) were examined. Triggered by the amplitude of the motion signal, a CT scan was taken recording the current anatomic situation. The amplitude steps triggering the CT scans for the individual patients are indicated in table 5.2.1. Each 4DCT consists of 7 or 10 CT scans for different motion states. As for static dose delivery, these CT scans were used as input to the dose delivery simulation software TuDoCa to determine the correct stopping ranges for the protons penetrating the tissues. The measured motion signal also serves as input for the software tool. The CT scans for the different motion phases are correlated to time by the motion curve for time dependent dose calculation. This correlation is based on the motion amplitudes that originally triggered the CT scan. The motion signal only provides arbitrary values of chest wall expansion that can be correlated to air filling of the lung during breathing. Therefore, the percentage air filling of the lung, as indicated in table 5.2.1, is used to correlate the CT phases to the motion signal again. The motion curves for the individual patients as well as correlated CT phases are visualized in figure 5.2.3.

Patient	LU1/LU2				
CT phase	0	1	2	3	4
Inhale [%]	0-20	20-40	40-60	60-80	80-100
CT phase	5	6	7	8	9
Inhale [%]	100-80*	80-60*	60-40*	40-20*	20-0*
Patient	LI				
CT phase	0	1	2	3	
Inhale [%]	0-25	25-50	50-75	75-100	
CT phase	4	5	6		
Inhale [%]	100-70*	70-40*	40-0*		

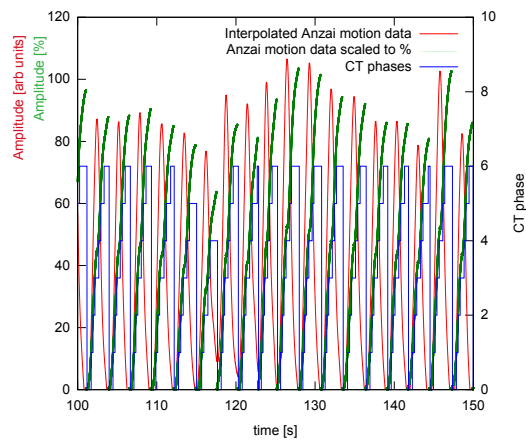
Table 5.2.1: CT acquisition steps for the individual patients. The percentage of air filling of the lung measured with a strain gauge is given in percent of maximum inhalation/exhalation. 100 % corresponds to maximum inhalation. Values labeled with '\*\*' refer to exhalation. Again 100 % refers to full inhalation.



(a)



(b)



(c)

Figure 5.2.3: Measured motion data and correlated CT phases for the lung patients LU1 and LU2 in picture (a) and (b) and for the liver patient in (c).

The amount of mean tumor motion was assessed through the CT phases. Knowledge of the amount and direction of motion between the CT phases is gained through deformable image registration using the registration software "OnQ rts" commercialized by OSL Oncology Systems Limited. The software calculates the displacement vectors for each voxel between the motion phases taking voxel deformations into account. From this data the mean amount of voxel motion for the tumor is derived. Amplitudes refer to peak-to-peak values and are presented for each direction of motion in table 5.2.2. This data was used to scale the motion signal measured with the ANZAI belt which, in the first place, gives only arbitrary motion values correlated with the patient's breathing. In figure 5.2.4 the resulting data is presented in terms of mean values and standard deviations for period, peak-to-peak amplitude and baseline shift. The data are also indicated in table 5.2.2.

Parameter	LU1	LU2	LI
$\bar{a}_x \pm a_{std,x}$	$0.21 \pm 0.7$	$1.69 \pm 0.5$	$2.79 \pm 1.5$
$\bar{a}_y \pm a_{std,y}$	$0.30 \pm 0.8$	$-2.32 \pm 0.7$	$-1.77 \pm 0.8$
$\bar{a}_z \pm a_{std,z}$	$8.80 \pm 2.4$	$3.39 \pm 0.9$	$9.05 \pm 2.3$
$\bar{a}_{Anzai} \pm a_{std}$ [mm]	$8.87 \pm 2.4$	$4.51 \pm 1.0$	$9.76 \pm 2.4$
$\bar{b}_{S_{Anzai}} \pm b_{S_{std}}$ [mm]	$-0.01 \pm 0.9$	$-0.02 \pm 1.79$	$0.0 \pm 1.2$
$\bar{p}_{Anzai} \pm p_{std}$ [mm]	$5.4 \pm 0.9$	$2.5 \pm 0.4$	$2.5 \pm 0.4$

Table 5.2.2: Patient motion parameter values as derived with deformable image registration. Mean and standard deviation are calculated for the tumor volume in all directions of motion separately. The motion values marked with "Anzai" refer to the average motion over the different directions and are used to scale the measured motion signal. The amplitude is denoted as a, bs refers to baseline shift and p to period.

In total three different patient cases have been examined here. Two lung patients, denoted as LU1 and LU2, as well as one liver patient LI [Data: HIT/GSI]. Both tumors are mainly affected by respiratory motion. For each patient an Internal Target Volume (ITV) as referred to in section 2.4.3 was delineated to encompass the tumor volume in all motion states. All target contours as well as organs at risk were delineated on the maximum exhalation phase which serves as a reference phase in the following. The anatomic tumor position in full exhalation phases as well as the target and selected contours of OARs are shown in figure 5.2.5. For each patient a static proton treatment plan was calculated using the treatment planning system KonRad [Nill et al., 2004]. As in the static case, spots were set on a 3 mm lateral between adjacent lateral spots and with energy steps according to 1 mm range differences. For the investigation of rescanning with a reduced number of spots, additionally, a treatment plan was calculated for

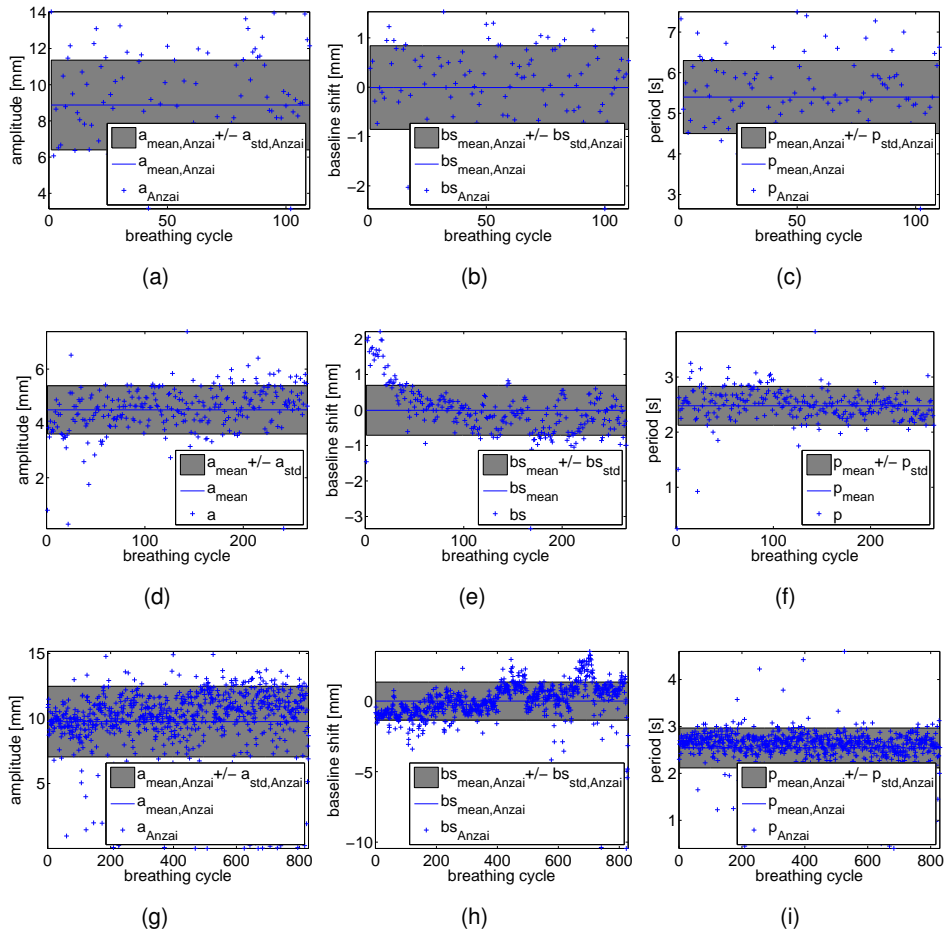


Figure 5.2.4: Motion parameter values for the individual patients: (a)-(c) for lung patient LU1, (d)-(f) for lung patient Lu2 and (g)-(i) for liver patient LI. a refers to amplitude (mean over all directions), bs refers to baseline shift and p to period.

patient LU1 using a 6 mm spot grid in all directions. The dose was prescribed and optimized to the ITV in order to yield 100 % of the CTV to receive between 95 % and 107 % of the prescribed dose. Plan optimization has been performed on the full exhalation phase. All patient specific input data are summarized in tables 5.2.3 and 5.2.4.

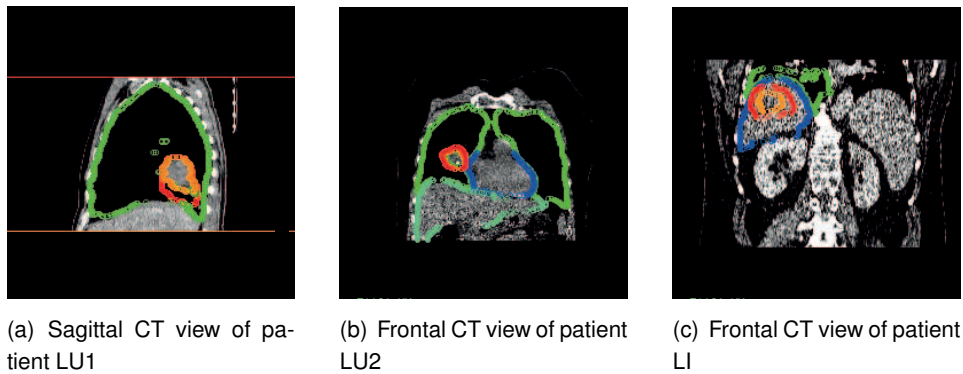


Figure 5.2.5: CT views of lung patients LU1 (a) and LU2 (b) and liver patient LI (c). The ITV (red), GTV/CTV (orange) and some selected critical organs are delineated: lung (green), heart (blue) in (b), liver (blue) in (c).

Patient	# CTs	CT voxel grid x=y=z[mm]	ITV volume [voxels] ([cm <sup>3</sup> ])	CTV <sub>exh</sub> volume [voxels] ([cm <sup>3</sup> ])
LU1	10	0.98	197133 (183.5)	109257 (101.69)
LU2	10	0.98	76495 (71.2)	54973 (51.2)
LI	7	0.98	175456 (163.21)	85960 (80.01)

Table 5.2.3: CT data for lung (LU1, LU2) and liver (LI) patients.

### 5.2.3 Magnitude of motion induced effects

In order to assess the amount of motion induced effects on the dose distribution, first, the 4D dose delivery algorithm described above was used to simulate dose delivery to a moving tumor. As machine parameters, TULIP specific values were used as summarized in table 5.2.5. For all dose delivery simulations 3D spot scanning was applied. Therefore, the gantry is only rotating to move to the next fixed beam position.

For each of the three cases dose delivery to the static tumor was simulated by using only the reference (maximum exhalation) phase for which the static treatment plan was optimized to calculate the dose. In the following, this case is referred to as 'static' and

Patient	$D_{presc}$ [Gy]	# beams	beam angles [°]
LU1	60.0	1	180
LU2	63.8	2	270, 345
LI	32.4	1	180

Table 5.2.4: Treatment planning data for lung (LU1, LU2) and liver (LI) patients. Angles are reported according to IEC standard [IEC standard].

<b>TULIP beam delivery parameters</b>	
pulse rate $f$	120 Hz
delivery time per spot $t_{delivery}$	1/f=8.3 ms
gantry speed $v_g$	6°/s
couch speed $v_c$	1 $\frac{mm}{s}$
lateral scan speed $v_{scan,lat}$	5 $\frac{m}{s}$
magnet field change time $t_{mag}$	100 ms

Table 5.2.5: TULIP specific beam delivery parameters.

serves as a reference to which the other simulation results assuming tumor motion are compared. For evaluation of the magnitude of motion induced effects on an individual patient basis, dose delivery was simulated as described in section 5.2.1 for a single fraction and for multiple fractions without employing any motion mitigation method.

The dosimetric results are again represented by minimum doses to 99 %, 50 % and 1 % of the target volume and dose volume histograms. Additionally, a homogeneity index is calculated:

$$HI = \frac{D_5 - D_{95}}{D_{prescr}}, \quad (5.2.1)$$

where  $D_{prescr}$  is the prescribed dose and  $D_{95}$  and  $D_5$  the minimum dose received by 95 % and 5 % of the target volume. According to this formula, the better the dose distribution, the smaller the homogeneity index, implied  $D_{50}$  to be close to the prescribed dose.

## 5.2.4 Rescanning

In order to simulate dose delivery by using rescanning as one motion mitigation technique as described in section 2.5, the basic dose calculation code remained the same, but small changes were made. In a first approach we decided to model scaled volumetric rescanning as described by Zenklusen et al. [2010] to see the general effect of

rescanning on the dose distribution and to derive irradiation times for this rather simple technique.

The modifications applied to the simulation software code, as described in section 5.2.1, affect the creation of the spot list as depicted in figure 5.2.1. The spot weights are scaled by the number of rescans. The spot order for one scan remains the same but is repeated subsequently for the number of rescans applied. Consequently, the spot list is expanded and includes all spots for one volumetric scan after the other. All subsequent steps remain as described above.

We simulated dose delivery in 10 rescans to the moving tumors of all three patients in a single fraction. The dosimetric results were evaluated by minimal doses received by 99 %, 50 % and 1 % of the GTV (LU2) or CTV (LU1, LI) as delineated on the maximum exhale phase for which the treatment plan was optimized. Dvhs and dose distributions serve to visualize these effects. Additionally, the effect on the homogeneity was evaluated by calculating the homogeneity index as defined in formula 5.2.1.

In comparison to existing proton accelerators it is of particular interest to study irradiation times, since this is one drawback of rescanning (and also gating) and may be one obstruction for the wide spread application of this method. Therefore, total irradiation times, the lateral scan times and spot delivery times are calculated. Furthermore, the same quantities are calculated for irradiation using rescanning with a common synchrotron used as proton accelerator. For TULIP no additional energy change time is needed. The irradiation time calculation for TULIP is based on the parameters given in table 5.2.5. For the synchrotron, the same parameters were used and additional energy change time of 1.5 s was assumed. Due to the effect of dose averaging caused by rescanning, the impact on the dose distribution is not supposed to change due to the different time patterns of TULIP and synchrotrons. This is exemplarily investigated for one patient case (LU2), for which also the dose distribution achieved by dose delivery with a synchrotron in 10 rescans was simulated and compared to the same dose delivery with TULIP.

The patient cases used for the rescanning study and corresponding treatment plans are the ones described in section 5.2.2.

## 5.3 Results

### 5.3.1 Magnitude of motion induced effects

Table 5.3.1 and figure 5.3.1 summarize the dosimetric results for dose delivery to a moving target and for comparison to a static tumor. Dose values are given for the CTV and for an organ at risk. For the lung tumor we indicate the volume of the lung receiving 20 Gy and for the liver tumor we present the same quantity for the liver. For the lung cases, tumor motion during irradiation obviously leads to detrimental and significant

underdosage as visualized in figure 5.3.1. The effects also manifest in a decrease of  $D_{99}$  by almost 10 Gy for LU1 and by 14 Gy for LU2 when the tumors moved. The misdosage for patient LU2 is shown in the dose distribution and dose difference plots in figure 5.3.2. For LU1 we also observed overdosage of 3 Gy to the CTV, which was less pronounced for the other lung patient. These dose deviations are displayed by the increased homogeneity index. For LU1 the HI increased from 2 % for static tumor irradiation to 13 % when tumor motion was applied. Similar effects occurred for LU2, where the HI increased from 5 to 18 %.

In the studied lung cases, the averaging effect of fractionation on the dose distribution was more pronounced for LU1. For this tumor, dose delivery in 10 fractions reduced the overdosage by almost 2 Gy. The dvh tended to approach more the course of the dvh for dose delivery to a static tumor. For LU2 the effects of fractionation on the resulting dose were minor.

Due to tumor motion the lung volume receiving 20 Gy was increased from 11.8 to 12.7 % which was not significantly reduced due to fractionation for lung patient LU1. For patient LU2  $V_{20}$  almost remained same, independent from tumor motion or fractionation. Generally, the effect on  $V_{20}$  was small.

For the liver patient studied, the detrimental effects on the dose distribution were less severe compared to the lung tumor irradiation. The dvh for static tumor irradiation was the steepest and reveals an excellent dose distribution. The maximum dose deviations in terms of  $D_1$ ,  $D_{50}$  and  $D_{99}$  were below 1 Gy for a moving tumor compared to dose delivery to a static tumor. The homogeneity index changed from 1 % to 3% in that case. However, figure 5.3.3 reveals impressively locally occurring dose deviations induced by anatomical changes. For fractionated delivery the dosimetric changes were subtle.

For all investigated patient cases irradiation times (including couch motion time) were below 8 minutes per fraction (see table 5.3.2). For dose delivery in 10 fractions for the lung patients and in 4 fractions for the liver patient, the total time per fraction reduced compared to single fraction dose delivery. This is due to the reduced number of protons per spot and less need to subdivide spots that exceed the source limitation of  $5 \cdot 10^7$  protons per pulse. Irradiation times amounted to less than 5 minutes per fraction for all studied cases.

### 5.3.2 Rescanning

Regarding the dosimetric results, rescanning improved the dose distribution compared to single scan irradiation for all investigated cases as visualized in figure 5.3.4. The results for moving tumor irradiation are summarized in table 5.3.3. For comparison the static tumor irradiation results are depicted, too. The overdosage was reduced and strongly approached the static tumor case for all patients. The maximum residual deviation from the static tumor irradiation was found for patient LU1, represented by a

Patient	motion state	#f	CTV				OAR	
			D <sub>99</sub> [Gy]	D <sub>50</sub> [Gy]	D <sub>1</sub> [Gy]	HI [%]	V20 [%]	
LU1	static	1	59.3	60.0	61.6	2	11.8	
	moving	1	49.5	60.0	64.6	13	12.7	
	moving	10	50.5	60.0	62.7	10	12.6	
LU2	static	1	59.7	63.8	66.2	5	10.9	
	moving	1	45.7	62.7	66.7	18	10.9	
	moving	10	48.3	62.8	66.0	18	10.9	
LI	static	1	32.2	32.4	32.7	1	7.3	
	moving	1	31.5	32.4	33.2	3	7.4	
	moving	4	31.7	32.4	33.0	2	7.3	

Table 5.3.1: Results for 4D spot scanning dose delivery in 1 or 10 fractions, denoted as (#f).

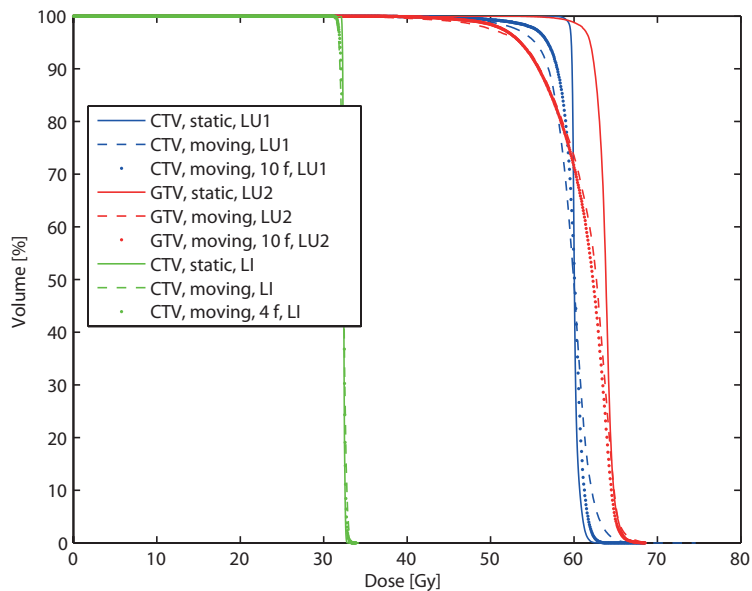


Figure 5.3.1: DVHs showing the magnitude of the effect of tumor motion on the dose distribution during irradiation for the CTVs (GTV).

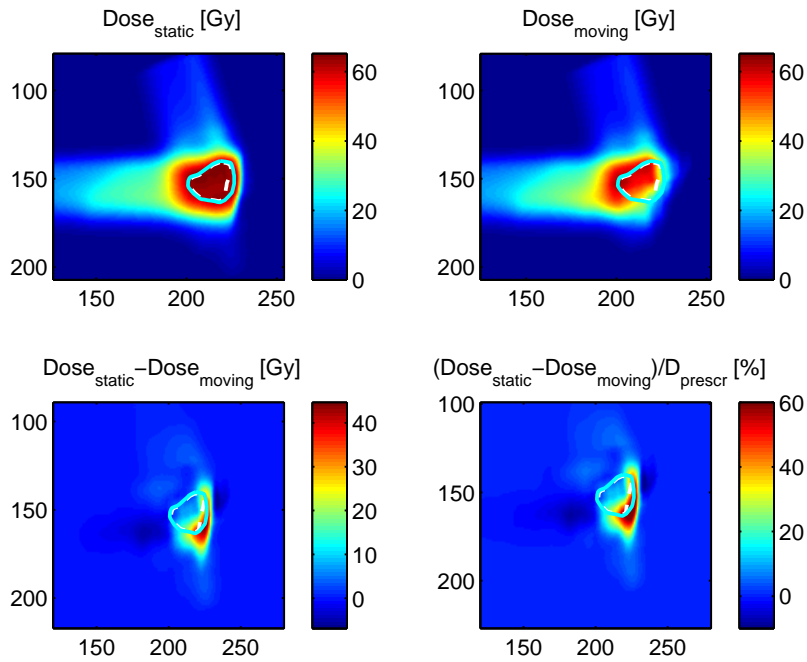


Figure 5.3.2: Dose distribution on a transversal slice for the moving lung tumor of patient LU2. The motion induced misdosage (top, right) compared to the dose distribution for a static tumor (top, left) is visible. The dashed white lines indicate the CTV and the cyan solid line the ITV. The bottom row shows the dose differences between dose delivered to a static and to a moving tumor in [Gy] (left) and [%] right.

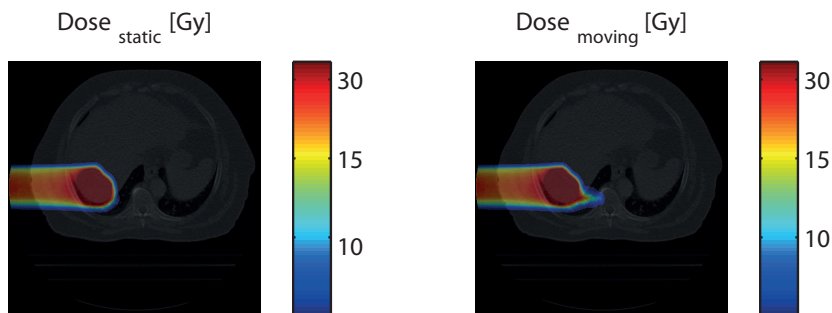


Figure 5.3.3: Dose distribution for the static (left) and moving (right) liver tumor of patient LI. The overshoot caused by motion induced anatomical changes can be seen.

Patient	#f	# pulses per fraction	$t_{total}$ per fraction [min]
LU1	1	55408	7.8
LU1	10	22616	3.2
LU2	1	26317	4.3
LU2	10	15828	2.6
LI	1	37259	5.3
LI	4	27765	4.5

Table 5.3.2: Irradiation times for 3D spot scanning with TULIP for moving tumors for single fraction dose delivery ( $\#f=1$ ) or dose delivery in 10 fractions ( $\#f=10$ )

difference in  $D_1$  of 1.3 Gy. For the other patients, values for  $D_1$  deviated even less from the results achieved by static tumor irradiation. Less improvement was achieved for the underdosage. For LU1 the minimum dose received by 99 % of the target volume was improved by 2.9 Gy, but an underdosage of 6.9 Gy from the dose to the static tumor remained for the small spot grid size of  $(\Delta x, \Delta y, \Delta z) = (3, 3, 1)$  mm. The increase of the spot size for patient LU1 reveals in an decreased homogeneity, which is also visualized in figure 5.3.6. The homogeneity index increased from 6 % for static tumor irradiation to 16 % with tumor motion. However, 10 rescans decreased the homogeneity again to 8 %. For the other lung patient (LU2)  $D_{99}$  increased by 3.7 Gy for irradiation to the moving tumor, when rescanning was applied, however, 10.3 Gy were lacking to approach the static tumor irradiation results. This is visualized in the dvhs shown in figure 5.3.4. For the liver patient LI the absolute dosimetric effects were smaller and also the impact of tumor motion was less compared to the lung tumors. However, rescanning improved the dose distribution already for 5 rescans. The course of the corresponding dvh almost matched the one of the static tumor irradiation when the dose was delivered in 10 rescans (see figure 5.3.5).

As expected, the dose averaging effect did not significantly change using the synchrotron time parameters compared to irradiation with TULIP for LU2. However, when comparing irradiation times, there is a striking increase for synchrotron dose delivery with rescanning. Dose delivery in 5 rescans with TULIP was feasible within 20 minutes per fraction for liver patient LI. For a synchrotron here additional time for changing the energy is required. Therefore, even for higher scan speeds and smaller delivery times, 11.6 minutes for energy change are needed for volumetric spot scanning in this case. Impressively, the influence of the spot grid, thus the decreased number of spots is shown for LU1 and a spot grid of 6 mm in all directions. One fraction with 10 fold rescanning could be delivered within 3.5 minutes.

Pat	spot grid ( $\Delta x, \Delta y, \Delta z$ ) [mm]	motion state	#s	GTV/CTV			
				D <sub>99</sub> [Gy]	D <sub>50</sub> Gy]	D <sub>1</sub> Gy]	HI [%]
LU1	(3,3,1)	static	1	59.3	60.0	61.6	2
	(3,3,1)	moving	1	49.5	60.0	64.6	13
	(3,3,1)	moving	10	52.4	60.2	62.9	8
LU1	(6,6,6)	static	1	58.2	60.5	63.8	6
	(6,6,6)	moving	1	52.5	60.1	68.0	16
	(6,6,6)	moving	10	54.8	60.0	63.4	8
LU2	(3,3,1)	static	1	59.7	63.8	66.2	5
	(3,3,1)	moving	1	45.7	62.7	66.7	18
	(3,3,1)	moving	10	49.4	62.8	65.7	14
	(3,3,1)	moving	10 (syn.)	50.1	62.8	65.7	14
LI	(3,3,1)	static	1	32.2	32.4	32.7	1
	(3,3,1)	moving	1	31.5	32.4	33.2	3
	(3,3,1)	moving	5	31.8	32.4	32.9	2
	(3,3,1)	moving	10	32.0	32.4	32.8	2

Table 5.3.3: Results for 4D rescanning dose delivery with TULIP. The number of scans is denoted as #s. Results for dose delivery with 1 scan and 10 rescans to a moving tumor are presented. For patient LU2 dose values for rescanning achieved with a synchrotron, denoted as (syn.) are declared.

Pat	machine	spot grid ( $\Delta x, \Delta y, \Delta z$ ) [mm]	$t_{total}$ (10f) [min]	$t_{delivery}$ [min]	$t_{scan}$ [min]	$t_{mag}$ [s]	$t_{energy}$ [min]
LU1	TULIP	(3,3,1)	36.2 (34.0)	31.4	4.5	21	-
LU1	synchr.	(3,3,1)	55.0 (55.0)	29.2	4.5	-	21.3
LU1	TULIP	(6,6,6)	8.2 (3.5)	7.6	0.5	2.1	-
LU2	TULIP	(3,3,1)	26.0 (25.8)	22.2	3.5	17	-
LU2	synchr.	(3,3,1)	60.9 (60.9)	21.9	3.5	-	35.5
LI	TULIP	(3,3,1)	20.3 (20.0)	18.9	1.2	11.0	-
LI	synchr.	(3,3,1)	31.4 (31.4)	18.6	1.2	-	11.6

Table 5.3.4: Irradiation times for 4D rescanning with TULIP and with a common synchrotron (synchr.). Times are given for a single fraction dose delivery and the total irradiation time is given for one fraction of dose delivery in 10 fractions (10f).

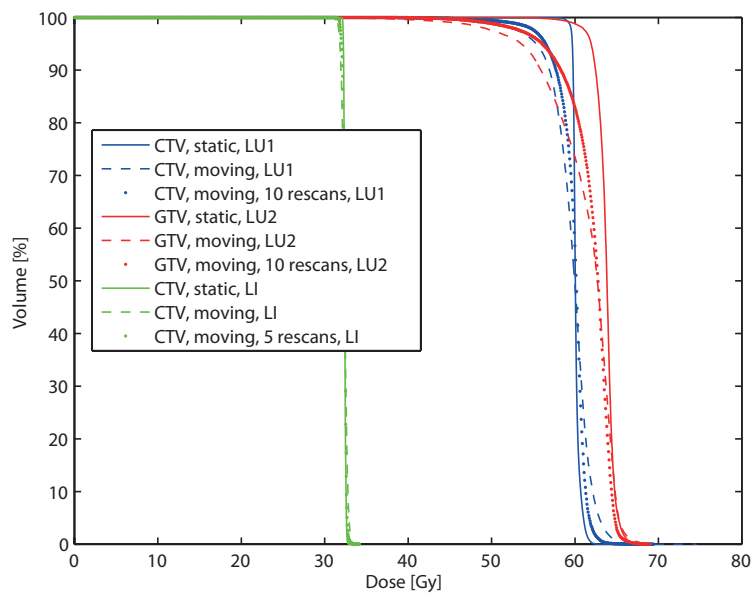


Figure 5.3.4: DVHs for rescanning with TULIP for treatment plans using a small spot grid size  $(\Delta x, \Delta y, \Delta z) = (3, 3, 1)$  mm. 10 rescans for lung patients LU1 and LU2 showed to average out dose distortions caused by organ motion. For the liver patient, the dvh achieved with 5 rescans almost approaches the dvh achieved by static tumor irradiation.

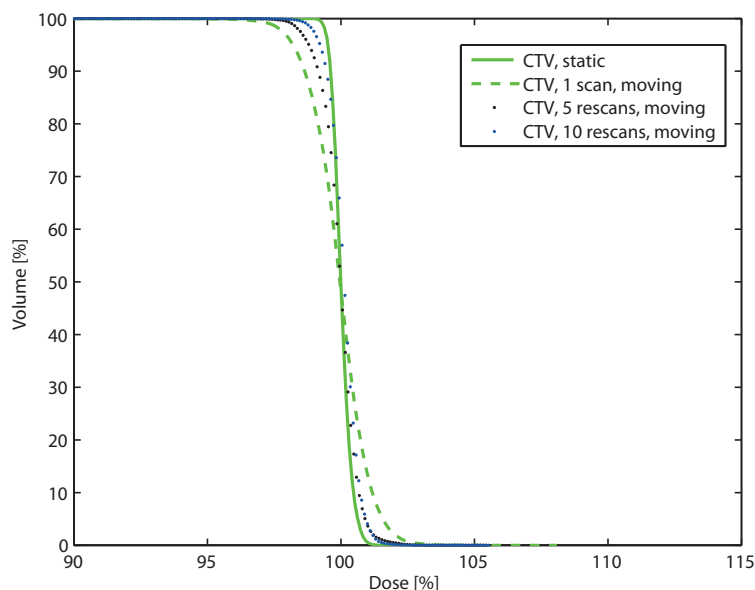


Figure 5.3.5: DVHs for rescanning with TULIP for liver patient LI. The difference in the dose can be seen for 5 and 10 rescans. The dose is normalized, so that 100% correspond to  $D_{50}$  for the irradiation of the static tumor.

## 5.4 Discussion

The results presented in section 5.3.1 reveal the harmful effects of organ and tumor motion during proton irradiation. The difference between lung and liver tumor irradiation in the presence of organ motion is large for the studied cases. While the motion induced effects on the dose distribution were minor for the liver tumor, massive deviations from static tumor irradiation occurred for the lung tumors. The effect of liver motion has also been studied by Zhang et al. [2012] who found dose deviations of up to a maximum of 44.6 % between static liver tumor irradiation and dose delivery to a moving tumor for a single field plan. Mean dose deviations of 2.9 % were observed averaged over different patient cases. In our studied liver case, the motion induced interplay effects were a little smaller. Maximum dose deviations of 22 % could be found. Interestingly, the study of Zhang et al. [2012] reveals the significant impact of the motion registration algorithm used for motion simulation on the dose deviations when comparing static and moving tumors. This agrees with our results. Compared to studies performed prior to this work (data not presented) for the same underlying patient data, but a different algorithm used for CT image registration, we also observed differences, that might also be due to different registration data.

The strong impact of interplay effects on lung tumors has been revealed before.

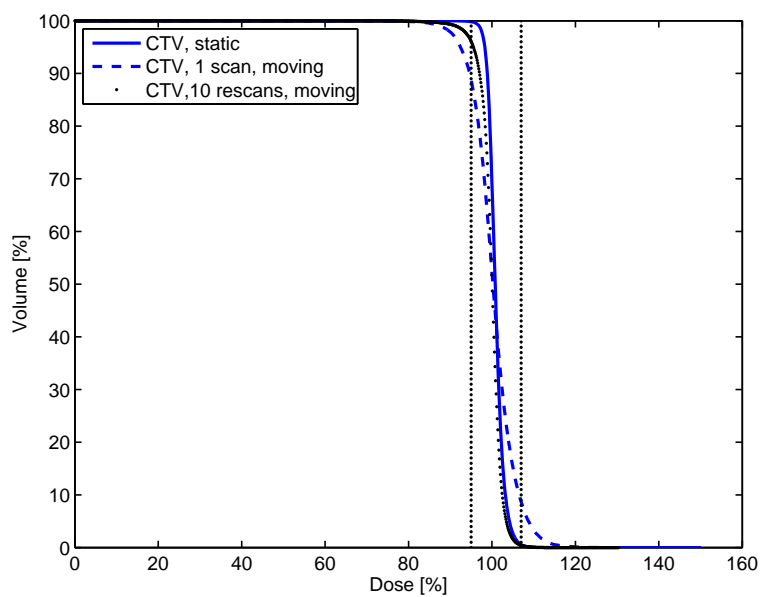


Figure 5.3.6: DVHs for rescaning with TULIP for LU1 using a larger spot grid size  $(\Delta x, \Delta y, \Delta z) = (6, 6, 6)$  mm. 10 rescans improved the dose distribution. However, due to the large spot grid, the clinical requirements, that 100 % of the volume should receive between 95 % and 107 % of the prescribed dose (indicated by black dotted lines), could not be entirely met by rescaning.

[Dowdell et al. \[2013\]](#)) also showed the large influence of tumor motion in the lung on the dose distribution by using 4D Monte Carlo dose calculation. Even though they found a beneficial averaging effect of fractionation on the dose, they also pointed out, that this effect can also be compromised caused by treatment plan settings or specific patient anatomy. Our approach definitely suffers from the use of a pencil beam dose calculation algorithm, which cannot correctly model lateral spread of the dose. This is more evident in very heterogeneous tissues as occur for lung tumors. Particularly at the edges of tumors in very heterogeneous tissues, as is the case for lung tumors, the algorithm might over- or underestimate the dose.

Our results show the severe influence of the extent of tumor motion and the individual patient anatomy on the dose distribution, but also reveal the unpredictability of interplay effects once more ([\[Kraus et al., 2011\]](#), [\[Dowdell et al., 2013\]](#)). Therefore, motion mitigation techniques are mandatory for irradiation of mobile tumors with 3D spot scanning using active energy variation. TULIP offers an improved time structure compared to synchrotrons, that require large time intervals for energy variation.

The results gained for volumetric rescanning of the two lung tumors and the liver tumor indicate the averaging effect of rescanning with respect to dose. Especially, for the liver tumor, where the motion induced dosimetric effects were less pronounced, rescanning improved the dose distribution even further. The resulting dose distribution for 5 rescans almost matched the static tumor irradiation result.

For the lung, rescanning also improved the dose homogeneity. However, the effect of rescanning strongly depends on the spread of the tumor position in the range of motion states during irradiation. Residual detrimental effects on the dose distribution might remain, if the range of motion states covered by the tumor is not sufficient to fully exploit the averaging effect of rescanning. [Mori et al. \[2013a\]](#) also studied rescanning for lung tumors and found volumetric rescanning to have a reliable averaging effect only for more than four rescans. However, this strongly correlates to the specific time structure of the beam delivering devices. Better results even for smaller numbers of rescans were conducted by phase-controlled rescanning [[Furukawa et al., 2010](#)], for which the extraction rate of the accelerator is adjusted and often an additional gating window is defined to ensure dose delivery to a scan volume or layer within a certain time. Using additional gating, however, comes along with an increase of irradiation time. For a conventional synchrotron energy variation requires several seconds and is therefore not preferably suited for volumetric rescanning. This was confirmed by the calculation of energy change time to 11.6 minutes for 93 isoenergy slices and 1.5 s for each energy change. For slow energy changing systems alternative approaches are studied. There are developments described by [Inaniwa et al. \[2012\]](#) to implement a hybrid depth scanning system for carbon ions where the beam of a certain energy produced by a synchrotron is degraded with additional range shifter plates.

However, TULIP offers a real active energy variation together with 3D spot scanning for tumor irradiation on an beneficial time scale. Within several minutes, depending on

the specific treatment plan and tumor size, rescanning with TULIP showed to be feasible. It should be emphasized here, that more sophisticated rescanning techniques such as iso-layered or proportional rescanning [Zenklusen et al., 2010] have the potential to further reduce the irradiation time massively. For example, a reduction of the number of spots by a factor of 2 would almost result in half of the treatment time. Recently, iso-layered rescanning was found to result in improved dose homogeneities and reduced treatment times [Bernatowicz et al., 2013]. Moreover, the influence of the reduced number of proton spots using a wider spot grid was shown. As expected, the homogeneity is harmed by a larger spot distance, however, a huge improvement in irradiation was noticed. For the lung patient, using 6 mm spot distance, dose delivery of one fraction dose with 10 rescans was feasible within 3.5 minutes. Of course, one should mention here, that an increased spot grid size can only lead to acceptable dose distributions, if the spot grid is appropriate for the lateral spot sizes. Therefore, careful adjustment of the grid size to the lateral spot size is required.

For TULIP, the next step will be a combination of beam tracking using a fast 4D feedback system and rescanning, which could average out residual motion induced effects, caused by the delay time of the feedback system. This "rescanning with 4D feedback" will make use of the unique properties of TULIP, which can vary the energy of subsequent spots within milliseconds and thus adjust not only its transverse but also its longitudinal position.



# Chapter 6

## Summary and outlook

Before a general conclusion will be drawn and an outlook presented, the major aspects of this work are summarized here. This thesis is divided into three main parts. The first part contains the technical aspects of the novel accelerator design - TULIP - which constitutes this work (chapter 3). This part is followed by the description of the dose delivery study for static targets with TULIP in chapter 4. The last chapter (5) deals with dose delivery to moving targets.

### **TU**rning **L**inac for **P**roton therapy - TULIP

This work has been carried out as part of the ambitious efforts of the TERA foundation to develop a novel relatively compact proton accelerator for treatment of cancer with proton therapy. In chapter 3 the rational, the technical advances during the development and the current status of the machine design are described. In order to increase the availability of proton therapy, the size and costs of proton accelerators have to be reduced. Therefore, a concept based on a linear accelerator for protons was patented [Amaldi et al., 2008]. It involves a high-frequency linear accelerator for protons mounted on a gantry named TULIP (TUrning LInac for Proton therapy). Protons are preaccelerated to 24 MeV by a cyclotron and then are directed to two subsequent linear accelerator sections. The total length of the accelerator amounts to 11 m. The accelerating sections consist of radio frequency modules that are powered by individual klystrons. The first three modules accelerate the particles to a fixed energy of 70 MeV. Within the remaining modules, the energy can be varied on a milliseconds time scale within a range of 70 to 230 MeV by acting on the klystron input powers. TULIP runs at 3 GHz and provides pulses with a pulse rate of 120 Hz and a maximum number of protons of  $5 \cdot 10^7$  per pulse. In high gradient tests of a prototype gradients of 35 MV/m could be reached. Breakdown rates of  $3 \cdot 10^{-6}$  bpp/m were measured, that correspond to a breakdown every 400 s assuming a length of 10 m. Lateral scanning magnets are included allowing for 3D spot scanning beam delivery.

With the capability to deliver proton spots on a milliseconds time scale, active energy variation and 3D spot scanning, TULIP has the potential of delivering highly conformal dose distributions to static tumors. Furthermore, due to the energy variation on a very short time scale, it might open perspectives for treatment of moving targets. The relatively small size of the accelerator and reduced costs compared to large proton therapy facilities make TULIP a highly competitive single room facility for cancer treatment with protons.

### **Dose delivery to static tumors**

In order to study dose delivery with TULIP, the major part of this work was the development of a software tool, named TuDoCa (TULip DOse CAlculation software) to simulate this process. The software development is described in section 4.1. For dose calculation a pencil-beam algorithm was used and beam specific parameters were included. These comprise the anticipated beam spot sizes and depth dose profiles as well as timing parameters. In a first instance, the gantry was used for proton rotational therapy. Therefore, a dynamic dose delivery process was implemented in the software tool to simulate time dependent rotational dose delivery for various dynamic parameters such as gantry speed, couch motion speed and pulse rate.

After successful validation of the dose calculation algorithm, dose delivery to static tumors by a rotating gantry was simulated (4.2). Two methods were studied. In one approach the gantry stops after predefined angular steps to avoid spots to be delivered too far away from their planned position for a given pulse rate and gantry speed. The second method studied was dose delivery during continuous gantry motion. It has been found that in order to achieve acceptable dose distributions, careful adjustment of dynamic parameters is required. The first approach resulted in good dose distributions, however, from a technical point of view, numerous gantry stops during rotational dose delivery are technically difficult to realize with the required accuracy and might also harm the supporting gantry material. For continuous gantry rotation the parameters for gantry speed and repetition rate found for a realistic patient case were out of the technically feasible range for TULIP. Moreover, when comparing the dosimetric output to results achieved with 3D spot scanning, the dose homogeneity and treatment time was preferable for 3D spot scanning. Altogether, we could not see an advantage of rotational dose delivery with TULIP with regard to time or dose. These findings contributed to the decision to not further pursue rotational dose delivery with TULIP.

After this decision the feasibility of 3D spot scanning dose delivery with TULIP was studied. In the context of this investigation the TULIP specific constraints were put into focus rather than the dosimetric results achieved with this already established delivery method. Therefore, three different patients were selected with a rather complex configuration of tumor and organs at risk. As expected, for all tumors we achieved good target

coverage with 3D spot scanning. Also, for craniospinal irradiation with an extensive target volume, dose calculations using the TULIP treatment field of  $20 \times 20 \text{ cm}^2$  resulted in high quality dose distributions.

Regarding the treatment time, as expected, we found a strong dependence of the irradiation time on the required number of pulses since each pulse requires a delivery time of the inverse of the pulse rate produced by the linear accelerator. However, treatment times were comparable to what is commonly achieved with conventional radiotherapy using either photons or protons. We found irradiation times of 6 minutes for the prostate and 25 minutes for craniospinal irradiation. Moreover, due to the strong dependence of the treatment on the number of pulses and spots, we proposed several methods to reduce the number of proton pulses leading to shorter irradiation times. Concerning the treatment device, the proton source could be modified to allow for more protons per spot or we could even think of using multiple sources. With respect to treatment planning, the spot grid size could be increased to use less spots for the dose delivery, whenever this does not compromise the dose distribution unacceptably. Moreover, Distal Edge Tracking (DET) could be applied, which would certainly reduce the number of proton spots.

Another performance measure is the breakdown rate of the accelerator. For TULIP, measurements of a prototype resulted in a breakdown rate of  $3 \cdot 10^{-5}$  bpp. This would roughly convert to one breakdown within each fraction of dose delivery. This means that, depending on the actual breakdown rate, spots that were planned to be delivered, are left out during irradiation. Therefore, we simulated 3D spot scanning dose delivery assuming various breakdown rates (4.2.3). For almost all breakdown rates and cases no significant influence on the delivered dose was observed. Only for breakdown rates greater than  $10^{-3}$  bpp dose deviations were unacceptable.

In summary, we found that 3D spot scanning with TULIP is feasible and, due to our investigations, superior to rotational dose delivery. Dose can be delivered on a time scale comparable to or shorter than radiation therapy carried out with common existing treatment devices. Further reduction of treatment time could be obtained quite easily either by modifying the proton source or by adaptations of the treatment plan.

### **Dose delivery to moving tumors with TULIP**

Organ motion during radiation therapy, especially with protons and Carbon ions, is still very challenging. Motion mitigation techniques such as rescanning or gating lead to an increase of the treatment times on principle. We consider TULIP to be preferably suited for dose delivery to moving organs due to the very short time scale (milliseconds) at which proton pulses can be delivered. Therefore, we studied TULIP specific dose delivery to moving organs with and without rescanning in chapter 5. As expected and reported also by others, dose delivery with active spot scanning to moving targets

resulted in large dose distortions due to interplay effects between beam and tumor motion. The motion induced dose deviations were larger for the studied lung tumors than for the liver tumor. When rescanning was applied dose deviations were reduced in all cases and confirmed a general beneficial effect of rescanning for irradiation of moving tumors. For the studied liver case, the dose achieved when a static tumor is assumed, could almost be reached. However, reliable conclusions can only be drawn, if more patient cases are studied. With regard to irradiation time, TULIP showed improvement for volumetric rescanning in comparison to dose delivery using a synchrotron, which needs several seconds for each energy change. Dose delivery of a fraction dose in 5 rescans was possible in 20 minutes. As described in the previous paragraph, the irradiation time could possibly be further decreased by modifications to the proton source and more easily by modifications to the treatment plans. The latter case has also been studied in this work. For an increased spot grid of 6 mm we could reduce the total irradiation time of one fraction to 3.5 minutes.

This study has revealed that TULIP is suitable for 3D spot scanning dose delivery for static and moving targets. The combination of active spot scanning on a very short time scale showed to be advantageous compared to other proton accelerator designs. To our knowledge, none of the commercial systems considered in this work can provide active energy variation on such short time scales.

In conclusion, coming back to the initial question of how more patients could profit from proton therapy, our answer is that TULIP can contribute, on a short time scale, to the increase of availability and it opens new perspectives on the treatment of moving tumors with protons.

## **Outlook**

The number of spots and pulses showed to have a significant impact on the dose delivery time. Therefore, more sophisticated rescanning methods, that allow for reduction of the number of spots, should be considered for future investigations. For further investigation, we consider combination of rescanning with an appropriate 4D feedback system and beam tracking. Ten fold rescanning would reduce even more the residual motion induced effects on the dose. Indeed a suitable position detector could provide information of the current motion state during irradiation and thus can be used to pause the beam, whenever the tumor moves outside of a predefined gating window, or send a signal to a 4D feedback system with beam tracking and reduce the residual misdosages by rescanning.





## Bibliography

- Alonso, J. (2011). 562 speaker the dielectric wall accelerator: independent evaluation of project status [1]. *Radiotherapy and Oncology*, 99, Supplement 1:S229–S230.
- Alonso-Basanta, M., Lustig, R. A., and Kennedy, D. W. (2011). Proton beam therapy in skull base pathology. *Otolaryngologic clinics of North America*, 44(5):1173–1183. PMID: 21978900.
- Amaldi, U., Bergesio, D., Bonomi, R., Degiovanni, A., Garlasché, M., Magagnin, P., Verdú-Andrés, S., and Wegner, R. (2012). High-power test results of a 3 GHz single-cell cavity. arXiv e-print 1206.1930.
- Amaldi, U., Berra, P., Crandall, K., Toet, D., Weiss, M., Zennaro, R., Rosso, E., Szeless, B., Vretenar, M., Cicardi, C., De Martinis, C., Giove, D., Davino, D., Masullo, M., and Vaccaro, V. (2004). LIBO—a linac-booster for protontherapy: construction and tests of a prototype. *Nuclear Instruments and Methods in Physics Research Section A: Accelerators, Spectrometers, Detectors and Associated Equipment*, 521(2–3):512–529.
- Amaldi, U., Bonomi, R., Braccini, S., Crescenti, M., Degiovanni, A., Garlasché, M., Garonna, A., Magrin, G., Mellace, C., Pearce, P., Pittà, G., Puggioni, P., Rosso, E., Verdú Andrés, S., Wegner, R., Weiss, M., and Zennaro, R. (2010). Accelerators for hadrontherapy: From lawrence cyclotrons to linacs. *Nuclear Instruments and Methods in Physics Research Section A: Accelerators, Spectrometers, Detectors and Associated Equipment*, 620(2–3):563–577.
- Amaldi, U., Braccini, S., Magrin, G., Pearce, P., and Zennaro, R. (2008). Ion acceleration system for medical and/or other applications.
- Amaldi, U., Braccini, S., and Puggioni, P. (2009). High frequency linacs for hadrontherapy. *Reviews of Accelerator Science and Technology*, 02(01):111–131.
- Amaldi, U. and Grandolfo, M. and Picardi, L. (1996). The RITA network and the design of compact proton accelerators.

- Andres, S. V., Garlasche, M., Bonomi, R., Amaldi, U., Degiovanni, A., and Wegner, R. (2012). 203 the tera high gradient test program for hadron therapy linacs. *Radiotherapy and Oncology*, 102, Supplement 1:S99–S100.
- Baroni, G., Ferrigno, G., Orecchia, R., and Pedotti, A. (2000). Real-time three-dimensional motion analysis for patient positioning verification. *Radiotherapy and Oncology*, 54(1):21–27.
- Bernatowicz, K., Lomax, A. J., and Knopf, A. (2013). Comparative study of layered and volumetric rescanning for different scanning speeds of proton beam in liver patients. *Physics in medicine and biology*, 58(22):7905–7920. PMID: 24165090.
- Bert, C. and Durante, M. (2011). Motion in radiotherapy: particle therapy. *Physics in Medicine and Biology*, 56(16):R113.
- Bert, C., Gemmel, A., Saito, N., Chaudhri, N., Schardt, D., Durante, M., Kraft, G., and Rietzel, E. (2010). Dosimetric precision of an ion beam tracking system. *Radiation oncology (London, England)*, 5:61. PMID: 20591160.
- Bert, C., Groezinger, S. O., and Rietzel, E. (2008). Quantification of interplay effects of scanned particle beams and moving targets. *Physics in Medicine and Biology*, 53(9):2253–2265.
- Bert, C. and Rietzel, E. (2007). 4D treatment planning for scanned ion beams. *Radiation Oncology*, 2(1):24.
- Bert, C., Saito, N., Schmidt, A., Chaudhri, N., Schardt, D., and Rietzel, E. (2007). Target motion tracking with a scanned particle beam. *Medical physics*, 34(12):4768–4771. PMID: 18196804.
- Bethe, H. A. (1953). Molière's theory of multiple scattering. *Physical Review*, 89(6):1256. Copyright (C) 2010 The American Physical Society.
- Blattmann, H. and Coray, A. (1990). A horizontal proton beam line for the development of a scanning technique. *Radiotherapy and Oncology*, 17(1):17–20.
- Bortfeld, T., Jiang, S. B., and Rietzel, E. (2004). Effects of motion on the total dose distribution. *Seminars in Radiation Oncology*, 14(1):41–51.
- Bortfeld, T., Jokivarsi, K., Goitein, M., Kung, J., and Jiang, S. B. (2002). Effects of intra-fraction motion on IMRT dose delivery: statistical analysis and simulation. *Physics in Medicine and Biology*, 47(13):2203–2220.
- Bragg, W. H. (1904). On the absorption of alpha rays, and on the classification of the alpha rays from radium. *Philosophical Magazine*, 6(8):719–725.

- Britton, K. R., Starkschall, G., Tucker, S. L., Pan, T., Nelson, C., Chang, J. Y., Cox, J. D., Mohan, R., and Komaki, R. (2007). Assessment of gross tumor volume regression and motion changes during radiotherapy for non-small-cell lung cancer as measured by four-dimensional computed tomography. *International journal of radiation oncology, biology, physics*, 68(4):1036–1046. PMID: 17379442.
- Calypso Medical (2011). Calypso Medical Installs System into World's Largest Proton Facility at University of Pennsylvania. Press release.
- Caporaso, G. (2011). Science and technology review (S&TR) | October/November 2011: Weapons diagnostics technology revolutionizes cancer treatment. <https://str.llnl.gov/OctNov11/caporaso.html>.
- Caporaso, G. J., Chen, Y.-J., and Sampayan, S. E. (2009). The dielectric wall accelerator. *Reviews of Accelerator Science and Technology*, 02(01):253–263.
- Caporaso, G. J., Mackie, T. R., Sampayan, S., Chen, Y.-J., Blackfield, D., Harris, J., Hawkins, S., Holmes, C., Nelson, S., Paul, A., Poole, B., Rhodes, M., Sanders, D., Sullivan, J., Wang, L., Watson, J., Reckwerdt, P. J., Schmidt, R., Pearson, D., Flynn, R. W., Matthews, D., and Purdy, J. (2008). A compact linac for intensity modulated proton therapy based on a dielectric wall accelerator. *Physica medica*, 24(2):98–101. PMID: 18430600.
- Casiraghi, M., Albertini, F., and Lomax, A. J. (2013). Advantages and limitations of the 'worst case scenario' approach in IMPT treatment planning. *Physics in medicine and biology*, 58(5):1323–1339. PMID: 23391569.
- Chaudhri, N., Saito, N., Bert, C., Franczak, B., Steidl, P., Durante, M., Rietzel, E., and Schardt, D. (2010). Ion-optical studies for a range adaptation method in ion beam therapy using a static wedge degrader combined with magnetic beam deflection. *Physics in Medicine and Biology*, 55(12):3499.
- Chu, W. T., Ludewigt, B. A., and Renner, T. R. (1993). Instrumentation for treatment of cancer using proton and light-ion beams. *Review of Scientific Instruments*, 64(8):2055–2122.
- Combs, S. E. and Debus, J. (2013). Treatment with heavy charged particles: Systematic review of clinical data and current clinical (comparative) trials. *Acta oncologica (Stockholm, Sweden)*. PMID: 23964656.
- Combs, S. E., Laperriere, N., and Brada, M. (2013). Clinical controversies: proton radiation therapy for brain and skull base tumors. *Seminars in radiation oncology*, 23(2):120–126. PMID: 23473689.

- CPAC (2013). CPAC - compact particle acceleration corporation. <http://www.cpac.pro/>.
- Degiovanni, A., Amaldi, U., Bonomi, R., Garlasché, M., Garonna, A., Verdú-Andrés, S., and Wegner, R. (2011). TERA high gradient test program of RF cavities for medical linear accelerators. *Nuclear Instruments and Methods in Physics Research Section A: Accelerators, Spectrometers, Detectors and Associated Equipment*, 657(1):55–58.
- DeLaney, T. F. (2011). Proton therapy in the clinic. *Frontiers of radiation therapy and oncology*, 43:465–485. PMID: 21625169.
- Dowdell, S., Grassberger, C., Sharp, G. C., and Paganetti, H. (2013). Interplay effects in proton scanning for lung: a 4D monte carlo study assessing the impact of tumor and beam delivery parameters. *Physics in medicine and biology*, 58(12):4137–4156. PMID: 23689035.
- Engelsman, M. and Kooy, H. M. (2005). Target volume dose considerations in proton beam treatment planning for lung tumors. *Medical physics*, 32(12):3549–3557. PMID: 16475753.
- Flynn, R. T., Barbee, D. L., Mackie, T. R., and Jeraj, R. (2007). Comparison of intensity modulated x-ray therapy and intensity modulated proton therapy for selective subvolume boosting: a phantom study. *Physics in medicine and biology*, 52(20):6073–6091. PMID: 17921573 PMID: PMC2712448.
- Fokdal, L., Honoré, H., Høyer, M., Meldgaard, P., Fode, K., and von der Maase, H. (2004). Impact of changes in bladder and rectal filling volume on organ motion and dose distribution of the bladder in radiotherapy for urinary bladder cancer. *International Journal of Radiation Oncology\*Biophysics*, 59(2):436–444.
- Fourrier, J., Mandrillon, P., Mandrillon, J., Meot, F., Pasternak, J., and Conjat, M. (2008). Variable energy protontherapy FFAG accelerator. In *Conf.Proc.*, volume C0806233, page TUPP115.
- Fredriksson, A. (2012). A characterization of robust radiation therapy treatment planning methods-from expected value to worst case optimization. *Medical physics*, 39(8):5169–5181. PMID: 22894442.
- Furukawa, T., Inaniwa, T., Sato, S., Shirai, T., Mori, S., Takeshita, E., Mizushima, K., Himukai, T., and Noda, K. (2010). Moving target irradiation with fast rescanning and gating in particle therapy. *Medical Physics*, 37(9):4874–4879. PMID: 20964205.

- Furukawa, T., Inaniwa, T., Sato, S., Tomitani, T., Minohara, S., Noda, K., and Kanai, T. (2007). Design study of a raster scanning system for moving target irradiation in heavy-ion radiotherapy. *Medical Physics*, 34(3):1085–1097.
- Goitein, M., Lomax, A. J., and Pedroni, E. S. (2002). Treating cancer with protons. *Physics Today*, 55(9):45–50.
- Gottschalk, B., Koehler, A., Schneider, R., Sisterson, J., and Wagner, M. (1993). Multiple coulomb scattering of 160 MeV protons. *Nuclear Instruments and Methods in Physics Research Section B: Beam Interactions with Materials and Atoms*, 74(4):467–490.
- Grudiev, A., Calatroni, S., and Wuensch, W. (2009). New local field quantity describing the high gradient limit of accelerating structures. *Physical Review Special Topics - Accelerators and Beams*, 12(10):102001.
- Grözinger, S. O., Li, Q., Rietzel, E., Haberer, T., and Kraft, G. (2004). 3D online compensation of target motion with scanned particle beam. *Radiotherapy and oncology: journal of the European Society for Therapeutic Radiology and Oncology*, 73 Suppl 2:S77–79. PMID: 15971315.
- Haberer, T., Becher, W., Schardt, D., and Kraft, G. (1993). Magnetic scanning system for heavy ion therapy. *Nuclear Instruments and Methods in Physics Research Section A: Accelerators, Spectrometers, Detectors and Associated Equipment*, 330(1–2):296–305.
- Habermehl, D., Debus, J., Ganten, T., Ganten, M.-K., Bauer, J., Brecht, I. C., Brons, S., Haberer, T., Haertig, M., Jäkel, O., Parodi, K., Welzel, T., and Combs, S. E. (2013). Hypofractionated carbon ion therapy delivered with scanned ion beams for patients with hepatocellular carcinoma – feasibility and clinical response. *Radiation Oncology*, 8(1):59. PMID: 23497349.
- Hamm, R., Crandall, K. R., and Potter, J. (1991). Preliminary design of a dedicated proton therapy linac. In , *Conference Record of the 1991 IEEE Particle Accelerator Conference, 1991. Accelerator Science and Technology*, pages 2583–2585 vol.4.
- Hanley, J., Debois, M. M., Mah, D., Mageras, G. S., Raben, A., Rosenzweig, K., Mychalczak, B., Schwartz, L. H., Gloeggler, P. J., Lutz, W., Ling, C., Leibel, S. A., Fuks, Z., and Kutcher, G. J. (1999). Deep inspiration breath-hold technique for lung tumors: the potential value of target immobilization and reduced lung density in dose escalation. *International Journal of Radiation Oncology\*Biophysics*, 45(3):603–611.

- Harris, E. J., Miller, N. R., Bamber, J. C., Symonds-Taylor, J. R. N., and Evans, P. M. (2010). Speckle tracking in a phantom and feature-based tracking in liver in the presence of respiratory motion using 4D ultrasound. *Physics in Medicine and Biology*, 55(12):3363.
- Hill-Kayser, C. E., Both, S., and Tochner, Z. (2011). Proton therapy: Ever shifting sands and the opportunities and obligations within. *Frontiers in oncology*, 1:24. PMID: 22655235.
- Hong, L., Goitein, M., Bucciolini, M., Comiskey, R., Gottschalk, B., Rosenthal, S., Serago, C., and Urie, M. (1996). A pencil beam algorithm for proton dose calculations. *Physics in medicine and biology*, 41(8):1305–1330. PMID: 8858722.
- Hoppe, B., Henderson, R., Mendenhall, W. M., Nichols, R. C., Li, Z., and Mendenhall, N. P. (2011). Proton therapy for prostate cancer. *Oncology (Williston Park, N.Y.)*, 25(7):644–650, 652. PMID: 21888265.
- Hui, Z., Zhang, X., Starkschall, G., Li, Y., Mohan, R., Komaki, R., Cox, J. D., and Chang, J. Y. (2008). Effects of interfractional motion and anatomic changes on proton therapy dose distribution in lung cancer. *International Journal of Radiation Oncology\*Biography\*Physics*, 72(5):1385–1395.
- IBA, Proton Therapy (2012). ProteusONE, proton therapy. <http://www.iba-protontherapy.com/>.
- ICRU (International Commission on Radiation Units & Measurements) (1999a). ICRU report 50, prescribing, recording, and reporting photon beam therapy.
- ICRU (International Commission on Radiation Units & Measurements) (1999b). ICRU report 62, prescribing, recording, and reporting photon beam therapy.
- ICRU (International Commission on Radiation Units & Measurements) (2007). ICRU report 78, prescribing, recording, and reporting photon beam therapy.
- ICRU (International Commission on Radiation Units & Measurements) (2010). ICRU report 83, prescribing, recording, and reporting intensity-modulated photon-beam therapy.
- Inaniwa, T., Furukawa, T., Kanematsu, N., Mori, S., Mizushima, K., Sato, S., Toshito, T., Shirai, T., and Noda, K. (2012). Evaluation of hybrid depth scanning for carbon-ion radiotherapy. *Medical physics*, 39(5):2820–2825. PMID: 22559653.
- International Electrotechnical Commission (1999). Radiotherapy equipment - coordinates, movements & scales, may 1995.

- Iwata, Y., Kadowaki, T., Uchiyama, H., Fujimoto, T., Takada, E., Shirai, T., Furukawa, T., Mizushima, K., Takeshita, E., Katagiri, K., Sato, S., Sano, Y., and Noda, K. (2010). Multiple-energy operation with extended flattops at HIMAC. *Nuclear Instruments and Methods in Physics Research Section A: Accelerators, Spectrometers, Detectors and Associated Equipment*, 624(1):33–38.
- Jäkel, O. (2006). Ranges of ions in metals for use in particle treatment planning. *Physics in Medicine and Biology*, 51(9):N173.
- Jäkel, O., Combs, S., Bert, C., and Richter, D. (2013). Patient data by courtesy of Heavy Ion Therapy Center HIT (Heidelberg) and Gesellschaft für Schwerionenforschung GSI (Darmstadt).
- Jongen, Y., Abs, M., Blondin, A., Kleeven, W., Zaremba, S., Vandeplassche, D., Aleksandrov, V., Gursky, S., Karamyshev, O., Karamysheva, G., Kazarinov, N., Kostromin, S., Morozov, N., Samsonov, E., Shirkov, G., Shevtsov, V., Syresin, E., and Tuzikov, A. (2010). Compact superconducting cyclotron c400 for hadron therapy. *Nuclear Instruments and Methods in Physics Research Section A: Accelerators, Spectrometers, Detectors and Associated Equipment*, 624(1):47–53.
- Kanai, T., Endo, M., Minohara, S., Miyahara, N., Koyama-ito, H., Tomura, H., Matsufuji, N., Futami, Y., Fukumura, A., Hiraoka, T., Furusawa, Y., Ando, K., Suzuki, M., Soga, F., and Kawachi, K. (1999). Biophysical characteristics of HIMAC clinical irradiation system for heavy-ion radiation therapy. *International journal of radiation oncology, biology, physics*, 44(1):201–210. PMID: 10219815.
- Kanai, T., Matsufuji, N., Miyamoto, T., Mizoe, J., Kamada, T., Tsuji, H., Kato, H., Baba, M., and Tsujii, H. (2006). Examination of GyE system for HIMAC carbon therapy. *International journal of radiation oncology, biology, physics*, 64(2):650–656. PMID: 16414376.
- Keall, P. J., Kini, V. R., Vedam, S. S., and Mohan, R. (2001). Motion adaptive x-ray therapy: a feasibility study. *Physics in Medicine and Biology*, 46(1):1–10.
- Kilpatrick, W. D. (1957). Criterion for vacuum sparking designed to include both rf and dc. *Review of Scientific Instruments*, 28(10):824–826.
- Klein, H.-U., Baumgarten, C., Geisler, A., Heese, J., Hobl, A., Krischel, D., Schillo, M., Schmidt, S., and Timmer, J. (2005). New superconducting cyclotron driven scanning proton therapy systems. *Nuclear Instruments and Methods in Physics Research Section B: Beam Interactions with Materials and Atoms*, 241(1–4):721–726.

- Knopf, A.-C., Boye, D., Lomax, A., and Mori, S. (2013). Adequate margin definition for scanned particle therapy in the incidence of intrafractional motion. *Physics in medicine and biology*, 58(17):6079–6094. PMID: 23939146.
- Knopf, A.-C., Hong, T. S., and Lomax, A. (2011). Scanned proton radiotherapy for mobile targets-the effectiveness of re-scanning in the context of different treatment planning approaches and for different motion characteristics. *Physics in medicine and biology*, 56(22):7257–7271. PMID: 22037710.
- Kraus, K. M., Heath, E., and Oelfke, U. (2011). Dosimetric consequences of tumour motion due to respiration for a scanned proton beam. *Physics in medicine and biology*, 56(20):6563–6581. PMID: 21937770.
- Krause, S., Beck, S., Schubert, K., Lissner, S., Hui, S., Herfarth, K., Debus, J., and Sterzing, F. (2012). Accelerated large volume irradiation with dynamic Jaw/Dynamic couch helical tomotherapy. *Radiation oncology (London, England)*, 7:191. PMID: 23146914.
- Kupelian, P., Willoughby, T., Mahadevan, A., Djemil, T., Weinstein, G., Jani, S., Enke, C., Solberg, T., Flores, N., Liu, D., Beyer, D., and Levine, L. (2007). Multi-institutional clinical experience with the calypso system in localization and continuous, real-time monitoring of the prostate gland during external radiotherapy. *International Journal of Radiation Oncology\*Biography\*Physics*, 67(4):1088–1098.
- Legendijk, J. J., Raaymakers, B. W., Raaijmakers, A. J., Overweg, J., Brown, K. J., Kerkhof, E. M., Put, R. W. v. d., Hårdemark, B., Vulpen, M. v., and Heide, U. A. v. d. (2008). MRI/linac integration. *Radiotherapy and Oncology*, 86(1):25–29.
- Lambert, J., Suchowerska, N., McKenzie, D. R., and Jackson, M. (2005). Intrafractional motion during proton beam scanning. *Physics in Medicine and Biology*, 50(20):4853–4862.
- Langen, K. M. and Jones, D. T. L. (2001). Organ motion and its management. *International Journal of Radiation Oncology\*Biography\*Physics*, 50(1):265–278.
- Lattanzi, J., McNeeley, S., Pinover, W., Horwitz, E., Das, I., Schultheiss, T. E., and Hanks, G. E. (1999). A comparison of daily CT localization to a daily ultrasound-based system in prostate cancer. *International Journal of Radiation Oncology\*Biography\*Physics*, 43(4):719–725.
- Lennox, A. J. (1989). Hospital-based proton linear accelerator for particle therapy and radioisotope production. *Nuclear Instruments and Methods in Physics Research Section B: Beam Interactions with Materials and Atoms*, pages 1197–1200.

- Leo, W. R. (1994). *Techniques for Nuclear and Particle Physics Experiments: A How-To Approach*. Springer.
- Lomax, A. (1999). Intensity modulation methods for proton radiotherapy. *Physics in Medicine and Biology*, 44(1):185–205.
- Mackie, T. R., Holmes, T., Swerdloff, S., Reckwerdt, P., Deasy, J. O., Yang, J., Paliwal, B., and Kinsella, T. (1993). Tomotherapy: a new concept for the delivery of dynamic conformal radiotherapy. *Medical physics*, 20(6):1709–1719. PMID: 8309444.
- Maughan, R. L., Powers, W. E., and Blosser, H. G. (1994). A superconducting cyclotron for neutron radiation therapy. *Medical Physics*, 21(6):779–785.
- Mayahara, H., Murakami, M., Kagawa, K., Kawaguchi, A., Oda, Y., Miyawaki, D., Sasaki, R., Sugimura, K., and Hishikawa, Y. (2007). Acute morbidity of proton therapy for prostate cancer: The hyogo ion beam medical center experience. *International Journal of Radiation Oncology\*Biological\*Physics*, 69(2):434–443.
- Merchant, T. E. (2013). Clinical controversies: proton therapy for pediatric tumors. *Seminars in radiation oncology*, 23(2):97–108. PMID: 23473686.
- Mevion Medical Systems (2012). Compact proton accelerator hits 250 MeV - Medical-PhysicsWeb. <http://medicalphysicsweb.org/cws/article/research/42731>. Still River Systems achieves clinical beam extraction from its compact proton accelerator.
- Minohara, S., Kanai, T., Endo, M., Noda, K., and Kanazawa, M. (2000). Respiratory gated irradiation system for heavy-ion radiotherapy\*1. *International Journal of Radiation Oncology\*Biological\*Physics*, 47(4):1097–1103.
- Mohan, R. and Bortfeld, T. (2011). Proton therapy: clinical gains through current and future treatment programs. *Frontiers of radiation therapy and oncology*, 43:440–464. PMID: 21625168.
- Molière, G. (1948). Theorie der Streuung schneller geladener Teilchen II. Mehrfach- und Vielfachstreuung. *Zeitschrift für Naturforschung Teil A*, 3:78–97.
- Mori, S., Furukawa, T., Inaniwa, T., Zenklusen, S., Nakao, M., Shirai, T., and Noda, K. (2013a). Systematic evaluation of four-dimensional hybrid depth scanning for carbon-ion lung therapy. *Medical physics*, 40(3):031720. PMID: 23464315.
- Mori, S., Inaniwa, T., Furukawa, T., Zenklusen, S., Shirai, T., and Noda, K. (2013b). Effects of a difference in respiratory cycle between treatment planning and irradiation for phase-controlled rescanning and carbon pencil beam scanning. *The British journal of radiology*, 86(1028):20130163. PMID: 23833034.

- Mori, S., Lu, H.-M., Wolfgang, J. A., Choi, N. C., and Chen, G. T. Y. (2009). Effects of interfractional anatomical changes on water-equivalent pathlength in charged-particle radiotherapy of lung cancer. *Journal of radiation research*, 50(6):513–519. PMID: 19959880.
- Negoro, Y., Nagata, Y., Aoki, T., Mizowaki, T., Araki, N., Takayama, K., Kokubo, M., Yano, S., Koga, S., Sasai, K., Shibamoto, Y., and Hiraoka, M. (2001). The effectiveness of an immobilization device in conformal radiotherapy for lung tumor: reduction of respiratory tumor movement and evaluation of the daily setup accuracy. *International Journal of Radiation Oncology\*Biography\*Physics*, 50(4):889–898.
- Nihei, K., Ogino, T., Ishikura, S., Kawashima, M., Nishimura, H., Arahira, S., and Onozawa, M. (2005). Phase II feasibility study of high-dose radiotherapy for prostate cancer using proton boost therapy: first clinical trial of proton beam therapy for prostate cancer in japan. *Japanese journal of clinical oncology*, 35(12):745–752. PMID: 16314345.
- Nill, S., Bortfeld, T., and Oelfke, U. (2004). Inverse planning of intensity modulated proton therapy. *Zeitschrift für medizinische Physik*, 14(1):35–40. PMID: 15104008.
- Nioutsikou, E., Seppenwoolde, Y., Symonds-Taylor, J. R. N., Heijmen, B., Evans, P., and Webb, S. (2008). Dosimetric investigation of lung tumor motion compensation with a robotic respiratory tracking system: an experimental study. *Medical physics*, 35(4):1232–1240. PMID: 18491515.
- Nordlund, K. and Djurabekova, F. (2012). Defect model for the dependence of breakdown rate on external electric fields. *Physical Review Special Topics - Accelerators and Beams*, 15(7):071002.
- Oelfke, U. and Bortfeld, T. (2003). Optimization of physical dose distributions with hadron beams: comparing photon IMRT with IMPT. *Technology in Cancer Research & Treatment*, 2(5):401–412.
- Ohara, K., Okumura, T., Akisada, M., Inada, T., Mori, T., Yokota, H., and Calaguas, M. J. (1989). Irradiation synchronized with respiration gate. *International Journal of Radiation Oncology\*Biography\*Physics*, 17(4):853–857.
- Paganetti, H. (2012). *Proton therapy physics*. Series in Medical Physics and Biomedical Engineering. CRC Press, Taylor and Francis Group, Boca Raton, Fla.
- Park, P. C., Cheung, J. P., Zhu, X. R., Lee, A. K., Sahoo, N., Tucker, S. L., Liu, W., Li, H., Mohan, R., Court, L. E., and Dong, L. (2013). Statistical assessment of proton treatment plans under setup and range uncertainties. *International journal of radiation oncology, biology, physics*, 86(5):1007–1013. PMID: 23688812.

- Park, P. C., Zhu, X. R., Lee, A. K., Sahoo, N., Melancon, A. D., Zhang, L., and Dong, L. (2012). A beam-specific planning target volume (PTV) design for proton therapy to account for setup and range uncertainties. *International journal of radiation oncology, biology, physics*, 82(2):e329–336. PMID: 21703781.
- Pedroni, E., Bacher, R., Blattmann, H., Böhringer, T., Coray, A., Lomax, A., Lin, S., Munkel, G., Scheib, S., and Schneider, U. (1995). The 200-MeV proton therapy project at the Paul Scherrer Institute: conceptual design and practical realization. *Medical Physics*, 22(1):37–53.
- Pedroni, E., Bearpark, R., Böhringer, T., Coray, A., Dupich, J., Forss, S., George, D., Grossmann, M., Goitein, G., Hilbes, C., Jermann, M., Lin, S., Lomax, A., Negrazus, M., Schippers, M., and Kotle, G. (2004). The PSI gantry 2: a second generation proton scanning gantry. *Zeitschrift für medizinische Physik*, 14(1):25–34. PMID: 15104007.
- Peggs, S and Barton, D (2002). The rapid cycling medical synchrotron. In *Proceedings of the European Particle Accelerator Conference*, pages 2754–6.
- Phillips, M. H., Pedroni, E., Blattmann, H., Boehringer, T., Coray, A., and Scheib, S. (1992). Effects of respiratory motion on dose uniformity with a charged particle scanning method. *Physics in Medicine and Biology*, 37(1):223–233.
- Picardi, L., Bartolini, R., Silvestrov, G. I., Ronsivalle, C., Vsevolozskhaya, T., and Vignati, A. (1994). Preliminary design of a very compact protosynchrotron for proton therapy.
- Protom International, Inc. (2013). Protom - proton therapy technologies. <http://www.protominternational.com/>.
- PTCOG, Patientstatistics (2013). Particle Therapy Co-Operative Group (PTCOG). Hadron Therapy Patient Statistics. <http://ptcog.web.psi.ch/>.
- Raaymakers, B. W., Raaijmakers, A. J. E., and Lagendijk, J. J. W. (2008). Feasibility of MRI guided proton therapy: magnetic field dose effects. *Physics in medicine and biology*, 53(20):5615–5622. PMID: 18799829.
- Rechner, L. A., Howell, R. M., Zhang, R., Etzel, C., Lee, A. K., and Newhauser, W. D. (2012). Risk of radiogenic second cancers following volumetric modulated arc therapy and proton arc therapy for prostate cancer. *Physics in medicine and biology*, 57(21):7117–7132. PMID: 23051714.
- Riboldi, M., Orecchia, R., and Baroni, G. (2012). Real-time tumour tracking in particle therapy: technological developments and future perspectives. *The lancet oncology*, 13(9):e383–391. PMID: 22935238.

- Robinson, A. P. L., Zepf, M., Kar, S., Evans, R. G., and Bellei, C. (2008). Radiation pressure acceleration of thin foils with circularly polarized laser pulses. *New Journal of Physics*, 10(1):013021.
- Saito, N., Bert, C., Chaudhri, N., Gemmel, A., Schardt, D., Durante, M., and Rietzel, E. (2009). Speed and accuracy of a beam tracking system for treatment of moving targets with scanned ion beams. *Physics in Medicine and Biology*, 54(16):4849.
- Sampayan, S. E., Caporaso, G. J., and Kirbie, H. C. (1998). Enhanced dielectric-wall linear accelerator. CIB: H05H7/00; H05H9/00; (IPC1-7): H05H9/00.
- Sandison, G. A., Papiez, E., Bloch, C., and Morphis, J. (1997). Phantom assessment of lung dose from proton arc therapy. *International journal of radiation oncology, biology, physics*, 38(4):891–897. PMID: 9240659.
- Schell, S. and Wilkens, J. J. (2012). Dosimetric effects of energy spectrum uncertainties in radiation therapy with laser-driven particle beams. *Physics in Medicine and Biology*, 57(5):N47.
- Schillo, M., Geisler, A., Hobl, A., Klein, H. U., Krischel, D., Meyer-Reumers, M., Piel, C., Blosser, H., Kim, J.-W., Marti, F., Vincent, J., Brandenburg, S., and Beijers, J. P. M. (2001). Compact superconducting 250 MeV proton cyclotron for the PSI PROSCAN proton therapy project. *AIP Conference Proceedings*, 600:37–39.
- Schippers, J. M. (2009). Beam delivery systems for particle radiation therapy: Current status and recent developments. *Reviews of Accelerator Science and Technology*, 02(01):179–200.
- Schippers, J. M. and Lomax, A. J. (2011). Emerging technologies in proton therapy. *Acta oncologica (Stockholm, Sweden)*, 50(6):838–850. PMID: 21767183.
- Schlegel, W. and Bille, J. (2001). *Medizinische Physik*, volume 2. Springer, Berlin.
- Schlegel, W. and Mahr, A. (2007). *Multimedia DVD, 3D Conformal Radiation Therapy - A multimedia introduction to methods and techniques 2nd revised and enhanced edition*. Springer Verlag Berlin Heidelberg New York.
- Scholz, M. and Kraft, G. (1994). Calculation of heavy ion inactivation probabilities based on track structure, x ray sensitivity and target size. *Radiation Protection Dosimetry*, 52(1-4):29–33.
- Scholz, M. and Kraft, G. (1996). Track structure and the calculation of biological effects of heavy charged particles. *Advances in Space Research*, 18(1–2):5–14.

- Seco, J., Robertson, D., Trofimov, A., and Paganetti, H. (2009). Breathing interplay effects during proton beam scanning: simulation and statistical analysis. *Physics in Medicine and Biology*, 54(14):N283.
- Seiler, P. G., Blattmann, H., Kirsch, S., Muench, R. K., and Schilling, C. (2000). A novel tracking technique for the continuous precise measurement of tumour positions in conformal radiotherapy. *Physics in medicine and biology*, 45(9):N103–110. PMID: 11008969.
- Sengbusch, E., Pérez-Andújar, A., DeLuca, P M, J., and Mackie, T. R. (2009). Maximum proton kinetic energy and patient-generated neutron fluence considerations in proton beam arc delivery radiation therapy. *Medical physics*, 36(2):364–372. PMID: 19291975.
- Seppenwoolde, Y., Shirato, H., Kitamura, K., Shimizu, S., van Herk, M., Lebesque, J. V., and Miyasaka, K. (2002). Precise and real-time measurement of 3D tumor motion in lung due to breathing and heartbeat, measured during radiotherapy. *International Journal of Radiation Oncology\*Biological\*Physics*, 53(4):822–834.
- Shah, A. P., Kupelian, P. A., Waghorn, B. J., Willoughby, T. R., Rineer, J. M., Mañon, R. R., Vollenweider, M. A., and Meeks, S. L. (2013). Real-time tumor tracking in the lung using an electromagnetic tracking system. *International journal of radiation oncology, biology, physics*, 86(3):477–483. PMID: 23523325.
- Shirato, H., Harada, T., Harabayashi, T., Hida, K., Endo, H., Kitamura, K., Onimaru, R., Yamazaki, K., Kurauchi, N., Shimizu, T., Shinohara, N., Matsushita, M., Dosaka-Akita, H., and Miyasaka, K. (2003). Feasibility of insertion/implantation of 2.0-mm-diameter gold internal fiducial markers for precise setup and real-time tumor tracking in radiotherapy. *International journal of radiation oncology, biology, physics*, 56(1):240–247. PMID: 12694845.
- Shirato, H., Seppenwoolde, Y., Kitamura, K., Onimura, R., and Shimizu, S. (2004). Intrafractional tumor motion: lung and liver. *Seminars in Radiation Oncology*, 14(1):10–18. PMID: 14752729.
- Siddon, R. L. (1985). Fast calculation of the exact radiological path for a three-dimensional CT array. *Medical Physics*, 12(2):252–255.
- Smeenk, R. J., Teh, B. S., Butler, E. B., van Lin, E. N., and Kaanders, J. H. (2010). Is there a role for endorectal balloons in prostate radiotherapy? a systematic review. *Radiotherapy and Oncology*, 95(3):277–282.
- Smith, A. R. (2009). Vision 20/20: proton therapy. *Medical physics*, 36(2):556–568. PMID: 19291995.

- Sonke, J., Lebesque, J., and Herk, M. v. (2008). Variability of four-dimensional computed tomography patient models. *International Journal of Radiation Oncology, Biology, Physics*, 70(2):590–598.
- Steiner, E., Georg, D., Goldner, G., and Stock, M. (2013). Prostate and patient intrafraction motion: Impact on treatment time-dependent planning margins for patients with endorectal balloon. *International Journal of Radiation Oncology\*Biology\*Physics*, 86(4):755–761.
- Sterzing, F., Schubert, K., Sroka-Perez, G., Kalz, J., Debus, J., and Herfarth, K. (2008). Helical tomotherapy. experiences of the first 150 patients in heidelberg. *Strahlentherapie und Onkologie: Organ der Deutschen Röntgengesellschaft ... [et al]*, 184(1):8–14. PMID: 18188517.
- Stroom, J. C., Koper, P. C., Korevaar, G. A., van Os, M., Janssen, M., de Boer, H. C., Levendag, P. C., and Heijmen, B. J. (1999). Internal organ motion in prostate cancer patients treated in prone and supine treatment position. *Radiotherapy and Oncology*, 51(3):237–248.
- Takahashi, K., Purdy, J. A., and Liu, Y. Y. (1983). Work in progress: treatment planning system for conformation radiotherapy. *Radiology*, 147(2):567–573. PMID: 6403972.
- Timmermann, B., Lomax, A. J., Nobile, L., Grotzer, M. A., Weiss, M., Kortmann, R.-D., Bolsi, A., and Goitein, G. (2007). Novel technique of craniospinal axis proton therapy with the spot-scanning system: avoidance of patching multiple fields and optimized ventral dose distribution. *Strahlentherapie und Onkologie: Organ der Deutschen Röntgengesellschaft ... [et al]*, 183(12):685–688. PMID: 18040613.
- Tobias, C. A., Lawrence, J. H., Born, J. L., McCombs, R. K., Roberts, J. E., Anger, H. O., Low-Beer, B. V. A., and Huggins, C. B. (1958). Pituitary irradiation with high-energy proton beams a preliminary report. *Cancer Research*, 18(2):121–134.
- van Goethem, M. J., van der Meer, R., Reist, H. W., and Schippers, J. M. (2009). Geant4 simulations of proton beam transport through a carbon or beryllium degrader and following a beam line. *Physics in medicine and biology*, 54(19):5831–5846. PMID: 19741273.
- Varian Medical Systems (2012). Varian medical systems | oncology, x-ray & inspection equipment. <http://www.varian.com/>.
- Varian medical systems (2008). RapidArc. [http://www.varian.com/us/oncology/treatments/treatment\\_techniques/rapidarc/](http://www.varian.com/us/oncology/treatments/treatment_techniques/rapidarc/).

- Weber, U., Becher, W., and Kraft, G. (2000). Depth scanning for a conformal ion beam treatment of deep seated tumours. *Physics in Medicine and Biology*, 45(12):3627.
- Wilks, R. J. and Bliss, P. (2002). The use of a compensator library to reduce dose inhomogeneity in tangential radiotherapy of the breast. *Radiotherapy and oncology: journal of the European Society for Therapeutic Radiology and Oncology*, 62(2):147–157. PMID: 11937241.
- Wilks, S. C., Langdon, A. B., Cowan, T. E., Roth, M., Singh, M., Hatchett, S., Key, M. H., Pennington, D., MacKinnon, A., and Snavely, R. A. (2001). Energetic proton generation in ultra-intense laser–solid interactions. *Physics of Plasmas*, 8(2):542–549.
- Willoughby, T. R., Kupelian, P. A., Pouliot, J., Shinohara, K., Aubin, M., Roach, Mack, r., Skrumeda, L. L., Balter, J. M., Litzenberg, D. W., Hadley, S. W., Wei, J. T., and Sandler, H. M. (2006). Target localization and real-time tracking using the calypso 4D localization system in patients with localized prostate cancer. *International journal of radiation oncology, biology, physics*, 65(2):528–534. PMID: 16690435.
- Wolf, R. and Bortfeld, T. (2012). An analytical solution to proton bragg peak deflection in a magnetic field. *Physics in medicine and biology*, 57(17):N329–337. PMID: 22892827.
- Wong, J. W., Sharpe, M. B., Jaffray, D. A., Kini, V. R., Robertson, J. M., Stromberg, J. S., and Martinez, A. A. (1999). The use of active breathing control (ABC) to reduce margin for breathing motion. *International Journal of Radiation Oncology\*Biography\*Physics*, 44(4):911–919.
- Yan, Y., Song, Y., and Boyer, A. L. (2002). An investigation of a video-based patient repositioning technique. *International journal of radiation oncology, biology, physics*, 54(2):606–614. PMID: 12243841.
- Zenklusen, S. M., Pedroni, E., and Meer, D. (2010). A study on repainting strategies for treating moderately moving targets with proton pencil beam scanning at the new gantry 2 at PSI. *Physics in Medicine and Biology*, 55(17):5103–5121.
- Zhang, Y., Boye, D., Tanner, C., Lomax, A. J., and Knopf, A. (2012). Respiratory liver motion estimation and its effect on scanned proton beam therapy. *Physics in medicine and biology*, 57(7):1779–1795. PMID: 22407290.

# List of Figures

2.1.1	Schematic drawing of depth dose curves for protons and Carbon ions	6
2.2.1	Schematic drawing of a cyclotron	10
2.2.2	Design of a single room proton therapy facility by <i>Mevion</i>	11
2.2.3	Schematic drawing of a synchrotron	12
2.3.1	Schematic drawing of laser acceleration	14
2.3.2	Schematic drawing of a dielectric wall accelerator (DWA).	16
2.3.3	Schematic drawing of a cyclinac taken from	18
2.4.1	Passive beam delivery	19
2.4.2	Active beam scanning	21
2.5.1	Schematic drawing of interplay effects	26
3.1.1	Schematic drawing of previous versions of TULIP designs	38
3.1.2	Drawing of the most recent TULIP design	39
4.1.1	Initial $\sigma_0$ and FWHMs for increasing proton energies	43
4.1.2	Tulip dose calculation flow chart	46
4.1.3	Transversal view of the CT of Phantom1	48
4.1.4	Rotational dose delivery with TULIP	49
4.1.5	TuDoCa evaluation: histograms	52
4.1.6	TuDoCa evaluation: depth dose profiles for 3DSS	53
4.1.7	TuDoCa evaluation: dose distributions for 3DSS	54
4.1.8	TuDoCa evaluation: depth dose profiles for static rotational delivery	55
4.1.9	TuDoCa evaluation: dose distributions for static rotational delivery	56
4.1.10	Effect of submillimeter IC on the dose distribution for dynamic rotational delivery	58
4.1.11	Effect of submillimeter IC shift on the dose distribution for DET	59
4.2.1	Gantry positions for dynamic rotational dose delivery with TULIP	65
4.2.2	Dvhs for rotational dynamic dose delivery without a fixed angular step	68
4.2.4	Comparison of dose distributions for 3D spot scanning and dynamic rotational delivery	70
4.2.5	Dose profiles for 3D spot scanning and rotational delivery	71
4.2.6	CT views for 3DSS patient cases.	75

4.2.7	Inclusive dvhs for 3D spot scanning irradiation of the spine sarcoma . . .	76
4.2.8	Dose distribution for craniospinal irradiation with TULIP . . . . .	77
4.2.9	Inclusive dvhs for 3D spot scanning irradiation of the prostate . . . . .	78
4.2.10	Dose distributions for a lung patient for different BDRs . . . . .	82
5.2.1	Process flow of 4D dose delivery simulation software I . . . . .	87
5.2.2	Process flow of 4D dose delivery simulation software II . . . . .	88
5.2.3	Measured motion data and correlated CT phases . . . . .	90
5.2.4	Motion parameter values for the individual patients . . . . .	92
5.2.5	CT views of lung and liver patients . . . . .	93
5.3.1	DVHs showing the magnitude of the effect of tumor motion during irradi- ation on the dose . . . . .	97
5.3.2	Dose distribution for the lung tumor of patient LU2 . . . . .	98
5.3.3	Dose distribution for the static and moving liver tumor of patient LI . . . .	98
5.3.4	DVHs for rescanning with TULIP . . . . .	101
5.3.5	DVHs for rescanning with TULIP for liver patient LI . . . . .	102
5.3.6	DVHs for rescanning with TULIP . . . . .	103

# List of Tables

3.1.1	TULIP design parameters . . . . .	37
4.1.1	Patient and beam specific input data and parameters for TuDoCa . . . . .	44
4.1.2	Cylindrical phantom 'Phantom1' CT data . . . . .	48
4.1.3	Evaluation of dose algorithm: results . . . . .	51
4.1.4	Influence of relative isocenter shift on the dose distributions: results . . . . .	58
4.2.1	CT data for cylindrical phantom and lung patient A . . . . .	63
4.2.2	Parameter combinations for dynamic and static dose delivery with TULIP . . . . .	64
4.2.3	Dosimetric results for rotational dynamic and 3D spot scanning dose delivery with TULIP . . . . .	66
4.2.4	Results with regard to time for rotational dynamic and 3D spot scanning dose delivery with TULIP . . . . .	66
4.2.5	Patient data for 3D spot scanning dose delivery simulation study . . . . .	74
4.2.6	TULIP specific beam delivery parameters . . . . .	74
4.2.7	Results for 3D spot scanning dose delivery with TULIP . . . . .	76
4.2.8	Irradiation time for 3D spot scanning dose delivery with TULIP . . . . .	78
4.2.9	Patient Data for studying the influence of BDRs on the dose . . . . .	80
4.2.10	Influence of breakdowns on the dose . . . . .	81
5.2.1	CT acquisition steps . . . . .	89
5.2.2	Patient motion parameter values . . . . .	91
5.2.3	CT data for lung and liver patients . . . . .	93
5.2.4	Treatment planning data for lung and liver patients . . . . .	94
5.2.5	TULIP specific beam delivery parameters . . . . .	94
5.3.1	Results for 4D spot scanning dose delivery . . . . .	97
5.3.2	Irradiation times for 3D spot scanning dose delivery to moving tumors with TULIP . . . . .	99
5.3.3	Results for 4D rescanning dose delivery with TULIP . . . . .	100
5.3.4	Irradiation times for 4D rescanning dose delivery with TULIP . . . . .	100





## Acknowledgments

First, I want to express my gratitude to my supervisor Prof. Dr. Uwe Oelfke for giving me the opportunity to work at the German Cancer Research Center and for supporting me and my individual interests throughout my thesis.

I thank Prof. Dr. Wolfgang Schlegel for acting as a second referee and for constantly providing support, whenever needed. I am grateful for a friendly and nice working environment in the department of Medical Physics in Radiationtherapy supported by Prof. Schlegel.

I am very grateful to Prof. Dr. Ugo Amaldi, who had the idea for the TULIP project and thus made this work possible. Special thanks go also to the entire TERA group at CERN (Switzerland) who supported me throughout this work with fruitful discussions and a nice working environment.

Dr. Simeon Nill I wish to thank for his outstanding support and active help throughout the entire time I spent at the German Cancer Research Center.